บทความทางวิชาการ เรื่อง

Adaptive Finite Element Method for Analysis of Pollutant Dispersion in Shallow Water

Published in the

Journal of Applied Mathematics and Mechanics

Vol. 26, No. 12, pp. 1574-1584 2005 ©Editorial Committee of Appl. Math. Mech., ISSN 0253-4827

Article ID: 0253-4827 (2005) 12-1574-11

ADAPTIVE FINITE ELEMENT METHOD FOR ANALYSIS OF POLLUTANT DISPERSION IN SHALLOW WATER *

Somboon Otarawanna, Pramote Dechaumphai

(Mechanical Engineering Department, Chulalongkorn University,
Bangkok 10330, Thailand)

(Communicated by ZHOU Zhe-wei)

Abstract: A finite element method for analysis of pollutant dispersion in shallow water is presented. The analysis is divided into two parts: (1) computation of the velocity flow field and water surface elevation, and (2) computation of the pollutant concentration field from the dispersion model. The method was combined with an adaptive meshing technique to increase the solution accuracy, as well as to reduce the computational time and computer memory. The finite element formulation and the computer programs were validated by several examples that have known solutions. In addition, the capability of the combined method was demonstrated by analyzing pollutant dispersion in Chao Phraya River near the gulf of Thailand.

Key words: shallow water; pollutant dispersion; adaptive meshing technique; finite element method

Chinese Library Classification: 0242.21; 0368 2000 Mathematics Subject Classification: 76B15 Document code: A

Introduction

Nowadays, both the industrial and urban zones in Thailand have increased rapidly. The discharge of thermally or chemically polluted water from power stations, industrial plants, and households into rivers has become a threat to water resources. Authorities now require proof that the environmental impact of a planned discharge will not exceed a certain level, and plant designers must keep the impact below the specified level. For this reason, both authorities and plant designers have strong interest in reliable methods for predicting the distribution of pollutants resulting from a given discharge into a river.

The behavior of pollutant dispersion in shallow water is governed by the conservation of mass and momentum, and the pollutant transport equation. The analysis may be considered as a two-dimensional depth-averaged problem by assuming uniform velocities over the depth with their values equal to the depth-averaged velocities. The above governing differential

^{*} Received Jun. 10,2004; Revised Aug. 08,2005
Project supported by the Thailand Research Foundation (TRF)
Corresponding author P. Dechaumphai, Professor, Doctor, E-mail:fmepdc@eng.chula.ac.th

equations are coupled and nonlinear, and thus cannot be solved by analytical methods especially for complex flow geometry. Several computational methods have been proposed in the past. These include the finite difference method^[1-5], the finite volume method^[6,7] and the finite element method^[8-12]. The finite element method is widely used currently because it can handle complex geometries effectively^[12].

The accuracy of solution by the finite element method mainly depends on element sizes. High solution accuracy is obtained if small clustered elements are used in the model. However, the computational time and computer memory are increased if a large number of elements is used. Adaptive meshing technique^[13,14] can be applied to increase the analysis solution accuracy, and to reduce the computational time and memory. Such technique places small elements in the region of large change in the solution gradients to capture accurate solution, while locating coarse elements in other regions where the solutions are nearly uniform.

The paper starts by explaining the finite element formulation and the corresponding solution procedure that leads to the development of computer programs. The basic idea behind the adaptive meshing technique is then described. Finally, the derived finite element equations and the developed computer programs are validated using simple examples that have known solutions prior to applying to solve more complex problems.

1 Flow Model

1.1 Governing equations

The governing equations that explain the flow behavior of shallow water flow can be derived by averaging the mass and momentum conservation equations in two-dimensional over the depth. These equations are

$$\frac{\partial (Hu)}{\partial x} + \frac{\partial (Hv)}{\partial y} = 0, \qquad (1a)$$

$$\left(u\frac{\partial u}{\partial x} + v\frac{\partial u}{\partial y}\right) = \left(\frac{\partial \sigma_x}{\partial x} + \frac{\partial \tau_x}{\partial y}\right) - \frac{g\sqrt{u^2 + v^2}}{C^2 H}u,\tag{1b}$$

$$\left(u\frac{\partial v}{\partial x} + v\frac{\partial v}{\partial y}\right) = \left(\frac{\partial \tau_{sy}}{\partial x} + \frac{\partial \sigma_{y}}{\partial y}\right) - \frac{g\sqrt{u^{2} + v^{2}}}{C^{2}H}v, \qquad (1c)$$

where H is the total water depth, u and v are the depth-averaged velocity components in x- and y-directions, respectively; g is the gravitational acceleration; and C is the Chezy friction coefficient. The stress components σ_x , σ_y , τ_{xy} and τ_{xz} are defined by

$$\sigma_x = 2\nu \frac{\partial u}{\partial x} - g\zeta, \qquad (2a)$$

$$\sigma_{y} = 2\nu \frac{\partial v}{\partial y} - g\zeta, \tag{2b}$$

$$\tau_{xy} = \tau_{yx} = \nu \left(\frac{\partial u}{\partial y} + \frac{\partial v}{\partial x} \right),$$
 (2c)

and where ζ is the elevation of the water surface over the mean surface level as shown in Fig. 1, ν is the eddy viscosity coefficient.

The differential equations, Eqs.(1a) - (1c), are to be solved with appropriate

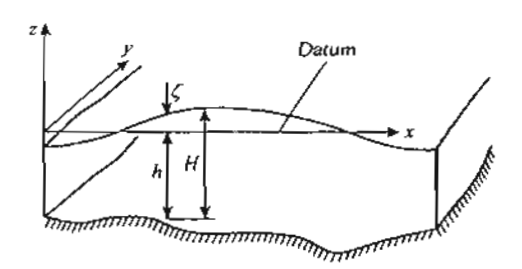


Fig. 1 The notationa of shallow water problem

boundary conditions which are either specified depth-averaged velocity components along edge S_1 ,

$$u = u_1(x,y)$$
, $v = v_1(x,y)$, (3a,b)
or surface tractions along edge S_2 ,

$$T_x = \sigma_x l + \tau_m m, \qquad (4a)$$

$$T_{r} = \tau_{sr} l + \sigma_{r} m, \qquad (4b)$$

where l and m are the direction cosines of the unit vector normal to the boundary edge.

1.2 Finite element formulation

The basic unknowns for the shallow water flow problem corresponding to the continuity Eq.(1a) and the two momentum equations (1b) – (1c) are the depth-averaged velocity components u, v and the water surface elevation ζ . The six-node triangular element suggested in Ref. [15] is used in this study. The element assumes a quadratic interpolation for the velocity component distributions and linear interpolation for the water surface elevation distribution according to their highest derivative orders in the differential Eqs.(1a) – (1c) as

$$u(x,y) = N_B u_B, \quad v(x,y) = N_B v_B, \quad (x,y) = H_\mu \zeta_\mu, \quad (5a,b,c)$$

where $\beta = 1, 2, \dots, 6$; $\mu = 1, 2, 3$; N_{β} and H_{μ} are the element interpolation functions for the velocity and water surface elevation, respectively.

To derive the finite element equations, the method of weighted residuals^[17] is applied to the momentum Eqs.(1b) - (1c) and the continuity Eq.(1a),

$$\int_{A} N_{i} \left[(uu_{,x} + vu_{,y}) - (\sigma_{x,x} + \tau_{yx,y}) + \frac{g\sqrt{u^{2} + v^{2}}}{C^{2}H} u \right] dA = 0,$$
 (6a)

$$\int_{A} N_{i} \left[(uv_{,x} + vv_{,y}) - (\tau_{xy,x} + \sigma_{y,y}) + \frac{g\sqrt{u^{2} + v^{2}}}{C^{2}H} v \right] dA = 0,$$
 (6b)

$$\int_{t} H_{i}[(Hu)_{,x} + (Hv)_{,y}] dA = 0, \qquad (6c)$$

where A is the element area. Applying Gauss's theorem^[16] to Eqs.(6a) - (6c) for generating the element boundary integrals, leads to the finite element equations which can be written in tensor form as

$$K_{\alpha\beta\gamma}u_{\beta}u_{\gamma} + K_{\alpha\beta\gamma}v_{\beta}u_{\gamma} - H_{\alpha\mu}\zeta_{\mu} + S_{\alpha\beta\gamma}u_{\beta} + S_{\alpha\beta\gamma}v_{\beta} + C_{\alpha\beta}u_{\beta} = Q_{\alpha\gamma}, \qquad (7a)$$

$$K_{\alpha\beta\gamma} u_{\beta} v_{\gamma} + K_{\alpha\beta\gamma} v_{\beta} v_{\gamma} - H_{\alpha\mu} \zeta_{\mu} + S_{\alpha\beta\gamma} u_{\beta} + S_{\alpha\beta\gamma} v_{\beta} + C_{\alpha\beta} v_{\beta} = Q_{\alpha\gamma}, \tag{7b}$$

$$J_{\mu\rho\eta^{x}}(\zeta_{\mu} + h_{\mu})u_{\beta} + J_{\mu\rho\eta^{y}}(\zeta_{\mu} + h_{\mu})v_{\beta} - R_{\eta\mu}\zeta_{\mu} = R_{\eta\mu}h_{\mu}, \tag{7c}$$

where the coefficients in these equations are defined by

$$K_{\alpha\beta\gamma^x} = \int_A N_{\alpha} N_{\beta} N_{\gamma,x} dA, \quad K_{\alpha\beta\gamma^y} = \int_A N_{\alpha} N_{\beta} N_{\gamma,y} dA, \quad H_{\alpha\mu^x} = g \int_A N_{\alpha,x} H_{\mu} dA, \quad (8a,b,c)$$

$$H_{\alpha\mu^{T}} = g \int_{A} N_{\alpha,\gamma} H_{\mu} dA, \quad S_{\alpha\beta^{c\alpha}} = 2\nu \int_{A} N_{\alpha,x} N_{\beta,x} dA + \nu \int_{A} N_{\alpha,\gamma} N_{\beta,\gamma} dA, \quad (8d,e)$$

$$S_{\alpha\beta^{SY}} = 2\nu \int_{A} N_{\alpha,y} N_{\beta,x} dA, \quad S_{\alpha\beta^{SX}} = \nu \int_{A} N_{\alpha,x} N_{\beta,y} dA, \qquad (8f,g)$$

$$S_{\alpha\beta} = \nu \int_{A} N_{\alpha,x} N_{\beta,x} dA + 2\nu \int_{A} N_{\alpha,y} N_{\beta,y} dA, \quad C_{\alpha\beta} = \frac{g \sqrt{u^2 + v^2}}{C^2 (\zeta + h)} \int_{A} N_{\alpha} N_{\beta} dA, \quad (8h,i)$$

$$Q_{\alpha^s} = \frac{1}{\rho} \int_S N_{\alpha} T_s dS, \quad Q_{\alpha^r} = \frac{1}{\rho} \int_S N_{\alpha} T_r dS, \quad J_{\mu\beta\eta^r} = \int_A H_{\mu} N_{\beta} H_{\eta,x} dA, \quad (8j,k,l)$$

$$J_{\mu\beta\eta\gamma} = \int_{A} H_{\mu} N_{\beta} H_{\eta,\gamma} dA$$
, $R_{\eta\mu} = \int_{S} H_{\eta} H_{\mu} V_{\eta} dS$. (8m,n)

1.3 Computational procedure

The nonlinear finite element equations, as shown in Eqs. (7a) - (7c), are solved by Newton-Raphson iteration method. The method requires writing the unbalanced values in the form,

$$F_{ax} = K_{aax} u_{a} u_{a} + K_{aax} v_{a} u_{x} - H_{aax} \zeta_{u} + S_{aa} u_{a} + S_{aa} v_{a} + C_{aa} u_{a} - Q_{a} , \quad (9a)$$

$$F_{\alpha T} = K_{\alpha \theta T} u_{\beta} v_{\gamma} + K_{\alpha \theta T} v_{\beta} v_{\gamma} - H_{\alpha \omega} \zeta_{\mu} + S_{\alpha \theta T} u_{\beta} + S_{\alpha \theta T} v_{\beta} + C_{\alpha \theta} v_{\beta} - Q_{\alpha T}, \qquad (9b)$$

$$F_{\eta} = J_{\mu \beta \eta^{x}} (\zeta_{\mu} + h_{\mu}) u_{\beta} + J_{\mu \beta \eta^{y}} (\zeta_{\mu} + h_{\mu}) v_{\beta} - R_{\eta \mu} (\zeta_{\mu} + h_{\mu}). \tag{9c}$$

Then application of the method leads to a set of algebraic equations with incremental unknowns of the form

$$\begin{bmatrix} (C_{\alpha\beta^{x}})_{(6\times6)} & (L_{\alpha\beta^{y}})_{(6\times6)} & (-H_{\alpha\mu^{x}})_{(6\times3)} \\ (L_{\alpha\beta^{x}})_{(6\times6)} & (C_{\alpha\beta^{y}})_{(6\times6)} & (-H_{\alpha\mu^{y}})_{(6\times3)} \\ (Z_{\eta\beta^{x}})_{(3\times6)} & (Z_{\eta\beta^{y}})_{(3\times6)} & (Q_{\eta\mu})_{(3\times3)} \end{bmatrix} \begin{bmatrix} (\Delta u_{\beta})_{(6\times1)} \\ (\Delta v_{\beta})_{(6\times1)} \\ (\Delta \zeta_{\mu})_{(3\times1)} \end{bmatrix} = - \begin{bmatrix} (F_{\alpha^{x}})_{(6\times1)} \\ (F_{\alpha^{y}})_{(6\times1)} \\ (F_{\eta})_{(3\times1)} \end{bmatrix}, \quad (10)$$

where the coefficients in the above equations are

$$G_{\alpha\beta^{\alpha}} = K_{\alpha\beta\gamma^{\alpha}} u_{\gamma} + K_{\alpha\gamma\beta^{\alpha}} u_{\gamma} + K_{\alpha\gamma\beta^{\alpha}} v_{\gamma} + S_{\alpha\beta^{\alpha\alpha}} + C_{\alpha\beta}, \tag{11a}$$

$$G_{\alpha\beta^{T}} = K_{\alpha\gamma\beta^{T}} v_{\gamma} + K_{\alpha\gamma\beta^{T}} v_{\gamma} + K_{\alpha\gamma\beta^{T}} u_{\gamma} + S_{\alpha\beta^{T}} + C_{\alpha\beta}, \tag{11b}$$

$$\begin{array}{lll} L_{\alpha\beta^{\alpha}} = K_{\alpha\beta\gamma^{\alpha}} v_{\gamma} + S_{\alpha\beta^{\sigma\alpha}}, & L_{\alpha\beta^{\sigma}} = K_{\alpha\beta\gamma^{\sigma}} u_{\gamma} + S_{\alpha\beta^{\sigma\gamma}}, & Z_{\eta\beta^{\alpha}} = J_{\mu\beta\eta^{\alpha}} (\zeta_{\mu} + h_{\mu}), & (\text{llc,d,e}) \\ Z_{\eta\beta^{\sigma}} = J_{\mu\beta\eta^{\sigma}} (\zeta_{\mu} + h_{\mu}), & Q_{\eta\mu} = J_{\mu\beta\eta^{\alpha}} u_{\beta} + J_{\mu\beta\eta^{\gamma}} v_{\beta} - R_{\eta\mu}. & (\text{llf,g}) \end{array}$$

These coefficients which are in form of element matrices can be evaluated in closed-form for triangular elements ready for computer programming. Details of the derivation of these element matrices are omitted herein for brevity. In these Eqs.(11a) – (11g), u_{γ} and v_{γ} are the values of the velocity components at the *i*-th iteration. The iteration process is terminated if the change in percentage of the overall errors of the nodal unknowns from the previous iteration is less than the specified value.

1.4 Adaptive meshing technique

The idea behind the adaptive meshing technique presented herein is to construct a new mesh based on the solution obtained from the previous mesh^[13,14]. The new mesh consists of small elements in the regions with large change in solution gradients and larger elements in the regions where the change in solution gradients is small. To determine proper element sizes at different locations in the flow field, the solid-mechanics concept of determining the principal stresses from a given state of stresses at a point is employed. Since small elements are needed in the regions of complex flow behavior, thus the velocity distribution can be used as an indicator in the determination of proper element sizes.

To determine proper element sizes, the second derivatives of the flow velocity with respect to the global coordinates x and y are first computed,

$$\begin{bmatrix} \frac{\partial^2 V}{\partial x^2} & \frac{\partial^2 V}{\partial x \partial y} \\ \frac{\partial^2 V}{\partial x \partial y} & \frac{\partial^2 V}{\partial y^2} \end{bmatrix}, \tag{12}$$

where V is the magnitude of two velocity components u and v,

$$V = \sqrt{u^2 + v^2}. (13)$$

The principal quantities in the principal directions X and Y where the cross derivatives vanish, are then determined

$$\begin{bmatrix} \frac{\partial^2 V}{\partial X^2} & 0\\ 0 & \frac{\partial^2 V}{\partial Y^2} \end{bmatrix} \tag{14}$$

The magnitude of the large principal quantity is then selected

$$\lambda = \max\left(\left|\frac{\partial^2 V}{\partial X^2}\right|, \left|\frac{\partial^2 V}{\partial Y^2}\right|\right). \tag{15}$$

This value is used to compute proper element size, and is the maximum principal quantity for the entire model

$$h^2 \lambda = \text{const} = h_{\min}^2 \lambda_{\max}, \qquad (16)$$

where h_{\min} is the specified minimum element size, and λ_{\max} is the maximum principal quantity for the entire model.

Based on the condition shown in Eq.(16), proper element sizes are generated according to the given minimum element size h_{\min} . Specifying too small h_{\min} may result in a model with an excessive number of elements. On the other hand, specifying too large h_{\min} may result inadequate solution accuracy or excessive analysis and remeshing cycles. These factors must be considered prior to generating a new mesh.

2 Dispersion Model

2.1 Governing equation

The depth-averaged pollutant transport equation is decoupled from the associated shallow water flow equations (1a) - (1c) and is given by

$$\frac{\partial(H\Theta)}{\partial t} + \frac{\partial(Hu\Theta)}{\partial x} + \frac{\partial(Hv\Theta)}{\partial y} = D\left[\frac{\partial}{\partial x}\left(H\frac{\partial\Theta}{\partial x}\right) + \frac{\partial}{\partial y}\left(H\frac{\partial\Theta}{\partial y}\right)\right],\tag{17}$$

where Θ is the pollutant concentration, and D is the dispersion coefficient. This differential equation is to be solved together with the boundary conditions that may consist of specifying the concentration

$$\Theta = \Theta_i(x, y), \tag{18}$$

or its gradient

$$\frac{\partial \Theta}{\partial n} = q_2(x, y), \qquad (19)$$

and the initial condition of

$$\Theta(x,y,0) = \Theta_0. \tag{20}$$

2.2 Finite element formulation

The distribution for the element concentration is first assumed as

$$\Theta(x,y,t) = [N(x,y)]_{(1\times3)} \{\Theta(t)|_{(3\times1)}, \qquad (21)$$

where $[N(x,y)]_{(1\times3)}$ are the linear interpolation functions. Applying the method of weighted residual and substituting Eq.(21) into Eq.(17) lead to the finite element equations in the form

$$\int_{A} \{ W \} [N] dA \{ \hat{\Theta} \} + \int_{A} \{ W \} [u - v] [B] dA \{ \hat{\Theta} \}
+ \left\{ \int_{A} D \left(\left\{ \frac{\partial W}{\partial x} \right\} \left[\frac{\partial N}{\partial x} \right] - \frac{1}{\{N\}\{H\}} \{ W \} \left[\frac{\partial N}{\partial x} \right] \{ H \} \left[\frac{\partial N}{\partial x} \right] \right\} dA
+ \int_{A} D \left(\left\{ \frac{\partial W}{\partial y} \right\} \left[\frac{\partial N}{\partial y} \right] - \frac{1}{\{N\}\{H\}} \{ W \} \left[\frac{\partial N}{\partial y} \right] \{ H \} \left[\frac{\partial N}{\partial y} \right] \right) dA \right\} \{ \hat{\Theta} \}
= \int_{A} \{ W \} q_{A} dS$$
(22)

or

$$[C]\{\dot{\Theta}\} + [[K_{\nu}] + [K_{c}]]\{\Theta\} = \{Q\},$$
 (23)

where the coefficients in this equation are defined by

$$[C] = \int_{A} \{W\}[N] dA, \qquad (24a)$$

$$[K_{\nu}] = \int \{W\}[u \quad \nu][B] dA, \qquad (24b)$$

$$[K_c] = \left\{ \int_A D\left(\left\{ \frac{\partial W}{\partial x} \right\} \left[\frac{\partial N}{\partial x} \right] - \frac{1}{[N]\{H\}} \{W\} \left[\frac{\partial N}{\partial x} \right] \{H\} \left[\frac{\partial N}{\partial x} \right] \right) dA$$

$$+ \int_{A} D\left(\left\{\frac{\partial W}{\partial y}\right\} \left[\frac{\partial N}{\partial y}\right] - \frac{1}{[N]\{H\}} \{W\} \left[\frac{\partial N}{\partial y}\right] \{H\} \left[\frac{\partial N}{\partial y}\right]\right) dA\right\}, \qquad (24c)$$

$$\{Q\} = \int_{S} |W| q, dS. \tag{24d}$$

2.3 Time discretization

The explicit recurrence relations are applied for time integration of Eq.(23). The application leads to

$$\frac{1}{\Delta t}[C]\{\Theta\}_{a+1} = \left(\frac{1}{\Delta t}[C] + [[K_V] + [K_C]]\right)|\Theta\}_a + |Q\}_a. \tag{25}$$

which can be solved directly for all nodal values of the pollutant concentration Θ in the flow domain.

3 Examples

In this section, three examples are presented. The first two examples are used to validate the finite element formulation derived and the computer program developed for flow field calculation. The validity of pollutant dispersion model is shown by the last example.

3.1 Flow in rectangular canal with variation in bottom profile

The first example presents the analysis of flow behavior in rectangular canal with variation in bottom profile as illustrated in Fig. 2. Figure 3 shows the finite element model and the boundary conditions with the maximum inlet velocity of 1.5 m/s, eddy viscosity

coefficient $\nu = 166.67 \text{ m}^2/\text{s}$, Chezy coefficient $C = 50 \text{ m}^{1/2}/\text{s}$, and gravitational acceleration $g = 10 \text{ m/s}^2$. This finite element mesh consists of 357 nodes and 160 elements. Figure 4 shows close agreement between the computed solution and that of the penalty finite element method in Ref. [9].

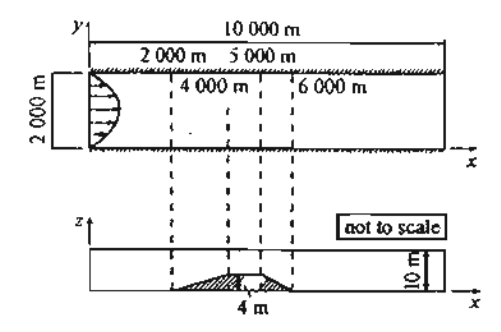


Fig. 2 Problem statement of flow in rectangular canal with variation in bottom profile

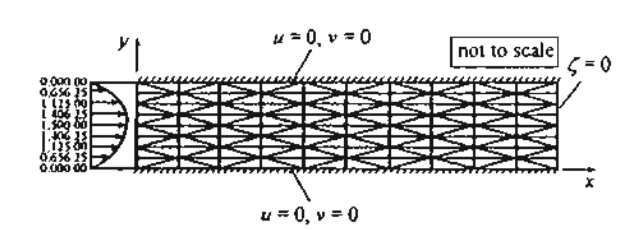


Fig. 3 Finite element model for flow in rectangular canal with variation in bottom profile

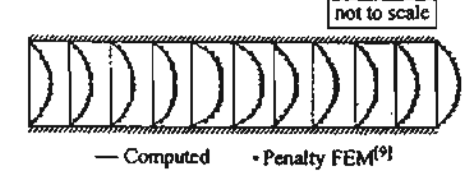


Fig. 4 Comparison of velocities for flow in rectangular canal with variation in bottom profile

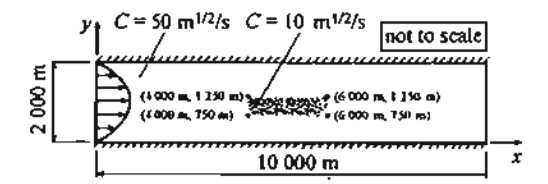


Fig. 5 Problem statement of flow in rectangular canal with variation in bottom friction

3.2 Flow in rectangular canal with variation in bottom friction

The geometry and the flow properties of this example are identical to those of the first example, except for the mean depth of 10 m everywhere and the Chezy coefficient of 10 m^{1/2}/s in the shaded zone of Fig. 5. Figure 6 shows the boundary conditions and the finite element mesh which consists of 187 nodes and 80 elements. The comparison of the computed velocity distribution with the solution presented in Ref. [9] using penalty finite element is shown in Fig. 7.

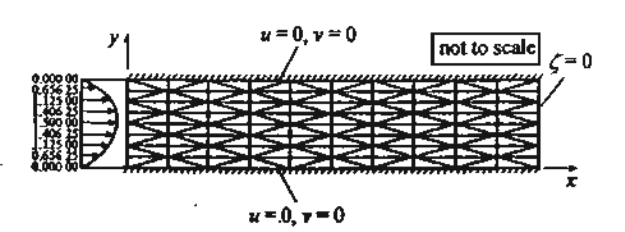


Fig. 6 Finite element model for flow in rectangular canal with variation in bottom friction

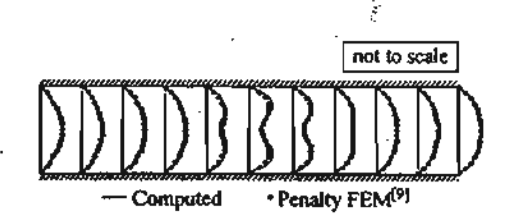
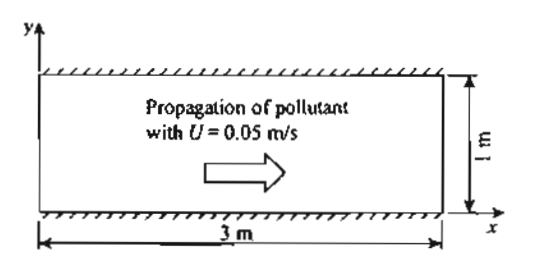


Fig. 7 Comparison of velocities for flow in rectangular canal with variation in bottom friction

3.3 Propagation of pollutant through open rectangular channel

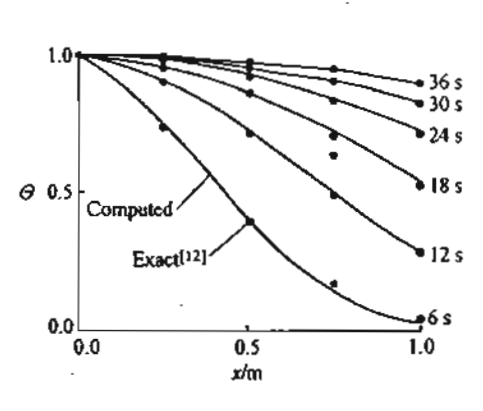
To verify the finite element formulation and the computer program developed for pollutant dispersion analysis, the concentration evolution of pollutant along an open channel in Fig. 8 is studied. The finite element mesh and the initial and boundary conditions are shown in Fig. 9. The mesh contains 50 nodes and 72 elements and taking a time interval Δt = 0.1s. The transient solution for times t = 6,12,18,24,30 and 36 s is presented for uniform velocity U = 0.05 m/s over the domain and dispersion coefficient D = 0.01 m²/s. Figure 10 shows the transient solution of pollutant concentration along the x-axis. The computed result is in very close agreement with the exact solution given in Ref. [12].



 $\partial \Theta / \partial n = 0$ Initial condition $\Theta = 0$ at all points $\partial \Theta / \partial n = 0$

Fig. 8 Problem statement of pollutant propagation through open rectangular channel

Fig. 9 Finite element model for pollutant propagation through open rectangular channel



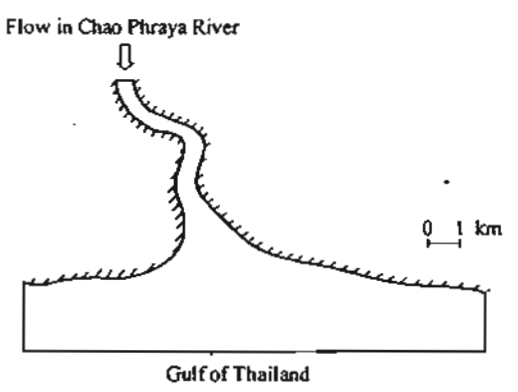


Fig. 10 Comparison of concentration for pollutant propagation through open rectangular channel

Fig. 11 Computational domain of Chao Phraya river

4 Application to Chao Phraya River

4.1 Flow in river

The geometry of the Chao Phraya River is shown in Fig. 11. Figure 12 shows the finite element model and the boundary conditions with the maximum inlet velocity of 1.5 m/s, eddy viscosity coefficient $\nu = 15 \,\mathrm{m}^2/\mathrm{s}$, Chezy coefficient $C = 50 \,\mathrm{m}^{1/2}/\mathrm{s}$, and the gravitational acceleration $g = 9.81 \,\mathrm{m/s}^2$. This initial finite element mesh consists of 4 111 nodes and 1 948 elements.

The numerical solution obtained from the initial mesh is then used to construct the second adaptive mesh as described in Section 1.4. The second adaptive mesh consisting of 4 153 nodes and 1 954 elements is shown in Fig. 13. The figure shows smaller elements are generated in the regions where large change in velocity gradients occurs. At the same time, larger elements are generated in other regions where the velocity is nearly uniform. With this second adaptive mesh, the entire procedure is repeated again to generate the third adaptive mesh with 3 411 nodes and 1 594 elements as shown in Fig. 14. The corresponding flow solution and its detail are shown in Figs. 15 and 16, respectively.

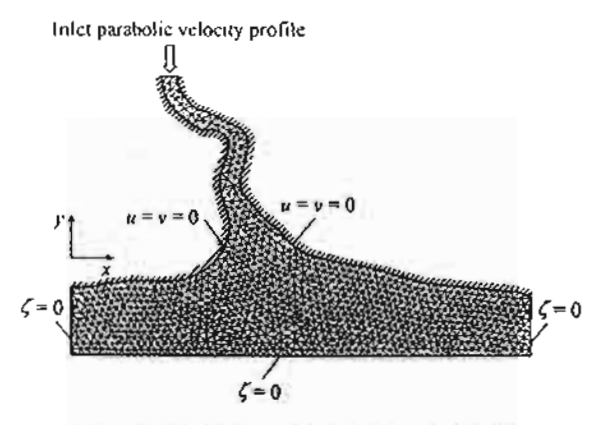


Fig. 12 Initial finite element mesh and boundary conditions for flow in Chao Phraya river

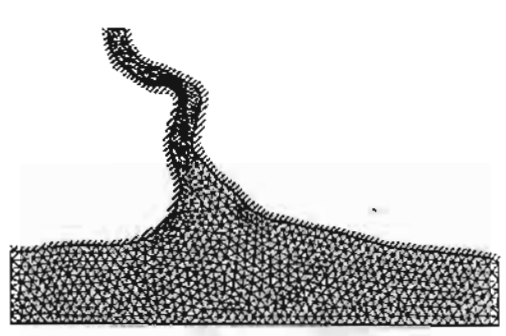


Fig. 13 Second finite element mesh for flow in Chao Phraya river

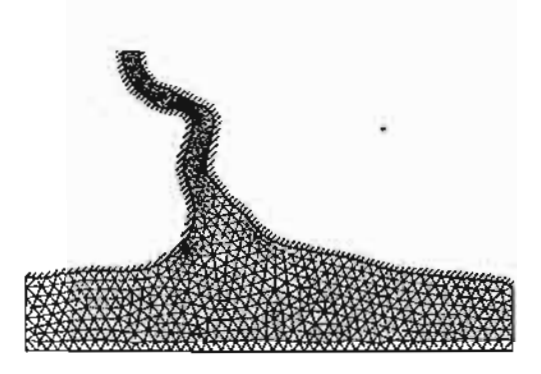


Fig. 14 Third finite element mesh for flow in Chao Phraya river

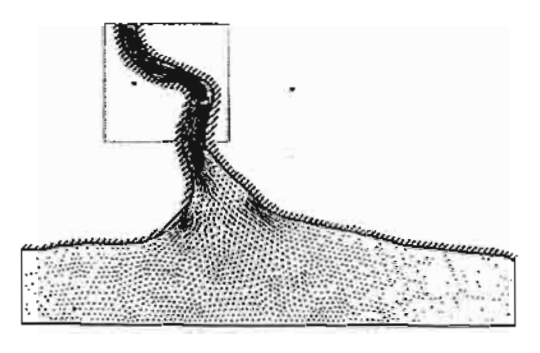


Fig. 15 Predicted velocity distribution for flow in Chao Phraya river

4.2 Dispersion in river

Contamination due to pollutant discharged from an industrial plant is studied. Fig. 17 shows the boundary conditions with the initial condition of no pollutant concentration throughout the computational domain. The dispersion coefficient is given as $50 \text{ m}^2/\text{s}$ and the time interval has the value $\Delta t = 100 \text{ s}$. The final adaptive mesh of the flow model as shown in Fig. 14 is used as the finite element mesh for the dispersion analysis. Figure 18 shows the computed concentration contours in the river at three hours after the plant disposal. Detail of distribution of pollutant-concentration near the plant is also shown in Fig. 19.

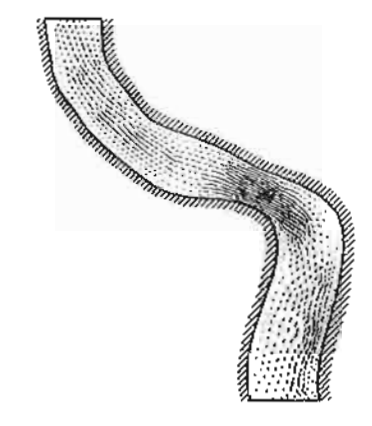


Fig. 16 Detail of predicted velocity distribution for flow in Chao Phraya river

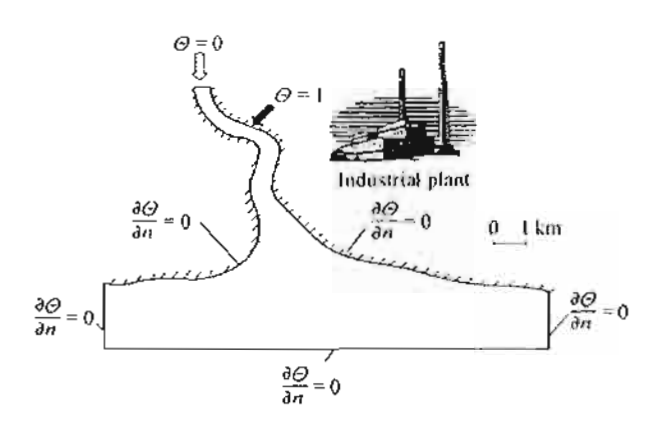


Fig. 17 Computational domain and bounary conditions for pollutant dispersion in Chao Phraya river

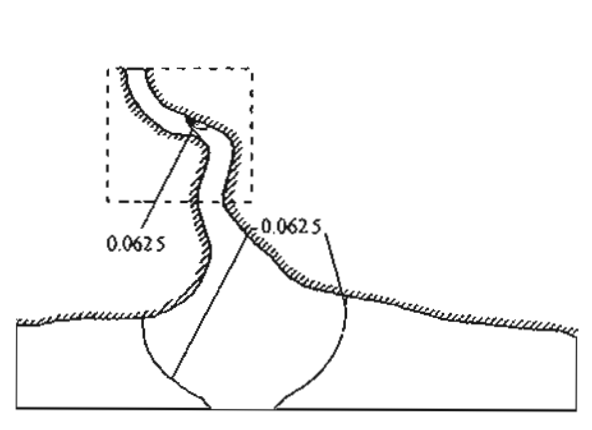


Fig. 18 Predicted distribution of pollutant concentration for pollutant dispersion in Chao Phraya river at three hours after the plant disposal

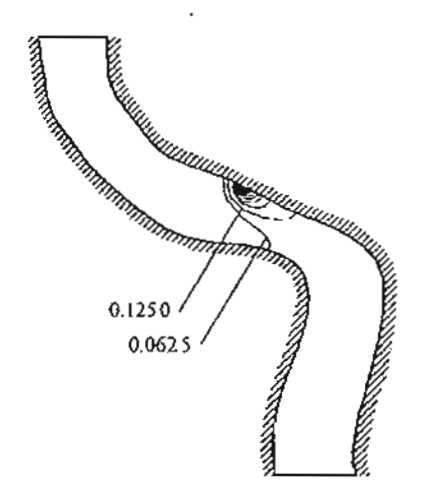


Fig. 19 Detail of predicted distribution of pollutant concentration for pollutant dispersion in Chao Phraya river at three hours after the plant disposal

5 Concluding Remarks

This paper presents the finite element method for analysis of pollutant dispersion in shallow water. The finite element formulation and its computational procedure is first described. The corresponding finite element equations are derived and the corresponding computer programs that can be executed on a standard personal computer have been developed. The finite element method is combined with the adaptive meshing technique in order to improve the flow solution accuracy. The adaptive meshing technique generates an entirely new mesh based on the solution obtained from a previous mesh. The new mesh consists of clustered elements in regions with large changes in the velocity gradients to

provide higher solution accuracy. Elsewhere, coarse elements are generated to reduce the computational time and computer memory. The results in this paper have demonstrated the capability of the combined method for the prediction of pollutant dispersion behaviors.

References:

- [1] Rastogi A K, Rodi W. Predictions of heat and mass transfer in open channels [J]. J Hydr Eng Div-ASCE, 1978, 104 (HY3): 397 420.
- [2] Vreugdenhill C B, Wijbenga J H. A computation of flow patterns in rivers[J]. J Hydr Eng Div-ASCE, 1982, 108 (HY11):1296 - 1310.
- [3] Demuren A O, Rodi W. Calculation of flow and pollutant dispersion in meandering channels
 [3] J Fluid Mech., 1986, 172:63-92.
- [4] Molls T, Chaudhry M H. Depth-averaged open channel flow model [3]. J Hydraul Eng-ASCE, 1995, 121(6):453-465.
- [5] Borthwick A G L, Akponasa G A. Reservoir flow prediction by contravariant shallow water equations [J]. J Hydraul Eng-ASCE, 1997, 123(5):432-439.
- [6] Zhou J G, Goodwill I M. A finite volume method for steady state 2D shallow water flows [J]. Internat J Numer Method H, 1997, 7(1):4 23.
- [7] Yu L, Righetto A M. Depth-averaged turbulence k-w model and applications [1]. Advances in Engineering Software, 2001, 32(5):375-394.
- [8] Zienkiewicz O C, Heinrich J C. A unified treatment of steady-state shallow water and two-dimensional Navier-Stokes equations-finite element approach [J]. Comput Method Appl M, 1979, 17/18:673 698.
- [9] Cochet J F, Dhatt D, Hubert G, Touzot G. River and estuary flows by a new penalty finite element [A]. In: Kawai T (ed). Finite Element Flow Analysis [C]. University of Tokyo Press, Tokyo, 1982, 563 570.
- [10] Leclerc M, Bellemare J, Dumas G, Dhatt G. A finite element model of estuarian and river flows with moving boundaries [J]. Adv Water Resour, 1990, 13(4):158 ~ 168.
- [11] Shrestha P L. An integrated model suite for sediment pollutant transport in shallow lakes[J]. Advances in Engineering Software, 1996, 27(3):201-212.
- [12] Tabuenca P, Vila J, Cardona J, Samartin A. Finite element simulation of dispersion in the Bay of Santander [J]. Advances in Engineering Software, 1997, 28(5):313-332.
- [13] Peraire J, Vahjdati M, Morgan K, Zienkiewicz O C. Adaptive remeshing for compressible flow computation [J]. J Comput Phys, 1987, 72(2):449 466.
- [14] Dechaumphai P, Morgan K. Transient thermal-structural analysis using adaptive unstructured remeshing and mesh movement [A]. In: Thermal Structures and Materials for High-Speed Flight [C]. American Institute of Aeronautics and Astronautics, Washington D C, 1992, 205 228
- [15] Dechaumphai P. Adaptive finite element technique for heat transfer problems [J]. Journal of Energy, Heat and Mass Transfer, 1995, 17(2):87-94.
- [16] Dechaumphai P. Finite Element Method for Computational Fluid Dynamics [M]. Chulalongkorn University Press, Bangkok, 2002.

บทความทางวิชาการ เรื่อง

Interaction of High-Speed Compressible

Viscous Flow and Structure by

Adaptive Finite Element Method

Published in the

Journal of Mechanical Science and Technology

Vol. 10, pp. 1837-1848

2005

Interaction of High-Speed Compressible Viscous Flow and Structure by Adaptive Finite Element Method

Wiroj Limtrakarn

Mechanical Engineering Department. Thammasat University, Bangkok 12120, Thailand
Pramote Dechaumphai*

Mechanical Engineering Department, Chulalongkorn University, Bangkok 10330, Thailand

The Separate Volume of KSME International Journal

Interaction of High-Speed Compressible Viscous Flow and Structure by Adaptive Finite Element Method

Wiroj Limtrakarn

Mechanical Engineering Department, Thammasat University, Bangkok 12120, Thailand

Pramote Dechaumphai*

Mechanical Engineering Department, Chulalongkorn University, Bangkok 10330, Thailand

Interaction behaviors of high-speed compressible viscous flow and thermal-structural response of structure are presented. The compressible viscous laminar flow behavior based on the Navier-Stokes equations is predicted by using an adaptive cell-centered finite-element method. The energy equation and the quasi-static structural equations for aerodynamically heated structures are solved by applying the Galerkin finite-element method. The finite-element formulation and computational procedure are described. The performance of the combined method is evaluated by solving Mach 4 flow past a flat plate and comparing with the solution from the finite different method. To demonstrate their interaction, the high-speed flow, structural heat transfer, and deformation phenomena are studied by applying the present method to Mach 10 flow past a flat plate.

Key Words: Flow-Structure Interaction, Aerodynamic Heating Rate, Adaptive Mesh

Nomenclature				
Ae	: element area			
$[A^*]$: Jacobian matrix			
$\{E_F\}$: fluid flux vector in x direction			
$\{E_{\tau}\}$	thermal flux vector in x direction			
$\{F_F\}$	I fluid flux vector in y direction			
$\{F_r\}$	thermal flux vector in y direction			
С	: specific heat of structure			
Cv	specific heat at constant volume of fluid			
$\{\bar{G}_t\}$: average inviscid flux vector			
$\{\bar{G}_{V}\}$: average viscous flux vector			
$\{h_1, h_2\}$: element sizes			
ĥ	: unit normal vector			
Þ	: pressure			

X, Y : principle directions

: coordinate directions

 $\{u, v\}$: x and y velocity components

 $\{U_{\rm F}\}$: fluid conservation variable vector

TEL: +82-63-290-1473; FAX: +82-63-291-9312 Mechanical Engineering Department, Chulalongkorn University, Bangkok 10330, Thailand (Manuscript Received March 2, 2002; Revised September 27, 2004) $\{U_T\}$: thermal conservation variable vector $\{U_S\}$: nodal displacement vector

 Γ_e : element boundary Ω : element domain δ : length of element sides ϵ : total energy

λι, λε : absolute second derivatives

ρ : density

1. Introduction

Fluid-Thermal-Structural analysis methods have an important role in the design of high-speed flight vehicles, such as hypersonic airbreathing vehicles (Glass et al., 2002), for predicting vehicles' aerothermostructural performance. Significant coupling occurs between high-speed flow phenomena, aerodynamic heating rates on structural surfaces, structural temperature and their gradients, as well as structural deformations and stresses, creating multidisciplinary interaction phenomena. High-speed flow phenomena normally include complex flow characteristics, such as shock waves, shock-shock inter-

^{*} Corresponding Author, E-mail: fmepdc@eng.chula.ac.th

actions, thin boundary layers and shock-boundary layer interactions (Anderson, 1982; Anderson, 1991). Such phenomena have been studied by a number of researchers using both the numerical simulations and experimental techniques. These include, as few examples, the study of shock motion by self-induced oscillation of an expanded jet impinging on a cylinder (Kim et al, 2002), the experimental study for the flow characteristic of the supersonic dual coaxial free jet (Back et al, 2003), and the numerical simulation of shock wave propagation using the lattice Boltzmann method (Kang et al, 2003). Some of these characteristics, especially near the structural surface, generate aerothermal load to vehicle structure, and normally affect the structural temperature, deformation and stress. Under intense aerodynamic heating rate, structural temperature begins to rise within few seconds and significant deformation may occur. In addition, the deformed structure may significantly alter the high-speed flow behavior and thus the aerothermal loads. These coupled effects indicate that the analysis of high-speed flow-structure interaction is an important consideration to high-speed vehicle design. Such coupled effects have been studied by a number of researchers recently. Computational fluid and structural dynamics commercial programs were combined together for predicting the flow and structure behaviors (Baum, 2002; Lohner et al., 2003). A parallel multilevel method for adaptively refined grids was introduced (Aftosmis et al., 2000) to reduce the overall computational effort. Embedded boundaries between the flow and the structure were proposed to effectively transfer information between the two different disciplines. The approach was later extended for unstructured grids to minimize the computational time and memory required for the flow analysis. The examples presented in these references, however, do not include the thermal response of the structure due to the intense aerodynamic heating rate from the high-speed flow.

In the present paper, an integrated flow-thermal-structural analysis approach for predicting each disciplinary behavior and their interaction is

presented. The study of the interactions is a preliminary, but important, step toward the objectives of analyzing more realistic structures, such as thermal protection systems and scramjet engine structures. For high-speed compressible flows, the cell-centered finite-element method (Gnoffo, 1986; Dechaumphai and Limtrakarn, 1999) is combined with an adaptive meshing technique to solve the Navier-Stokes equations. Based on the solution obtained from the previous mesh that could be either the initial or adaptive mesh constructed earlier, the adaptive meshing technique generates an entirely new mesh that consists of small elements in the regions with large change in solution gradients and large elements in the other regions where the change in the solution gradients is small. The combined technique is used to improve the efficiency of the finite-element flow solution and the accuracy of the aerothermal loads, as well as to reduce the computational time and the computer memory. The Galerkin finite-element method is applied to solve the structural energy equation for temperature distribution and the structural equations for deformation and stress. The paper starts by explaining the theoretical formulation of highspeed compressible flow, structural heat transfer, and structural response. Then the solution procedure for flow-thermal-structural interaction problem is presented. The basic idea behind the adaptive meshing technique is then described. The efficiency of the combined procedure, the cellcentered finite-element method and the adaptive meshing technique, is evaluated by solving the Mach 4 flow past a flat plate and comparing results with those obtained from the finite-difference method. The high-speed flow, structural heat transfer, and deformation behaviors are then studied by applying the present method to Mach 10 flow past a flat plate to demonstrate their interdisciplinary coupling.

2. Theoretical Formulation and Solution Procedure

2.1 Governing equations:

The equations for the high-speed compressible

flow, the structural heat transfer, and the structural analysis in two dimensions are described below.

High-speed compressible viscous flow

The equations for high-speed compressible viscous laminar flow are represented by the conservation of mass, momentum, and energy. These equations are written in the conservation form (Hirsch, 1988) as

$$\frac{\partial}{\partial t} \{ U_F \} + \frac{\partial}{\partial x} \{ E_F \} + \frac{\partial}{\partial y} \{ F_F \} = 0 \qquad (1)$$

where the subscript F denotes the fluid analysis. The vector $\{U_F\}$ contains the fluid conservation variables defined by

$$\{ U_F \} = \begin{cases} \rho \\ \rho u \\ \rho v \\ \rho \epsilon \end{cases}$$
 (2)

where ρ is the fluid density, u and v are the velocity components in the x and y directions, respectively, and ε is the total energy. The vectors $\{E\}$ and $\{F\}$ consist of the flux components in the x and y directions, respectively (Dechaumphai and Limtrakarn, 1999).

Structural heat transfer

The thermal response of the structure is described by the energy equation in the conservation form as

$$\frac{\partial}{\partial t}U_r + \frac{\partial}{\partial x}E_r + \frac{\partial}{\partial y}F_r = G_r \tag{3}$$

where the subscript T denotes the structural heat transfer analysis. The vector U_T contains the thermal conservation variable defined by

$$U_{\tau} = \rho c T \tag{4}$$

where c is the specific heat of structure. The heat flux components E_{τ} and F_{τ} are

$$E_T = -k \frac{\partial T}{\partial x}$$
 and $F_T = -k \frac{\partial T}{\partial y}$ (5)

and G_T is the heat source.

Structural response

The structural response is governed by the quasi-static equilibrium equations given by

$$\frac{\partial}{\partial x} \{ E_s \} + \frac{\partial}{\partial y} \{ F_s \} = 0 \tag{6}$$

where the subscript S denotes the structural analysis. The flux vector components $\{E_S\}$ and $\{F_S\}$ are

$$\{E_S\} = \left\{ \begin{array}{c} \sigma_X \\ \tau_{XY} \end{array} \right\} \quad \text{and} \quad \{F_S\} = \left\{ \begin{array}{c} \tau_{XY} \\ \sigma_Y \end{array} \right\} \quad (7)$$

where the stress components σ_x , σ_y , and τ_{xy} are related to the strain and the temperature by the generalized Hook's law (Beer et al., 2002).

2.2 Finite-element formulation:

The cell-centered finite-element method is applied to the Navier-Stokes equations to derive the finite-element equations. The Galerkin finite element approach is applied to the structural heat transfer equation and the equilibrium equations to derive the corresponding finite-element equations. The derivation procedures are briefly described below.

Finite-element flow equations

The method of weighted residuals (Zienkiewicz and Taylor, 2000) is applied to Eq. (1) over the element domain, Ω , by using a unit interpolation function as

$$\int_{\rho} \frac{\partial}{\partial t} \{U_F\} d\Omega = -\int_{\rho} \frac{\partial}{\partial x} \{E_F\} d\Omega - \int_{\rho} \frac{\partial}{\partial y} \{F_F\} d\Omega \quad (8)$$

The Gauss divergence theorem is then applied to the flux integral terms of Eq. (8) to yield,

$$\int_{\Omega} \frac{\partial}{\partial x} \{E_F\} d\Omega + \int_{\Omega} \frac{\partial}{\partial y} \{F_F\} d\Omega = \int_{\Gamma_e} \left(\{G_I\} + \{G_V\} \right) \cdot \hat{n} d\Gamma(9)$$

where the flux vectors $\{G_I\}$ and $\{G_V\}$ are the inviscid and viscous flux vectors of $\{E_I+F_I\}$ and $\{E_V+F_V\}$, respectively, and \hat{n} is the unit vector normal to the element boundary, Γ_e . Equation (9) is evaluated by summing the normal fluxes from all sides, Γ_e , of the element. The fluxes normal to the element sides are then approximated by the numerical inviscid and viscous fluxes, $\{\bar{G}_I\}$ and $\{\bar{G}_V\}$. By applying an explicit time marching algorithm (Hirsch, 1988), Eq. (9) becomes

$$\frac{A_e}{\Delta t} \{ U_F^{n+1} - U_F^n \} = -\sum_{s} \delta_s (\{ \overline{G}_t \} + \{ \overline{G}_t \}) \quad (10)$$

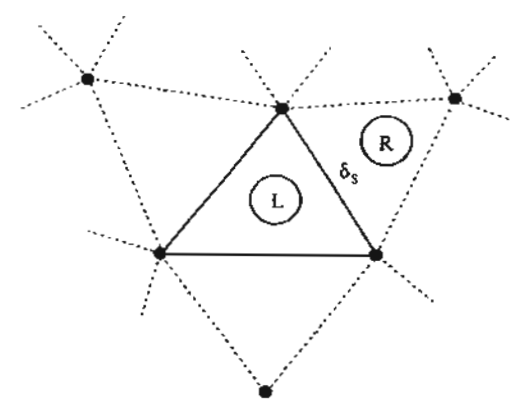


Fig. 1 The side length, δ_S , between the left element (and right element (b).

where U_F^{n+1} and U_F^n are the conservation variables at the time steps n+1 and n, respectively; A_e is the element area; δ_S is the length of the element side being considered as shown in Fig. 1 and the summation is performed for all sides. Δt is the allowable time step following the CFL and viscous stability requirement (Dechaumphai and Limtrakarn, 1999).

The basic concept behind the cell-centered finite-element method used in this paper is to determine the flux across element interfaces by using the Roe's averaging procedure. The average inviscid flux, G_I , is given by

$$\bar{G}_{I} = \frac{1}{2} [G_{I}^{L} + G_{I}^{R} + |A^{\bullet}| (U_{F}^{L} - U_{F}^{R})]$$
 (11)

where the superscripts L and R denote the left and right elements, respectively. The last term in Eq. (11) may be viewed as an artificial diffusion needed for the solution stability. This diffusion is represented by the product of the Jacobian matrix $[A^*]$ and the difference between the left and right element conservation variables U_F^L and U_F^R (Limtrakarn and Dechaumaphai, 2003).

The average viscous flux, G_V , in Eq. (10) normal to the element edge and its components consist of the stress and heat flux components that are in the form of the first-order derivative of u, v, and T (Hirsch, 1988). These derivative terms are computed from the nodal variable gradients. As an example, the temperature gradient at node K in Fig. 2, $\partial T_K/\partial x$, can be determined as follows. First, the temperature gradient of an ele-

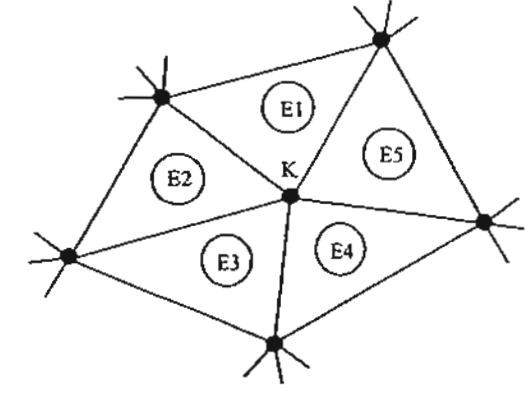


Fig. 2 Node K is surrounded by a number of elements

ment can be expressed as,

$$\frac{\partial T}{\partial x} = \lfloor N \rfloor \left(\frac{\partial T}{\partial x} \right) \tag{12}$$

where $\lfloor N \rfloor$ is the element interpolation function matrix. The method of weighted residuals is applied to Eq. (12) to yield,

$$\int_{\mathcal{Q}} \{N\} \frac{\partial T}{\partial x} d\mathcal{Q} = \int_{\mathcal{Q}} \{N\} \lfloor N \rfloor \left\{ \frac{\partial T}{\partial x} \right\} d\mathcal{Q} \quad (13)$$

Integration by parts is then applied to the integral term on the left-hand-side of Eq. (13).

$$[M] \left\{ \frac{\partial T}{\partial x} \right\} = \int_{\Gamma_e} \hat{n} \ T_s \{ N \} d\Gamma - \int_{\Omega} \left\{ \frac{\partial N}{\partial x} \right\} T \ d\Omega (14)$$

where T_s is the temperature of the boundary, and

$$[M] = \int_{\Omega} \{N\} \lfloor N \rfloor d\Omega \qquad (15a)$$

For the explicit algorithm, the consistent matrix, [M], in Eq. (15a) is written in the form of the lumped mass matrix, $[M]_{\text{tumped}}$, given by,

$$[M]_{\text{tumped}} = \frac{A_e}{3} \begin{bmatrix} 1 & 0 & 0 \\ 0 & 1 & 0 \\ 0 & 0 & 1 \end{bmatrix}$$
 (15b)

Then, Eq. (14) becomes,

$$\left(M_{\text{RUMPed}}\right)_{K} \frac{\partial T}{\partial x}\Big|_{K} = \int_{\Gamma_{d}} \hat{n} T_{S} N_{K} d\Gamma - \int_{\Omega} \frac{\partial N_{K}}{\partial x} T d\Omega \tag{16}$$

Also, the average temperature gradient at node K is computed from the contribution of the surrounding elements as,

$$\sum_{E} (M_{\text{lumped}})_{K} \frac{\partial T}{\partial x} \bigg|_{K} = \sum_{E} \int_{\Gamma_{K}} \hat{n} T_{S} N_{K} d\Gamma - \sum_{E} g \frac{\partial N_{K}}{\partial x} T dQ$$
(17)

The other derivative terms needed for computing the stress and heat flux components can be derived using the same procedure above.

By substituting Eq. (11) into Eq. (10), then Eq. (10) becomes

$$\frac{A_{e}}{\Delta t} \{ U_{F}^{n+1} - U_{F}^{n} \} = -\frac{1}{2} \sum_{S} \delta_{S} [\{ G_{I}^{L} \} + \{ G_{I}^{R} \} + | A^{\bullet} | (\{ U_{F}^{L} \} - \{ U_{F}^{R} \})] \\
- \sum_{F} \delta_{S} \{ \widetilde{G}_{F} \}$$
(18)

Finite-element structural heat transfer equations

The method of weighted residuals is applied to Eq. (3), over the element domain, \mathcal{Q} , by assuming a linear distribution of the conservation variable, U_T , and the flux components E_T and F_T in the form.

$$U_{\tau}(x, y, t) = [N(x, y)] \{ U_{\tau}(t) \}$$
 (19a)

$$E_{\tau}(x, y, t) = |N(x, y)| \{E_{\tau}(t)\}$$
 (19b)

$$F_T(x, y, t) = |N(x, y)| \{F_T(t)\}$$
 (19c)

where [N(x, y)] is the linear interpolation function matrix. The finite-element equations can then be derived in the form:

$$[M] \{ \Delta U_T \}^{n+1} = \{ R_T \}_T^n + \{ R_T \}_2^n$$
 (20)

where [M] is the mass matrix, and $\{\Delta U_T\}^{n+1} = \{U_T\}^{n+1} - \{U_T\}^n$ at time n+1. The $\{R_T\}_1^n$ and $\{R_T\}_2^n$ vectors are associated with the thermal fluxes within each element and across the element boundary, respectively, and are given by,

$$\{R_{T}\}_{1}^{n} = \int_{\Omega} \left\{ \frac{\partial N}{\partial x} \right\} [N] dQ \{E_{T}^{n}\}$$

$$+ \int_{\Omega} \left\{ \frac{\partial N}{\partial y} \right\} [N] dQ \{F_{T}^{n}\}$$
(21)

$$\{R_T\}_2^n = -\int_{\Gamma} \{N\} (E_T^n n_x + F_T^n n_y) d\Gamma$$
 (22)

Finite-element structural equations

The Galerkin finite-element method is applied to Eq. (6) in the same fashion as in the structural heat transfer analysis. The finite-element equations can also be derived in the form:

$$[K]\{U_s\} = \{R_s\} + \{R_T\}$$
 (23)

where [K] is the stiffness matrix, $\{U_S\}$ is the nodal displacement vector, $\{R_S\}$ is the external load vector, and $\{R_T\}$ is the thermal load vector.

These matrices are defined by

$$[K] = \int_{\Omega} [B]^r [C] [B] d\Omega \qquad (24)$$

$$\{R_s\} = \int_{\Gamma_s} [N]^T \{F_s\} d\Gamma \qquad (25)$$

$$\{R_T\} = \int_{\Omega} [B]^T [C] \{\alpha\} (T - T_0) d\Omega \qquad (26)$$

where [B] is the strain-displacement interpolation matrix, [C] is the elastic modulus matrix, $\{F_5\}$ is the surface traction matrix, $\{\alpha\}$ is the thermal expansion coefficient vector, and T_0 is the reference temperature for zero stress state.

2.3 Solution sequence

For high-speed compressible flows, the flow behavior normally approaches a steady state much faster than that of the thermal and structural response of the structure. Typically, the heating rate approaches a steady state in about few milliseconds. At this time, the structural configuration remains nearly undeformed at a temperature only slightly higher than the initial temperature. After few seconds, the structural temperature begins to rise appreciably and significant deformation may occur. At this time, thermal and deformation coupling effect can alter the flow field. The coupling effect continues to alter the flow and structure behavior until the structure reaches the state of the thermal equilibrium.

Based on the fact that the high-speed flow behavior normally reaches the steady-state condition in a much shorter time than the structural response, the analysis procedure of the flowstructure interaction presented in this paper consists of the solution sequence as described by Fig. 3. This solution sequence can reduce the total computational time by avoiding detailed transient flow analysis that requires significant computational effort (Limtrakarn, 2003). At the initial time, $t=t_0$, the adaptive cell-centered finite-element method is first used to predict the highspeed flow behavior as denoted by FA (Flow Analysis). The flow analysis generates aerothermal loads that include heating rate and pressure along the structural surface. After a short interval of time at $t=t_1$, the predicted aerodynamic heat-

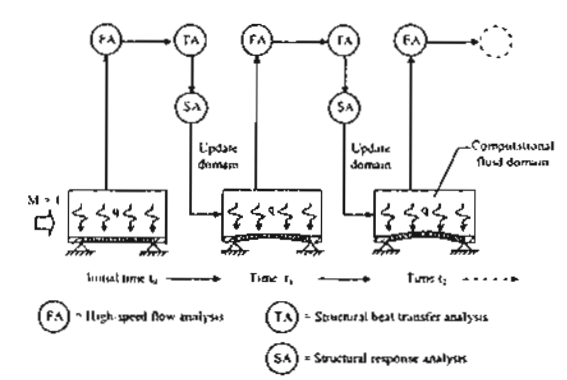


Fig. 3 Solution sequence of flow-structure interaction for high-speed flow over a flat plate

ing rate is applied to the structural configuration and the structural heat transfer analysis as denoted by TA (Thermal Analysis) is used to solve the structural temperature. Both the structural temperature and the fluid pressure are then used to predict the structural response for deformation and stresses as denoted by SA (Structural Analysis). The same sequence is repeated to predict the new flow field behavior, the aerothermal loads, the structural temperature, as well as the new structural deformation and stresses.

3. Adaptive Meshing Technique

Adaptive mesh generation techniques may be classified into two major categories: 1) refinement/derefinement, and 2) remeshing. The first category, the adaptive refinement/ derefinement technique, can be further classified into three subcategories: a) the h method, b) the p method, and c) the r method. In the h method, the elements in the initial mesh are refined into smaller elements or derefined into larger elements (Ramakrishnan et al., 1990). The p method maintains the geometry of the elements of the initial mesh but increases (or decreases) the order of the polynomials used for the element interpolation functions (Dechaumphai, 1982). The r method keeps the number of elements and their connectivities the same but relocates the nodes (Lohner et al., 1984).

The remeshing technique, the second adaptive mesh-generation category, generates an entirely

new mesh based on the solution obtained from an carlier mesh (Dechaumphai, 1995; Peraire et al., 1987). The technique is combined with the cellcentered finite-element method in this paper to obtain solutions of high-speed compressible flow problems. The idea is to construct a new mesh that consists of small elements in the regions with large change in solution gradients and large elements in the other regions where the changes in the solution gradients are small. As an example, small elements are needed in the regions of shock waves to capture shock resolution, whereas larger elements can be used in the free-stream region because the flow behavior is uniform. To determine proper element sizes at different locations in the flow field, the solid-mechanics concept of determining the principal stresses from a given state of stresses at a point is employed. Since the fluid density changes abruptly across the shock waves, thus the density distribution can be used as an indicator for the determination of proper element sizes.

Because small elements must be placed in the region of the shock wave where large changes in the density gradient occur, the second derivatives of the density at a point with respect to global x and y coordinates are needed to compute,

$$\begin{bmatrix} \frac{\partial^2 \rho}{\partial x^2} & \frac{\partial^2 \rho}{\partial x \partial y} \\ \frac{\partial^2 \rho}{\partial x \partial y} & \frac{\partial^2 \rho}{\partial y^2} \end{bmatrix}$$
(27)

Then the principal quantities in the principal X and Y directions, where the cross-derivatives vanish, are determined,

$$\lambda_1 = \left| \frac{\partial^2 \rho}{\partial X^2} \right|$$
 and $\lambda_2 = \left| \frac{\partial^2 \rho}{\partial Y^2} \right|$ (28)

These principal quantities are then used to compute proper element sizes, h_1 and h_2 , in the two principal directions using the following condition (Oden and Carey, 1981),

$$h_1^2 \lambda_1 = h_2^2 \lambda_2 = \text{constant} = h_{\min}^2 \lambda_{\max}$$
 (29)

where h_{min} is the specified minimum element size, and λ_{max} is the maximum principal quantity for the entire model.

Based on the condition in Eq. (29), the element

sizes are generated according to the given minimum element size h_{min} . Specifying too small h_{min} may result in a model with an excessive number of elements. On the other hand, specifying too large hmin may result in an inadequate solution accuracy or excessive analysis and meshing cycles. These factors must be considered prior to generating a new mesh. Note that, because the technique generates an entirely new mesh with different nodal locations from the old mesh, interpolation of the solution from the old to the new mesh should be used to increase the analysis solution convergence.

4. Applications

A Mach number 4 flow past a flat plate is presented as the first example to validate the adaptive cell-centered finite-element method for highspeed flow analysis and to compare the results with those obtained from the finite-difference method. Then the performance of the proposed high-speed flow-structure interaction procedure is evaluated by Mach number 10 flow past a flat plate.

4.1 Mach 4 flow past a flat plate:

The problem statement of a mach 4 flow past a flat plate as shown in Fig. 4 was taken from a reference (Anderson, 1995) that presents the analysis solution by using the finite-difference method. The flow enters through the left boundary of the computational fluid domain. The shock wave

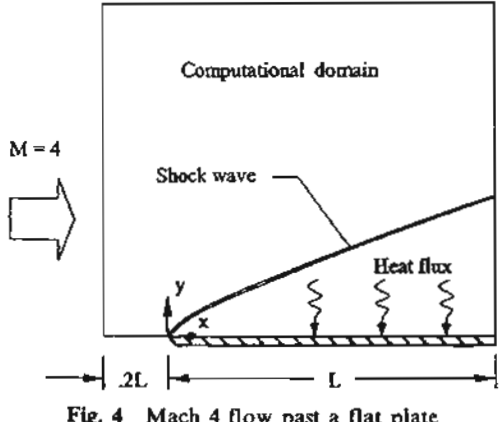
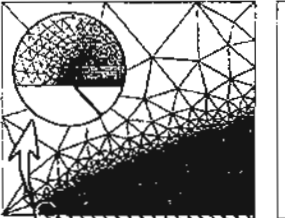


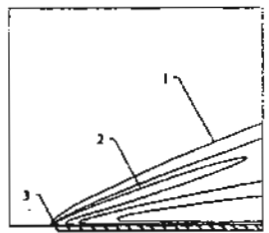
Fig. 4 Mach 4 flow past a flat plate

is created from the leading edge as highlighted in the figure. The inlet flow conditions consist of specifying $\rho = 1.2252 \text{kg/m}^3$, u = 1.36 tm/s, v = 0, $\varepsilon = 1.133,080 \text{J/kg}$, Re = 932 with the wall temperature of 288.16K. The combined method of the cell-centered finite-element analysis and the adaptive meshing technique is applied to solve the problem. Figure 5(a) shows the final adaptive mesh that consists of small elements clustered along the shock line from the sharp leading edge. The accuracy of the shock resolution and the shock angle strongly depends on the finite element mesh near the sharp leading edge. To capture the acrodynamic heating rate accurately, graded quadrilateral elements normal to the flat plate are generated to capture the thin boundary layer along the flat plate and in the leading edge region as shown in the figure. The total of 10,353 triangular elements are generated in the inviscid region and 4,011 quadrilateral elements in the boundary layer. Figure 5(b) shows the predicted density contours with high value at the leading edge.

As the flow encounters the leading edge, the fluid particles stop at the leading edge stagnation point. The oncoming freestream thus sees the leading edge as a blunt body. A viscous boundary layer region is then created between the plate and the induced shock wave. The lost kinetic energy from viscous dissipation then transforms into the internal energy, causing aerodynamic heat transfer rate and changing flow field temperature in the boundary layer region.

The predicted u-velocity distribution is normalized with the freestream velocity, u., and





(a) Final adaptive mesh (b) Density distribution (kg/m³)

Fig. 5 Final adaptive mesh and corresponding density contours for mach 4 viscous flow past a flat plate

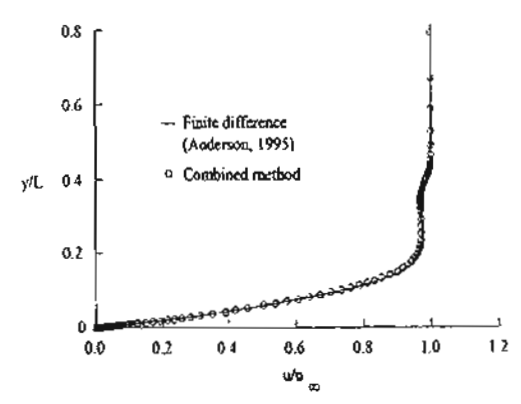


Fig. 6 Comparative normalized u-velocity distributions along normalized y distance at the flow exit (x=L) for mach 4 viscous flow past a flat plate

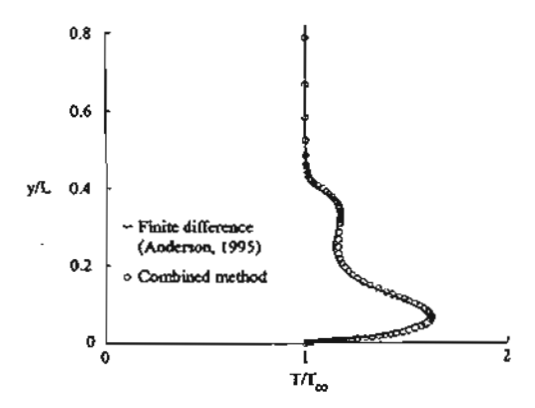


Fig. 7 Comparative normalized temperature distributions along normalized y distance at the flow exit (x=L) for mach 4 viscous flow past a flat plate

compared with the finite difference solution along the y-direction at the flow exit as shown in Fig. 6. The figure shows good agreement between the finite-element and the finite-difference solutions. At the flow exit, the u-velocity decreases slightly across the plate shock wave, and then reduces abruptly within the thin boundary layer to zero at the plate surface.

The predicted temperature distribution is normalized and compared with the finite difference solution along the y-direction at the same flow exit location as shown in Fig. 7. The figure shows the flow temperature increases slightly across the plate shock wave. The flow temperature then increases again before decreasing rapidly to the

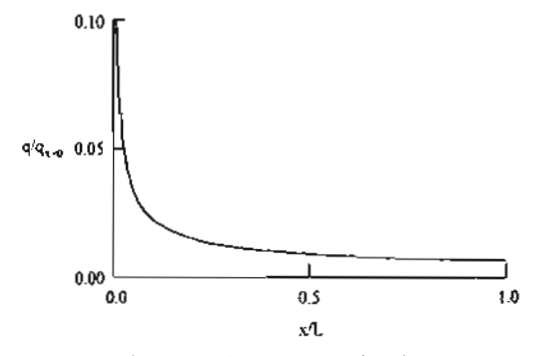


Fig. 8 Predicted heating rate distribution along the plate for mach 4 viscous flow past a flat plate

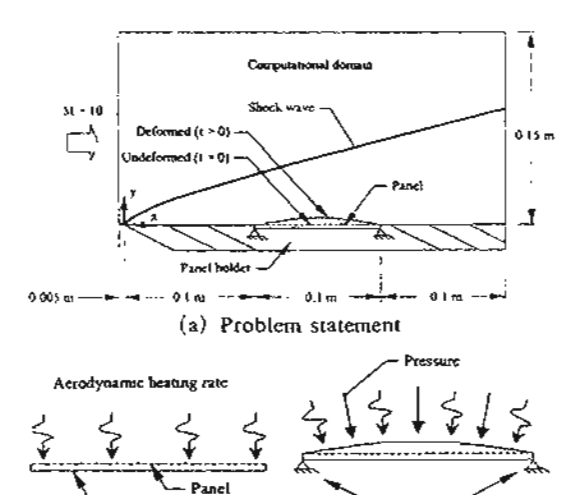
plate temperature within the thin boundary layer. Such steep flow temperature gradient next to the plate thus introduces aerodynamic heating rate on the plate.

The comparison between the two solutions shows good agreement with high temperate gradient in the thin thermal layer near the plate. The predicted flow temperature for the elements near the plate is also used to compute the temperature gradient and then the heating rate that occurs on the plate. Figure 8 shows the computed heating rate distribution along the plate, showing high value at the leading edge. Small quadrilateral elements are needed in the thin boundary layer to provide accurate heating rate solution. The example highlights the benefit of the adaptive meshing technique that can generate proper element sizes automatically to provide high solution accuracy with reduced total number of unknowns and thus the computational time.

4.2 Mach 10 flow past a flat plate:

The performance of the high-speed flow-structure interaction analysis procedure is evaluated by the example of Mach 10 flow past a flat plate as illustrated in Fig. 9. The flow enters through the left boundary of the computational fluid domain and creates a shock wave from the leading edge as highlighted in the figure. The inlet flow conditions consist of specifying $\rho=4.303\text{E}-05\text{kg/m}^3$, u=1,418.7m/s, v=0, $\varepsilon=1,043,000\text{J/kg}$, Re=5, 580 with the wall temperature of 288.16K. The flow-thermal-structural interaction of the flat plate was analyzed using the solution sequence

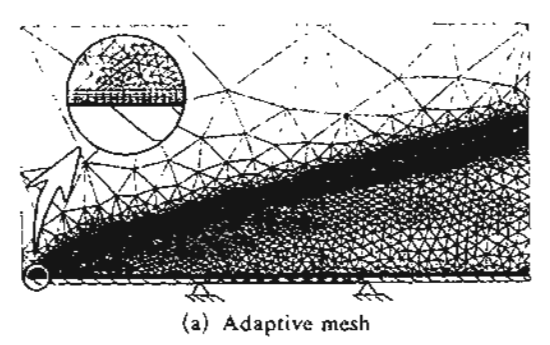
Fixed constrain

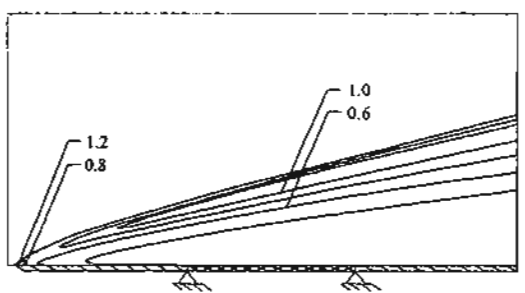


(b) Boundary condition for (c) Boundary condition for heat transfer analysis structural analysis

Fig. 9 Mach 10 flow past a flat plate

shown in Fig. 3. At the initial time, t=0 second, the flow field behavior is predicted by using the cell-centered finite-element method. Based on this flow solution, the adaptive meshing technique as described in the preceding section is then applied to obtain the adaptive mesh as shown in Fig. 10(a). Small elements are automatically generated along the shock line to improve shock resolution and larger elements in other regions. A total of 13,727 triangular elements are generated in the inviscid region and 7,560 quadrilateral elements inside the boundary layer. Ten graded layers of quadrilateral elements are used inside the boundary layer to capture steep temperature gradients for the accurate aerodynamic heating rate prediction. The predicted flow solution is shown by the density contours in Fig. 10(b). With the predicted aerodynamic heating rate from the flow analysis at time t=2 seconds, the structural heat transfer analysis is used to predict the temperature distribution on plate surface between 0.1 < x < 0.2m. At the same time, the quasi-static structural analysis is performed to compute the corresponding structural deformation. The computational fluid domain is then updated by the deformed plate and the cell-centered finite-element method is applied to predict the new flow field behavior. The adaptive meshing technique is





(b) Density distribution $(x10^{-4} \text{kg/m}^3)$

Fig. 10 Adaptive mesh and corresponding density contours for Mach 10 flow past a flat plate at t=0 sec

again applied to generate the new adaptive mesh as shown in Fig. 11(a). The shock pattern is altered by the convex deformation of the plate surface while small elements are automatically clustered to capture the new shock pattern. The corresponding fluid density contours are shown in Fig. 11(b). The fluid density increases through the shock wave and decreases as the fluid flows across the convex center of the plate along the left support toward the right support. The entire analysis procedure is repeated to compute the plate deformation shape and the new flow field behavior at time t=4 seconds as shown in Fig. 12. The figure shows the development of the shock emanating from the left support on the windward side of the deformed plate. As the plate deforms into the flow field, the boundary layer thickness is altered over the plate, becoming thinner after the flow encounters the left support and then it is thicker as the flow approaches the right support of the plate. Figures 13 and 14 compare the predicted aerodynamic heating rates and the pressures, respectively, for 0 < x < (0.3 m.The effect of both the fluid/plate heat transfer and

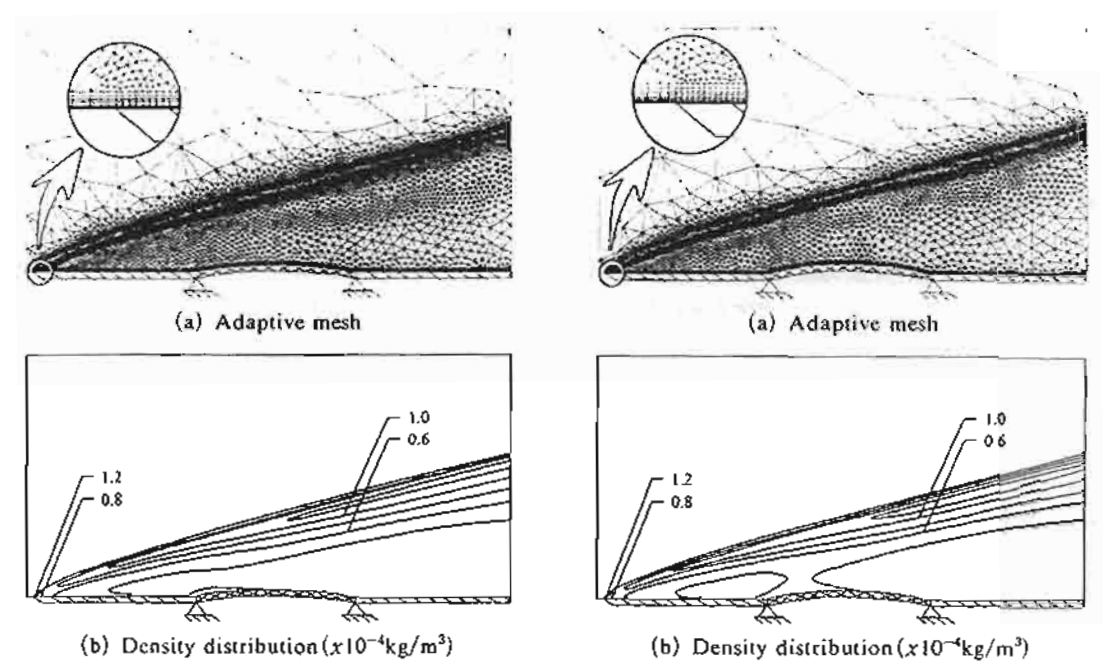


Fig. 11 Adaptive mesh and corresponding density contours for Mach 10 flow past a flat plate at $t=2\sec$

Fig. 12 Adaptive mesh and corresponding density contours for Mach 10 flow past a flat plate at $t=4\sec$

the plate deformation causes the heating rate and the pressure to increase for 0.1 < x < 0.2 as shown in the figures. The change in heating rates at x = 0.1 and 0.2m. is associated with the boundary thinning and thickening, respectively. These figures highlight the interdisciplinary coupling between the flow field and the deformed plate. The heated plate can deform into the flow field, and at the same time, the altered flow field can change the aerothermal loads of the heating rate and the pressure on the plate.

5. Concluding Remarks

The multidisciplinary interaction behaviors of high-speed compressible flow, structural heat transfer, and structural response were presented using the adaptive finite-element method. The finite-element method based on the cell-centered algorithm was used to predict the high-speed compressible flow behavior. The method was combined with the adaptive meshing technique to improve the flow accuracy. The technique generates an entirely new mesh based on the solution

obtained from the previous mesh. The new mesh consists of the clustered elements in the region with large change in the solution gradients to provide the high accuracy, and large elements are generated in the other regions to minimize the computational time and computer memory. The Galerkin finite-element method was used to predict the structural heat transfer and structural response behaviors. The finite-element formulation, the computational procedure and the basic idea behind the adaptive meshing technique were described. The Mach 4 flow past a flat plate was the first example used to validate the high-speed flow solution by comparing results with those obtained from the finite-difference method. Both solutions were found to be in good agreement. The Mach 10 flow past a flat plate was then used to study the flow-structure interaction and to evaluate the performance of the proposed analysis procedure. The later example highlights the interaction behavior between the high-speed flow and the thermal-structural response of the structure. These examples demonstrate the capability of the proposed high-speed compressible viscous

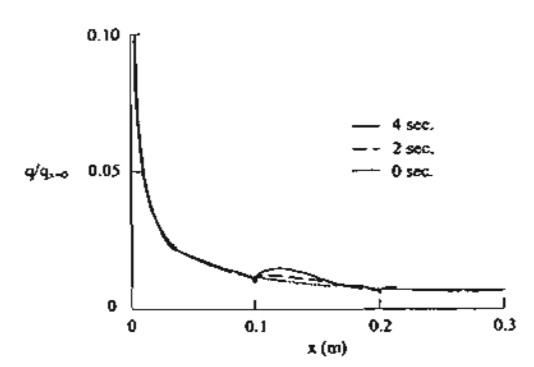


Fig. 13 Heat flux distributions for Mach 10 flow past a flat plate

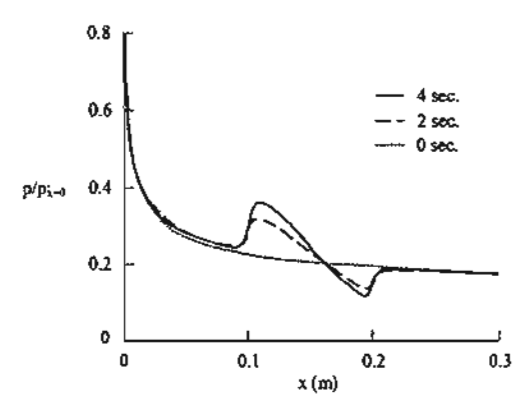


Fig. 14 Pressure distributions for Mach 10 flow past a flat plate

flow and the thermal-structural analysis methods for simulating fluid-structure interaction behavior.

Acknowledgement

The authors are pleased to acknowledge Thailand Research Fund (TRF) for supporting this research work.

References

Anderson, J. D. Jr., 1982, Modern Compressible Flow With Historical Prospective, New York: McGraw-Hill.

Anderson, J. D. Jr., 1991, Fundamentals of Aerodynamics, Second Ed., New York: McGraw-Hill.

Anderson, J. D. Jr., 1995, Computational Fluid Dynamics, McGraw-Hill, New York.

Aftosmis, M. J. Berger, M. J. Adomavicius, G., 2000, "A Parallel Multilevel Method for Adaptively Refined Cartesian Grids with Embedded Boundaries," AIAA Paper 2000-0808.

Back, S-C. Kwon, S-B. Lee, B-E, 2003, "An Experimental Study of Supersonic Dual Coaxial Free Jet," KSME International Journal Vol. 17 No. 12: pp. 2107~2115.

Baum, J. D., 2002, "Development of a Coupled CFD/CSD Methodology using an Embedded CSD Approach," Conference on Computational Physics.

Beer, F. P., Johnston, E. R., DeWolf, J. T., 2002, Mechanics of Materials, Third Edition, New York: McGraw-Hill.

Dechaumphai, P., 1982, "Improved Finite Element Methodology for Integrated Thermal-Structure Analysis," NASA CR 3635.

Dechaumphai, P., 1995, "Adaptive Finite Element Technique for Heat Transfer Problems," *Journal of Energy, Heat & Mass Transfer*, Vol. 17, No. 2, pp. 87~94.

Dechaumphai, P. Limtrakarn, W., 1999, "Adaptive Cell-Centered Finite Element Technique for Compressible Flows," Journal of Energy, Heat and Mass Transfer, Vol. 21, pp. 57~65.

Glass, D. E., Merski, N. R., Glass, C. E., 2002, "Airframe Research and Technology for Hypersonic Airbreathing Vehicles," AIAA Paper 2002-5137.

Gnoffo, P. A., 1986, "Application of Program LAURA to Three-dimensional AOTV Flow-fields," AIAA Paper 86-0565.

Hirsch, C., 1988, Numerical Computation of Internal and External Flows. Vol. 1, New York: Wiley.

Kang, H.-K. Tsutahara, M. Ro, K.-D. Lee, Y.-H., 2003, "Numerical Analysis of a Weak Shock Wave Propagating in a Medium Using Lattice Boltzmann Method (LBM)," KSME International Journal Vol. 17 No. 12: pp. 2034~2041.

Kim, H-D. Kashimura, H. Setoguchi, T., "The Self-Induced Oscillations of the Under Expanded Jets Impinging Upon a Cylindrical Body," KSME Iternational Journal Vol. 16 No. 11: pp. 1448~1456.

Limtrakarn, W., 2003, Finite Element Method

for High-Speed Flow-Structure Interaction, PhD thesis, Mechanical Engineering Department, Chulalongkorn University.

Limtrakarn, W. Dechaumphai, P., 2003, "Computations of High-Speed Compressible Flows with Adaptive Cell-Centered Finite Element Method," J Chin Inst Eng., Vol. 26: pp. 553~563.

Lohner, R., Morgan, K., Zienkiewicz, O. C., 1984, "Adaptive Grid Refinement for Compressible Euler and Navier-Stokes Equations," The International Conference on Accuracy Estimates and Adaptive Refinements in Finite Element Computations, Vol. 2: pp. 189-202, New York: Wiley.

Lohner, R. Baum, J. D. Mestreau, E. Sharov, D. Charman, C. Pelessone, D., 2003, "Adaptive Em-

bedded Unstructured Grid Methods," AIAA Paper 03-1116.

Oden, J. T. Carey, G. F., 1981, Finite Elements: Mathematical Aspects. New Jersey: Prentice-Hall.

Peraire, J. Vahjdati, M., Morgan, K., Zienkiewicz, O. C., 1987, "Adaptive Remeshing for Compressible Flow Computation," *J Comput Phys*, Vol. 72, pp. 449-466.

Ramakrishnan, R., Bey, K. S., Thornton, E., 1990, "A Adaptive Quadrilateral and Triangular Finite-Element Scheme for Compressible Flows," *AIAA Journal*, Vol. 28, No. 1, pp. 51 ~ 59.

Zienkiewicz, O. C. Taylor, R. L., 2000, The Finite Element Method. Fifth Ed., Woburn: Butterworth-Heinemann.

บทความทางวิชาการ เรื่อง

Stream Upwind Finite Element Method for Conjugated Heat Transfer Problems

Published in the

Acta Mechanica Sinica Journal

Vol. 21, pp. 436-443

2005

RESEARCH PAPER

Niphon Wansophark · Atipong Malatip Pramote Dechaumphai

Streamline upwind finite element method for conjugate heat transfer problems

Received: 17 November 2004 / Revised: 25 March 2005 / Accepted: 31 March 2005 / Published online: 26 October 2005 © Springer-Verlag 2005

Abstract This paper presents a combined finite element method for solving conjugate heat transfer problems where heat conduction in a solid is coupled with heat convection in viscous fluid flow. The streamline upwind finite element method is used for the analysis of thermal viscous flow in the fluid region, whereas the analysis of heat conduction in solid region is performed by the Galerkin method. The method uses the three-node triangular element with equal-order interpolation functions for all the variables of the velocity components, the pressure and the temperature. The main advantage of the proposed method is to consistently couple heat transfer along the fluid-solid interface. Three test cases, i.e. conjugate Couette flow problem in parallel plate channel, counter-flow in heat exchanger, and conjugate natural convection in a square cavity with a conducting wall, are selected to evaluate the efficiency of the present method.

Keywords Streamline upwind · Conjugate heat transfer · Finite element method

1 Introduction

Conjugate heat transfer problems are encountered in many practical applications, where heat conduction in a solid region is closely coupled with heat convection in an adjacent fluid. There are many engineering problems where conjugate heat transfer should be considered such as heat transfer enhancement by finned surfaces, design of thermal insulation, cooling of nuclear reactor, design of solar collector, etc. Most of the studies in this field, however, employ the finite difference and the finite volume methods as their numerical tools. Vynnycky et al. [1] studied the conjugate problem of forced convection heat transfer from a flat plate using the streamfunction-vorticity formulation based on the finite difference method. Chen and Han [2] derived the solution of a conjugate heat transfer problem using a finite difference SIMPLE-like algorithm. Schäfer and Teschauer [3] used the finite volume method for analysis of both the fluid flow behavior and the solid heat transfer with thermal effect. Horvat and Catton [4] also used the finite volume method to simulate the conjugate heat transfer in an electronic device heat sink. The results from these problems show that both the finite difference and the finite volume methods can perform very well for many problems of interest, but some assumptions on heat transfer coefficients have to be made in order to compute the temperatures along the fluid-solid interface. Furthermore, determination of the unknown temperatures and the heat fluxes at the fluid-solid interface is normally performed in an iterative way, usually via adoption of an artificial heat transfer coefficient.

At present, very few procedures for solving conjugate heat transfer problems by the finite element method have been proposed in the literature. Misra and Sarkar [5] used the standard Galerkin formulation to solve the continuity, momentum and energy equations simultaneously. Cesini et al. [6] employed the streamfunction-vorticity formulation with segregated solution algorithm to study the natural convection from a horizontal cylinder in a rectangular cavity.

In this paper, the streamline upwind finite element method [7] is selected for analyzing conjugate heat transfer problems. The method uses triangular elements with equal-order interpolation functions for the velocity components, the pressure and the temperature. A segregated solution algorithm [8-10] is also incorporated to solve the unknown variables separately for improving the computational efficiency. The main advantages of the proposed scheme can be illustrated and explained by Figs. 1-2. Figure 1 shows typical control volumes of the fluid and solid cells along the fluid-solid interface adopted by the finite volume method. In the figure, the control volumes 1 and 2 are in the fluid region whereas the control volumes 3 and 4 are in the solid region. Because the heat conduction coefficients in the solid and fluid regions are different, the harmonic mean of the heat conduction coefficient along

The English text was polished by Yunming Chen.

N. Wansophark · A. Malatip · P. Dechaumphai (図)
Department of Mechanical Engineering, Faculty of Engineering, Chulalongkorn University, Patumwan, Bangkok, Thailand, 10330

E-mail: fmepdc@eng.chula.ac.th

Tel.: 66-2-218-6621 Fax: 66-2-218-6621

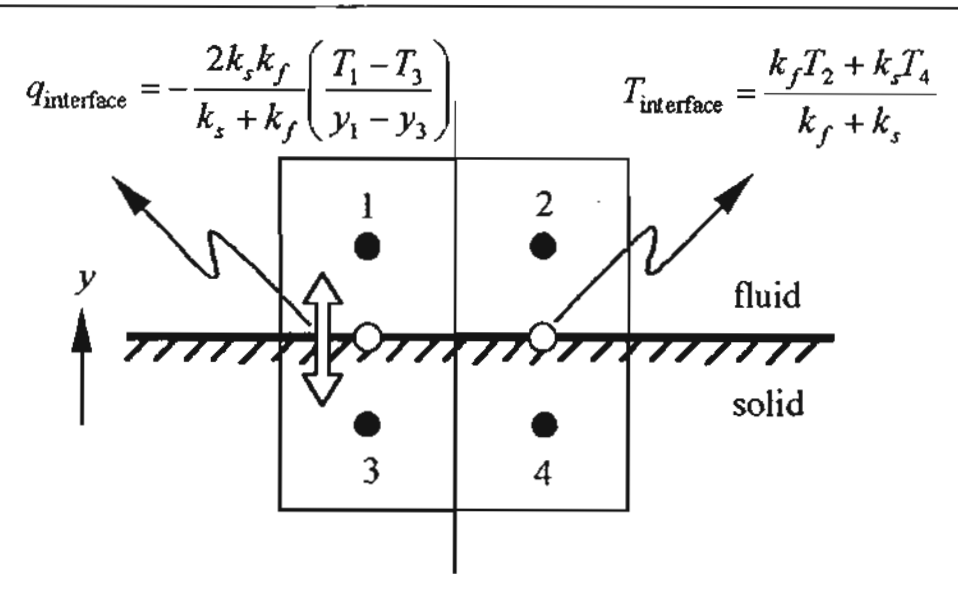


Fig. 1 Control volumes across fluid-solid interface used by the finite volume method

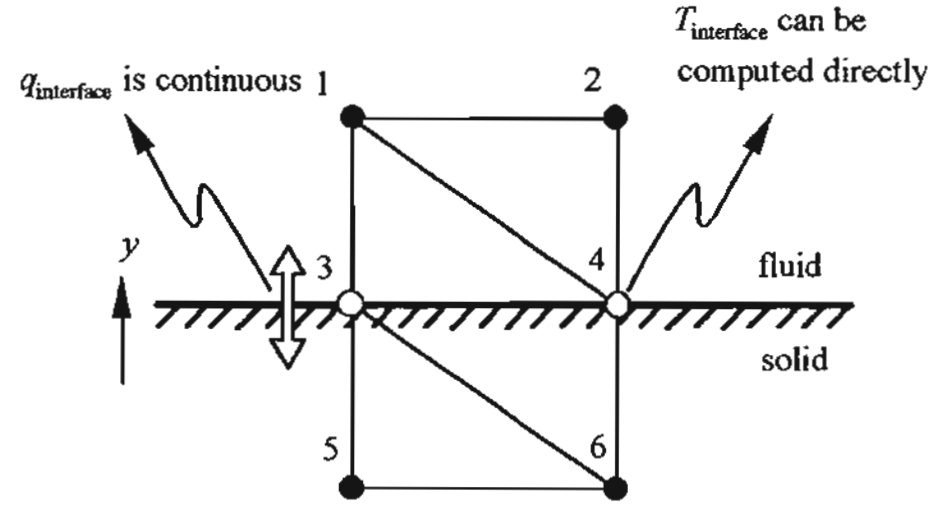


Fig. 2 Elements across fluid-solid interface in finite element method

the fluid-solid interface was introduced and assumed of the following form [11],

$$k_{\text{interface}} = \frac{2k_s k_f}{k_s + k_f},\tag{1}$$

where k_s and k_f are the heat conduction coefficients in the solid and the fluid region, respectively. The heat flux across the fluid-solid interface was then calculated by using the assumed heat conduction coefficient. For the finite element method presented in the paper, the elements along the interface are shown in Fig.2. Employing the finite element method for both the fluid and solid regions with common nodes along the fluid-solid interface provides convenience in analysis and computation. At the same time, the application of the same finite element method in both the regions allows the fluid-solid interface temperatures to be computed directly without assuming the heat transfer coefficient. Furthermore, the continuity of the heat fluxes across the fluid and solid regions along the interface is also automatically preserved.

The paper starts from briefly describing the set of the partial differential equations that satisfy the law of conservation of mass, momentums and energy. Corresponding finite element equations are derived and the element matrices are presented. The computational procedure used for developing appropriate computer program is then described. Finally, the finite element formulation and the computer program are then validated by solving several examples that have exact solution and numerical solutions from other methods.

2 Theoretical formulation and solution procedure

2.1 Governing equations

In this paper, the flow field in fluid region is assumed to be steady, two-dimensional, Newtonian, incompressible and laminar, while the heat transfer in solid region is also assumed to be steady, two-dimensional and isotropic. The fundamental laws used to solve conjugate heat transfer problems consist of: (a) the law of conservation of mass which is called the continuity equation, (b) the law of conservation of momentums, and (c) the law of conservation of energy, as follows:

$$\frac{\partial u}{\partial x} + \frac{\partial v}{\partial y} = 0, (2a)$$

$$\rho \left[u \frac{\partial u}{\partial x} + v \frac{\partial u}{\partial y} \right] = -\frac{\partial p}{\partial x} + \mu \left[\frac{\partial^2 u}{\partial x^2} + \frac{\partial^2 u}{\partial y^2} \right], \tag{2b}$$

$$\rho \left[u \frac{\partial v}{\partial x} + v \frac{\partial v}{\partial y} \right] = -\frac{\partial p}{\partial y} + \mu \left[\frac{\partial^2 v}{\partial x^2} + \frac{\partial^2 v}{\partial y^2} \right] - \rho g (1 - \beta (T - T_0)), \tag{2c}$$

$$\rho c \left[u \frac{\partial T}{\partial x} + v \frac{\partial T}{\partial y} \right] = k \left[\frac{\partial^2 T}{\partial x^2} + \frac{\partial^2 T}{\partial y^2} \right] + \rho Q, \tag{2d}$$

where u and v are the velocity components in the x and y direction, respectively; ρ is the density, p is the pressure, μ is the viscosity, g is the gravitational acceleration constant, β is the volumetric coefficient of thermal expansion, T is the temperature, T_0 is the reference temperature for which buoyant force in the y-direction vanishes, c is the specific heat, k is the coefficient of thermal conductivity and Q is the internal heat generation rate per unit volume. Equation (2d) can also be used for solving heat conduction in the solid by setting both the velocity components, u and v, as zero.

2.2 Finite element formulation

The three-node triangular element is used in this study. The element assumes linear interpolation for the velocity components, the pressure, and the temperature as

$$u(x, y) = N_i u_i, (3a)$$

$$v(x, y) = N_i v_i, \tag{3b}$$

$$p(x, y) = N_i p_i, (3c)$$

$$T(x, y) = N_i T_i, (3d)$$

where i = 1, 2, 3; and N_i is the element interpolation functions.

The basic idea of the solution algorithm proposed in this paper is to use the two momentum equations for solving both of the velocity components, use the continuity equation for solving the pressure, and use the energy equation for solving the temperature in the solid and fluid regions. The finite element equations corresponding to the momentum, the continuity and the energy equations are presented in the next section.

2.2.1 Discretization of the momentum equations

The two momentum equations, Eqs.(2b), (2c), are discretized using the conventional Bubnov-Garlerkin's method. However, a special treatment of the convection terms is incorporated.

These terms are approximated by a monotone streamline upwind formulation for application with triangular elements [9]. In this approach, the convection terms of the form

$$u\frac{\partial\phi}{\partial x} + v\frac{\partial\phi}{\partial y} \tag{4}$$

which are related to the transport variable ϕ , are first rewritten in the streamline coordinates as

$$U_s \frac{\partial \phi}{\partial s}$$
, (5)

where U_s and $\partial/\partial s$ are the velocity and the gradient along the streamline direction, respectively. For pure convection, the term in Eq.(5) is constant along the streamline. These terms are evaluated by a streamline tracing method which keeps track the direction of the flow within the element.

Using the standard Galerkin approach, each momentum equation is multiplied by weighting functions, N_i , and then the diffusion terms are integrated by parts using the Gauss theorem [12] to yield the element equations in the form

$$Au = R_{ox} + R_{u}, (6a)$$

$$Av = R_{py} + R_v + R_b, \tag{6b}$$

where the coefficient matrix A contains the known contributions from the convection and diffusion terms. The load vectors on the right-hand side of Eqs.(6a), (6b) are defined by

$$R_{px} = -\int_{\Omega} N \frac{\partial p}{\partial x} d\Omega, \qquad (7a)$$

$$R_{py} = -\int_{\Omega} N \frac{\partial p}{\partial y} d\Omega, \tag{7b}$$

$$R_{u} = \mu \int_{\Gamma} N\left(\frac{\partial u}{\partial x} n_{x} + \frac{\partial u}{\partial y} n_{y}\right) d\Gamma, \tag{7c}$$

$$R_{v} = \mu \int_{\Gamma} N\left(\frac{\partial v}{\partial x}n_{x} + \frac{\partial v}{\partial y}n_{y}\right) d\Gamma, \tag{7d}$$

$$R_b = -\int_{\Omega} N\{\rho g[1 - \beta(T - T_0)]\} d\Omega,$$
 (7e)

where Ω is the element area and Γ is the element boundary. The element equations are assembled to yield the global equations for the velocity components. Such global equations are then modified for the specified velocity components along the boundaries prior to solving for the new velocity components.

2.2.2 Discretization of the pressure equation

To derive discretized pressure equation, the method of weighted residuals is applied to the continuity equation, Eq.(2a),

$$\int_{\Omega} N_{i} \left(\frac{\partial u}{\partial x} + \frac{\partial v}{\partial y} \right) d\Omega = -\int_{\Omega} \left(\frac{\partial N_{i}}{\partial x} u + \frac{\partial N_{i}}{\partial y} v \right) d\Omega + \int_{\Gamma} N_{i} (u n_{x} + v n_{y}) d\Gamma = 0, \quad (8)$$

where the integrations are performed over the element domain Ω and along the element boundary Γ ; n_x and n_y are

the direction cosines of the unit vector normal to the element boundary with respect to x and y direction, respectively. As mentioned earlier, the continuity equation is used for solving the pressure, but the pressure term does not appear in the continuity equation. For this reason, the relation between velocity components and pressure are required. Such relations can be derived from the momentum equations, Eqs. (6a), (6b) as

$$A_{ii}u_i = -\sum_{j \neq i} A_{ij}u_j + f_i^u - \int_{\Omega} N_i \frac{\partial p}{\partial x} d\Omega, \qquad (9a)$$

$$A_{ii}v_i = -\sum_{j \neq i} A_{ij}v_j + f_i^v - \int_{\Omega} N_i \frac{\partial p}{\partial y} d\Omega, \qquad (9b)$$

where f_i^u and f_i^u are the surface integral terms and the source term due to buoyancy. By assuming constant pressure gradient on an element, we get

$$u_i = \hat{u}_i - K_i^{\rho} \frac{\partial p}{\partial x},\tag{10a}$$

$$v_i = \hat{v}_i - K_i^{\rho} \frac{\partial p}{\partial v},\tag{10b}$$

where

$$\hat{u}_{l} = \frac{-\sum_{j\neq i} A_{lj} u_{j} + f_{i}^{u}}{A_{ll}},$$

$$-\sum_{i} A_{lj} v_{i} + f_{i}^{u}$$
(11a)

$$\hat{v}_i = \frac{-\sum_{j \neq i} A_{ij} v_j + f_i^{u}}{A_{ii}}, \tag{11b}$$

$$K_i^p = \frac{\int_{\Omega} N_i d\Omega}{A_{ii}}.$$
 (11c)

By applying the element velocity interpolation functions, Eqs. (3a), (3b), into the continuity equation, Eq. (8),

$$-\int_{\Omega} \frac{\partial N_i}{\partial x} (N_j u_j) d\Omega - \int_{\Omega} \frac{\partial N_i}{\partial y} (N_j v_j) d\Omega + \int_{\Gamma} N_i (u n_x + v n_y) d\Gamma = 0,$$
 (12)

and introducing the nodal velocities u_j and v_j from Eqs. (10a), (10b), then Eq. (12) becomes

$$\int_{\Omega} \frac{\partial N_{i}}{\partial x} (N_{j} K_{j}^{p}) \frac{\partial p}{\partial x} d\Omega + \int_{\Omega} \frac{\partial N_{i}}{\partial y} (N_{j} K_{j}^{p}) \frac{\partial p}{\partial y} d\Omega
= \int_{\Omega} \frac{\partial N_{i}}{\partial x} (N_{j} \hat{u}_{j}) d\Omega + \int_{\Omega} \frac{\partial N_{i}}{\partial y} (N_{j} \hat{v}_{j}) d\Omega
- \int_{\Gamma} N_{i} (u n_{x} + v n_{y}) d\Gamma.$$
(13)

Finally, by applying the element pressure interpolation functions, Eq. (3c), the above element equations can be written in matrix form with unknowns of the nodal pressures as

$$(K_x + K_y)p = F_u + F_v + F_b,$$
 (14)

where

$$K_{x} = \int_{\Omega} \frac{\partial N}{\partial x} (N_{j} K_{j}^{p}) \frac{\partial N}{\partial x} d\Omega, \qquad (15a)$$

$$K_{y} = \int_{\Omega} \frac{\partial N}{\partial y} (N_{j} K_{j}^{p}) \frac{\partial N}{\partial y} d\Omega, \qquad (15b)$$

$$F_{u} = \int_{\Omega} (N_{j} \hat{u}_{j}) \frac{\partial N}{\partial x} d\Omega, \qquad (15c)$$

$$\boldsymbol{F}_{\boldsymbol{v}} = \int_{\Omega} (N_j \hat{\boldsymbol{v}}_j) \frac{\partial N}{\partial y} d\Omega, \qquad (15d)$$

$$F_b = -\int_{\Gamma} N(u n_x + v n_y) d\Gamma. \tag{15e}$$

The above element pressure equations are assembled to form the global equations, boundary conditions for the specified nodal pressures are imposed prior to solving for the updated nodal pressures.

2.2.3 Discretization of the energy equation

The finite element equations corresponding to the energy equation are derived using an approach similar to that used in deriving element momentum equations. The streamline upwind method is applied to the convection term in the energy equation, Eq. (2d). The standard Galerkin method is then applied to yield the element equations which can be written in matrix form as

$$KT = R + O. ag{16}$$

where the matrix K consists of the known contributions from the convection and diffusion terms, and the load vectors R and Q represent the heat flux along the element boundary and internal heat generation, respectively, as follows:

$$R = k \int_{\Gamma} N \left(\frac{\partial T}{\partial x} n_x + \frac{\partial T}{\partial y} n_y \right) d\Gamma, \tag{17}$$

$$Q = \rho \int_{\Omega} N Q d\Omega. \tag{18}$$

These element equations are again assembled to yield the global temperature equations. Appropriate boundary conditions are applied prior to solving for the new temperature values.

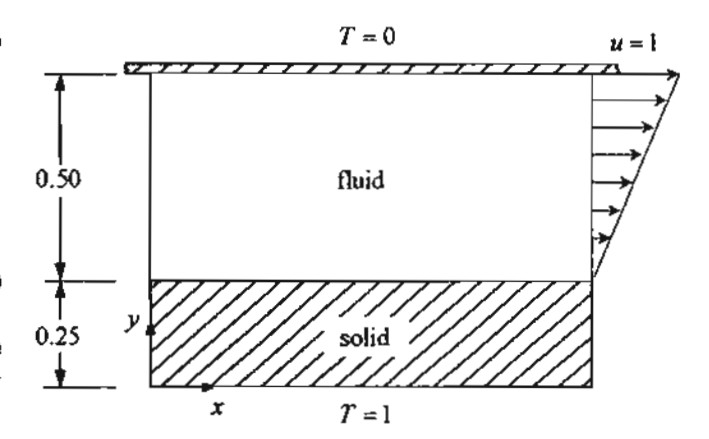


Fig. 3 Conjugate Couette flow problem in parallel plate channel

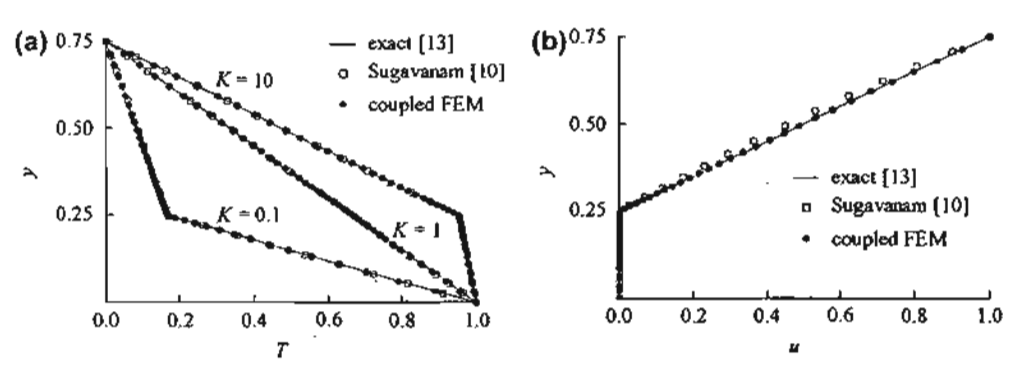


Fig. 4 (a) The temperature profiles, (b) the u-velocity profile for Couette flow problem

2.2.4 Computational procedure

The computational procedure is described in this section. A set of initial nodal velocity components, pressures, and temperatures are first assumed. The new nodal temperatures in both regions are computed simultaneously by using Eq.(16). The new nodal velocity components and pressures are then computed by using Eqs.(6a), (6b) and Eq. (14), respectively. The nodal velocity components are then updated by using Eqs. (9a), (9b) with the computed nodal pressures. This process is continued until the specified convergence criterion is met. Such segregated solution procedure helps reducing the computer storage because the equations for the velocity components, the pressure, and the temperature are solved separately.

3 Results

In this section, three example problems are presented. The first example, conjugate Couette flow problem in a parallel plate channel, is chosen to evaluate the finite element formulation and to validate the developed computer program. The second and the third examples, counter-flow in heat exchanger and conjugate natural convection in a square cavity with a conducting wall, respectively, are used to illustrate the efficiency of the proposed scheme for analyzing conjugate heat transfer problems.

3.1 Conjugate Couette flow problem in a parallel plate channel

The first example for evaluating the finite element formulation and validating the developed computer program is the problem of conjugate Couette flow problem in a parallel plate channel [10]. The problem statement is shown in Fig.3 with a fluid between the upper wall that moves at a constant velocity and is a stationary conducting solid. The other side of the conducting solid is maintained at a constant temperature that is higher than the constant temperature of the opposing channel wall. The numerical results are compared with the numerical results from Sugavanam [10] and the analytical solution given in Ref. [13]. Figure 4 shows that the computational results from the present finite element schemes demonstrate excellent agreement with the analytical solution for varying conductivity ratios $K = k_s/k_f$. The numerical results of the temperatures and the *u*-velocity from the present method are compared within 0.04% and 0.001% of the analytical solutions, respectively, whereas the numerical results of the temperatures and the *u*-velocity from Ref. [10] are compared within 0.5% and 2.0% of the analytical solutions, respectively.

3.2 Conjugate counter flow heat exchanger

To further validate the numerical scheme, a conjugate counter flow heat exchanger problem is selected as the second test case. This heat exchanger consists of two parallel flow passages with widths a_1 and a_3 , separated by a solid plate with thickness of a_2 , as shown in Fig.5. The outer walls of the flow passages are assumed to be adiabatic. The same properties and uniform inlet velocity and temperature profiles are assumed for the hot and cold fluids. The parameters adopted in the computation are as follows, geometrical sizes $a_1 =$ $a_2 = a_3 = 0.1$ and L = 1.0, the flow parameters in upper channel $u_1 = 0.2$, $T_1 = 800$, Re = 133.33 and Pr = 0.75, the flow parameters in lower channel $u_2 = 0.1$, $T_2 = 300$, Re = 66.67 and Pr = 0.75, conduction ratio K = 5. The finite element model, consisting of 1763 nodes and 3360 triangles as shown in Fig.6, is used in this study. Figure 7 shows the predicted temperature contours in the entire domain. The predicted temperature distributions at x = L/2 from presented scheme is compared with the finite volume results from Chen and Han [2] as shown in Fig.8. The figure also shows good agreement between the solutions.

3.3 Conjugate natural convection in a square cavity with a conducting wall

The last example to evaluate the efficiency of the presented scheme, the problem of conjugate natural convection in a square cavity with a conducting wall is selected as shown in Fig.9. The fluid in the cavity is heated from the higher temperature solid wall along the left side and maintained at

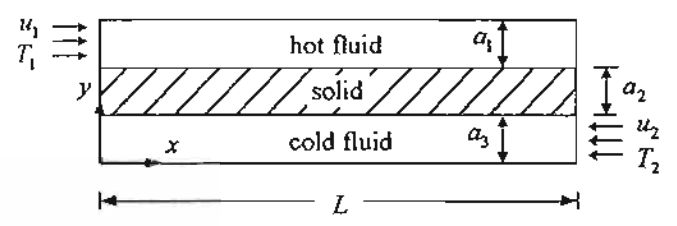


Fig. 5 Conjugate counter flow heat exchanger

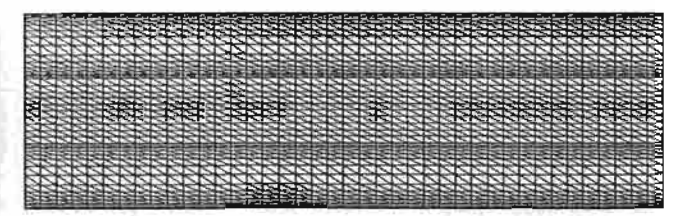


Fig. 6 Finite element model for the conjugate counter flow heat exchanger

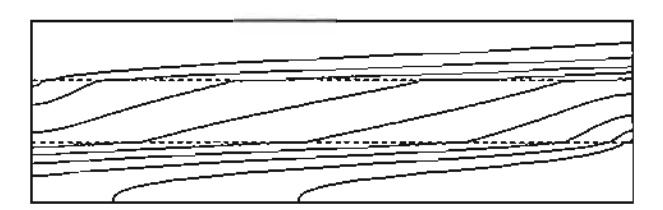


Fig. 7 Predicted temperature contours for the conjugate counter flow heat exchanger

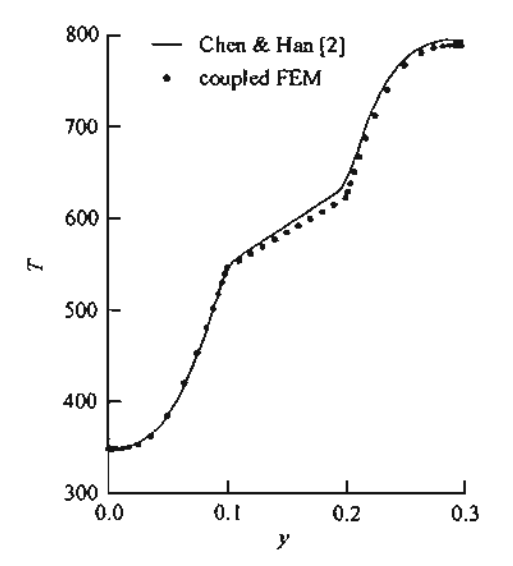


Fig. 8 The temperature profiles at x = L/2 for the conjugate counter flow heat exchanger

zero temperature along the right side, all other boundaries are insulated. The finite element model for both the solid wall and fluid region consists of 2 009 nodes and 3 840 triangles as shown in Fig. 10. Figures 11 and 12 show the predicted streamline and temperature contours for two different thermal conductivity ratios of K=1 and 10 at the Grashof numbers of 10^3 and 10^5 , respectively. The temperature and the heat flux distributions along the fluid-solid interface with the variation

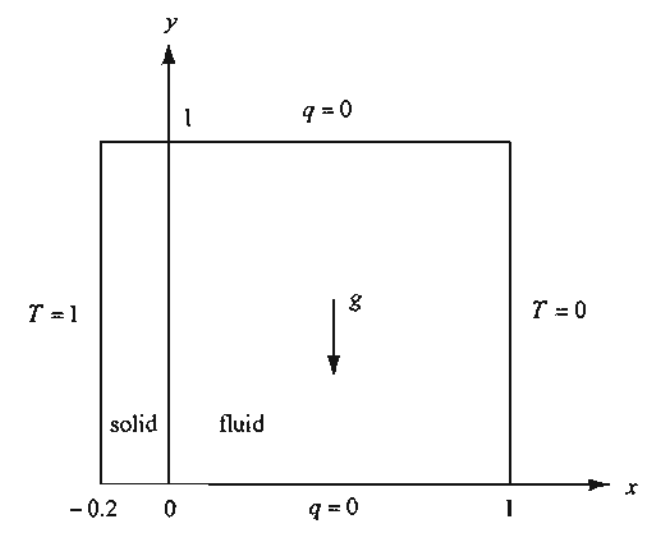


Fig. 9 Conjugate natural convection problem

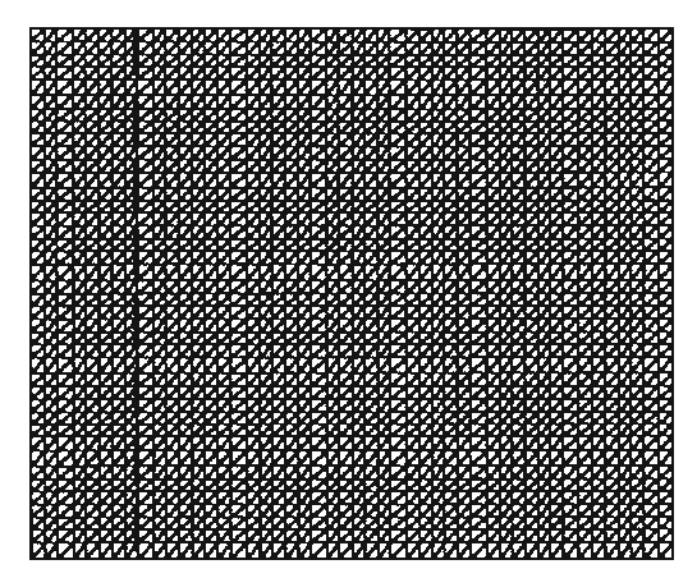


Fig. 10 Finite element model for the conjugate natural convection problem

of conduction ratio K are shown in Figs. 13(a) and 13(b), respectively. In addition, the predicted average Nusselt numbers along the interface, $\overline{Nu}_{x\pm0}$, are compared in Table 1 with the results obtained by Hribersek using boundary-domain integral method [14]. The table shows good agreement of the average Nusselt numbers for both the temperature and heat flux.

4 Conclusions

A coupled finite element method was presented for solving conjugate heat transfer problems. The method combines thermal viscous flow analysis of the fluid region and heat transfer analysis in the solid region together. The finite element formulation and its computational procedure were first described. The flow analysis used a segregated solution algo-

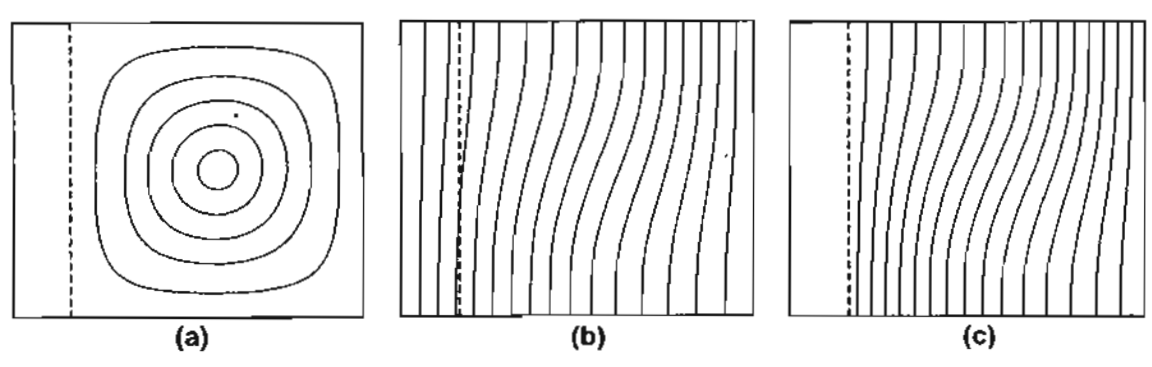


Fig. 11 (a) Streamline contours for K = 10, (b) Temperature contours for K = 1 and (c) Temperature contours for K = 10, all at $Gr = 10^3$

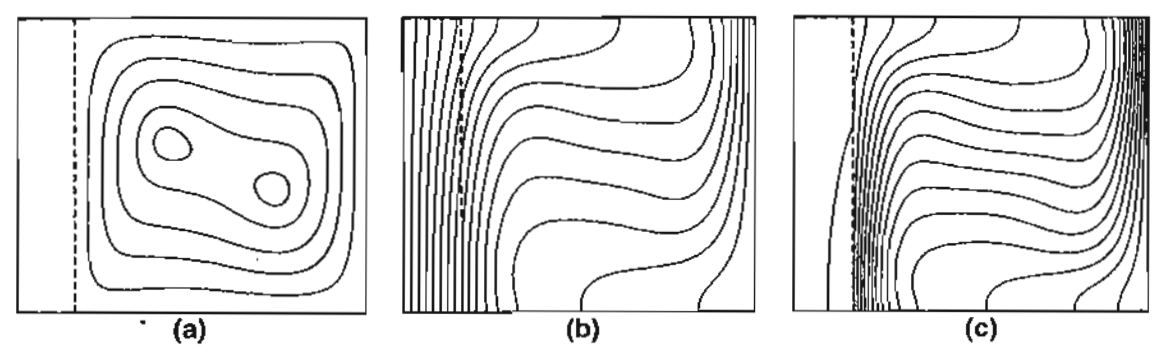


Fig. 12 (a) Streamline contours for K = 10, (b) Temperature contours for K = 1 and (c) Temperature contours for K = 10, all at $Gr = 10^5$

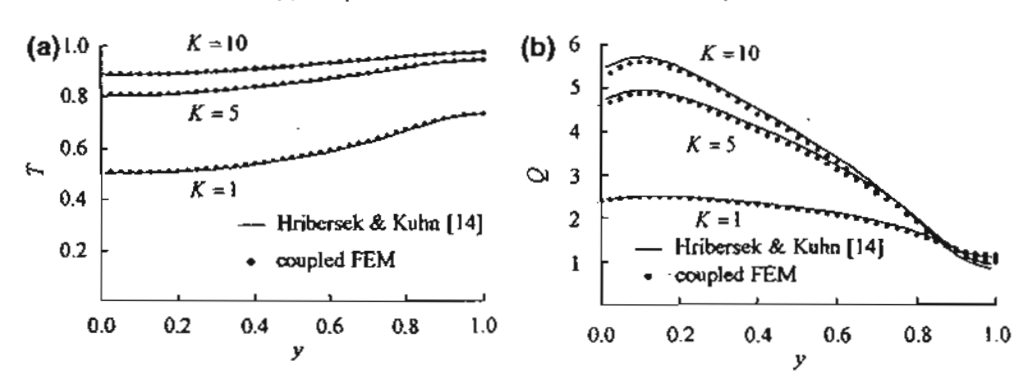


Fig. 13 (a) Interface temperatures and (b) Interface heat fluxes, all at $Gr = 10^5$

Table 1 Variation of the overall Nusselt numbers

		Average Nusselt number along interface (% difference from Ref. [14])		
$K = k_s/k_f$		1		10
$Gr = 10^3$	Hribersek [14]	0.87	1.02	1.04
$Gr = 10^3$	Coupled FEM	0.85 (2.29%)	1.03 (0.98%)	1.04 (0.0%)
$Gr = 10^5$	Hribersek [14]	2.08	3.42	3.72
$Gr = 10^{5}$	Coupled FEM	2.04 (1.92%)	3.30 (3.51%)	3.60 (3.22%)

rithm to compute the velocities, the pressure and the temperature separately for improving computational efficiency. The convection terms in the momentum and the energy equations are treated by the streamline upwind finite element method to suppress the non-physical spatial oscillation in the numerical solutions. All the finite element equations were derived and a corresponding computer program was developed. The efficiency of the coupled finite element method was evaluated

by using several examples and comparing the solutions with those obtained from other methods. These examples highlight the benefits of the combined finite element method that can simultaneously model and solve for solutions in both the fluid and solid regions, as well as to compute the temperatures along the fluid-solid interface directly.

Acknowledgements The authors are pleased to acknowledge the Thailand Research Fund (TRF) for supporting this research.

References

- Vynnycky, M., Kimura, S., Kanev, K., Pop, L.: Forced convection heat transfer from a flat plate: the conjugate problem. Int. J. Heat Mass Transfer 41, 45-59 (1998)
- Chen, X., Han, P.: A note on the solution of conjugate heat transfer problems using SIMPLE-like algorithms. Int. J. Heat Fluid Flow, 21, 463-467 (2000)
- Schäfer, M., Teschauer, I.: Numerical simulation of coupled fluidsolid problems. Comput. Meth. Appl. Mech. Eng. 190, 3645–3667 (2001)
- Horvat, A., Catton, I.: Numerical technique for modeling conjugate heat transfer in an electronic device heat sink, Int. J. Heat Mass Transfer, 46, 2155-2168 (2003)
- Misra, D., Sarkar, A.: Finite element analysis of conjugate natural convection in a square enclosure with a conducting vertical wall. Comput. Meth. Appl. Mech. Eng. 141, 205-219 (1997)
- Cesini, G., Paroncini, M., Cortella, G., Manzan, M.: Natural convection from a horizontal cylinder in a rectangular cavity. Int. J. Heat Mass Transfer, 42, 1801–1811 (1999)
- Wansophark, N., Dechaumphai, P.: Enhancement of streamline upwinding finite element solutions by adaptive meshing technique. JSME Int. J. Series B, 45, 770-779 (2002)

- Choi, H.G., Yoo, J.Y.: Streamline upwind scheme for the segregated formulation of the Navier-Stokes equation. Numer. Heat Transfer. Part B, 25, 145–161 (1994)
- Wansophark, N., Dechaumphai, P.: Combined adaptive meshing technique and segregated finite element algorithm for analysis of free and forced convection heat transfer. Finite Elem. Anal. Desn. 40, 645–663 (2004)
- Sugavanam, R. Ortega, A., Choi, C.Y.: A numerical investigation of conjugate heat transfer from a flush heat source on a conductive board in laminar channel flow. Int. J. Heat Mass Transfer, 38, 2969-2984 (1995)
- Patankar, S. V.: Numerical Heat Transfer and Fluid Flow. New York: McGraw-Hill, 1980
- Zienkiewicz, O.C., Taylor, R.L.: The Finite Element Method. 5th edn. Oxford: Butterworth-Heinemann, 2000
- White, F.M.: Viscous Fluid Flow. 2nd edn. New York: McGraw-Hill, 1991
- Hribersek, M., Kuhn, G.: Conjugate heat transfer by boundarydomain integral method. Eng. Anal. Bound. Elem. 24, 297-305 (2000)

บทความทางวิชาการ เรื่อง

Mixed Entropy Fix Method for Roe's Flux-Difference Splitting Scheme with Automatic Mesh Adaptation

Published in the

Transactions of the Canadian Society for Mechanical Engineering

Vol. 28, No. 3, pp. 531-549

2004

MIXED ENTROPY FIX METHOD FOR ROE'S FLUX-DIFFERENCE SPLITTING SCHEME WITH AUTOMATIC MESH ADAPTATION

Sutthisak Phongthanapanich¹ and Pramote Dechaumphai²
Graduate Student

² Professor (E-mail: fmepdc@eng.chula.ac.th)
(Mechanical Engineering Department, Chulalongkorn University, Bangkok 10330, Thailand)

Received November 2003, Accepted August 2004 No. 03-CSME-55, E.I.C. Accession 2790

ABSTRACT

A combined procedure for two-dimensional Delaunay mesh generation algorithm and an adaptive remeshing technique with higher-order compressible flow solver is presented. The flux-difference splitting scheme with a mixed entropy fix method is introduced for high-speed compressible flow analysis on unstructured meshes. The scheme eliminates unphysical flow solutions such as a spurious bump of the carbuncle phenomenon that occurs on the bow shock from flow over a blunt body, and the oscillation in the odd-even grid perturbation in a straight duct for the Quirk's odd-even decoupling test. The proposed scheme is further extended to achieve higher-order spatial and temporal solution accuracy. The performance of the combined procedure is evaluated by solving several high-speed compressible flow problems on unstructured triangular meshes.

Key words: Adaptive mesh; carbuncle phenomenon; entropy fix; Roe's flux-difference splitting scheme.

METHODE D'ENTROPIE DE MELANGE CONSTANTE POUR LE SCHEMA DE DECOMPOSITION DE DIFFERENCE DE FLUX DE ROE AVEC L'ADAPTATION DE MAILLAGE AUTOMATIQUE

RESUME

On présente une procédure associée pour la formation algorithmique de maillage de Delaunay à deux dimensions et la technique de remaillage adaptatif avec un flux de solution compressible en ordre supérieur. Le schéma de décomposition de différence de flux avec la méthode d'entropie de mélange constante est introduit dans le but d'obtenir une analyse de flux à grande vitesse compressible sur les maillages non-structurés. Le schéma élimine les flux de solutions non-physiques telle qu'une fausse bosse du phénomène d'escarboucle, qui apparaît sur le front de choc venant du flux par dessus un corps émoussé, et l'oscillation de perturbation de la grille nombres impairs - nombres pairs dans un canal direct pour le test de découplage de Quirk nombres impairs - nombres pairs. Ce schéma tend vers l'accomplissement de la solution spatiale et temporelle précise d'ordre supérieur. La performance de la procédure associée est évaluée par la résolution de plusieurs problèmes de flux compressibles à grande vitesse sur les maillages triangulaires non-structurés.

Mots-clés : Maillage adaptatif, phénomène d'escarboucle, entropie constante, schéma de décomposition de différence de flux de Roe

INTRODUCTION

Spatial discretization of a given domain is a prerequisite for numerical simulation of the physical model of the problem. Most of two-dimensional mesh generation schemes, including the method used in this paper, first generate boundary points, then create interior points which are added into the domain if prescribed criterions are satisfied. The point connections by the Delaunay triangulation [1,2] guarantee triangles which are as well shaped as possible for the given set of points. Since the Delaunay triangulation in itself does not include procedures for creating points inside the domain, additional points have to be generated by an automatic point creation algorithm [3-7].

To enhance solution accuracy of the numerical analysis, the mesh adaptation is needed to improve the computed solution [7-13]. An adaptive meshing procedure based on the advancing-front algorithm for computing steady-state and transient solutions of the high-speed compressible flows in two dimensions was presented in Refs. [8-10]. The anisotropic adaptation using unstructured triangular meshes based on the Delaunay criteria was then described in Refs. [11-13] with particular emphasis to fluid flow computations. The process of the adaptive meshing is to first generate initial mesh from the domain, which is used to compute the corresponding solution by the finite element or finite volume method. Then the regions where adaptation is vital are determined by an error indicator, which dictates a close correlation between the size of elements and the behavior of the corresponding computed solution. A new mesh, which is better adapted for the particular problem, is entirely created. The same process is repeated until the specified convergence criterion is met. The performance of the overall procedure is evaluated using computational fluid dynamics test cases.

In this paper, the Delaunay triangulation and the mesh refinement procedure introduced by Marchant and Weatherill [5] are used to generate meshes. The second derivative error indicator [8] is used to determine element sizes for adaptation process. The main objective of the proposed adaptive technique is to overcome any disadvantage of the second derivative error indicator by the virtue of an element size scaling function. Testing criteria are introduced and designed to control the regularity of elements by limiting a range of allowable element sizes in the vicinity of high gradient areas. The algorithm is terminated when the number of inserted points in each iteration is less than some threshold values that can be specified by user.

High-speed compressible flows normally involve complex flow phenomena, such as strong shock waves and shock-shock interactions. Various numerical inviscid flux formulations have been proposed to solve the approximate Riemann problem. Among these formulations, the flux-difference splitting scheme by Roe [14] is widely used due to its accuracy, quality and mathematical clarity. However, the scheme may sometimes lead to unphysical flow solutions in certain problems, such as the carbuncle phenomenon [15] with a spurious bump in the bow shock from flow over a blunt body. In the odd-even decoupling problem [16], an unrealistic perturbation may grow with the planar shock as it moves along the duct. To improve the solution accuracy of these problems, Quirk [16] pointed out that the original Roe's scheme should be modified or replaced by other schemes in the vicinity of strong shock. Harten [17] proposed an entropy fix formulation to replace the near zero small eigenvalues by certain tolerances. The mathematical background of the Harten's entropy fix with the suggested tolerance values is given by Van Leer et al. [18].

This paper modifies the entropy fix method by Van Leer et al. [18] and the multidimensional dissipation technique of Pandolfi and D'Ambrosio [19] for unstructured triangular meshes and implemented into the original Roe's scheme. The presented scheme is further extended to achieve higher-order solution accuracy and then evaluated by several benchmark test cases.

The presentation in this paper starts by describing adaptive remeshing technique with the implementation procedure in an objected-oriented programming concept. Next, the Roe's flux-difference splitting scheme with some well-known problems that exhibit numerical shock instability is described. A Roe's scheme with a mixed entropy fix method is then proposed and examined for its capabilities. The presented scheme with the improved higher-order solution accuracy is then explained. Finally, the combined procedure is evaluated by several high-speed compressible flow benchmarks on both structured and adaptive unstructured meshes.

MESH ADAPTATION TECHNIQUE FOR EULER SOLUTIONS

The Delaunay triangulation employed in this paper follows the Bowyer-Watson algorithm [1,2], and the automatic point creation by Marchant and Weatherill [5] is used to generate points inside the domain. The step-by-step explanation of these algorithms were presented in detail in Ref. [7].

Adaptive mesh regeneration

In high-speed compressible flows, the flow properties, such as the density and pressure, change abruptly across the shock waves. Small elements are thus needed along the shock waves to provide good result resolution. The second derivatives of any key variable ϕ , such as density is used to determine the proper element sizes [8]; that is, small elements are placed in the region where changes in the variable gradients are large. Elements, which will be either refined or coarsened by AdaptiveRemeshing algorithm, are identified by a dimensionless error indicator using the pressure-switch coefficient [9]. The indicator at node I is given by,

$$E_{I} = \frac{\sum_{e \in I} \left| 2\phi_{I} - \phi_{J} - \phi_{K} \right|}{\sum_{e \in I} \left(A^{*} + B^{*} \right)} \tag{1}$$

where J and K are the other two nodes of the triangle, $A^* = \max(|\phi_I - \phi_J|, \alpha(\phi_I + \phi_J))$ and $B^* = \max(|\phi_I - \phi_K|, \alpha(\phi_I + \phi_K))$. The value of α is prescribed as .005 in this paper, which means $A^* = .005(\phi_I + \phi_J)$ and $B^* = .005(\phi_I + \phi_K)$ if ϕ_J and ϕ_K are within 1% of ϕ_I , respectively.

Practical experience found that this type of error indicator for complex high-speed compressible flow problems, where regions such as shock or discontinuity have different strength, may cause inaccurate solution from inadequate refinement because the point spacing is scaled according to the maximum value of the second derivatives. To overcome this problem, an element size scaling function, which scales the point spacing of point p_i

between minimum and maximum element sizes, h_{min} and h_{max} , within the range of χ_{min} and χ_{max} , has been used,

$$\chi_i = \text{ScaleRange}\left(\frac{h_{max} - dp_i}{h_{max} - h_{min}}, 0, 1, \chi_{min}, \chi_{max}\right)$$
(2)

where dp_i is nodal distribution value of node i [7].

The coefficient χ_i controls the point insertion in the regions of high solution gradient and eliminates undue distortion of the triangle regularity. The value of χ_{\min} limits number of points insertion in high gradient region such as shock, while the value of upper limit χ_{\max} allows more points to be inserted into the lower solution gradient region. As shapes of adapted elements generated by this function may be distorted, the Alpha and Beta coefficients [5] are incorporated as coefficients of such function to control point density and the regularity of triangulation.

The proposed adaptive mesh regeneration is based on the concepts of the Delaunay triangulation and the mesh refinement as described by Algorithm I and II [7]. The new mesh is constructed using the information from the previous or background mesh, such that it is composed of small elements in the regions with large changes of solution gradients, and large elements in the other regions where the changes of solution gradients are small. The proposed algorithm is terminated when number of inserted points in each iteration is less than some *threshold* values, between 2 to 5 points. Detailed process of adaptive remeshing technique is shown and described in the algorithm as follows.

Algorithm III; AdaptiveRemeshing

- Let user-specified threshold be the minimum number of points required in each point iteration loop to continue this algorithm.
- 2. Let P0, k = 1, ..., n be the set of points of the background mesh.
- 3. Let P be the set of points and T be the set of triangles.
- 4. Read next interior point p_i of the background mesh from P0.
- 5. If $h_i > h_{max}$ then go to step 4.
- 6. Search triangle t_i in T which contains the point p_i . Then calculate the centroid of the triangle t_i and define it as point p_q , and compute the point distribution function of point p_q .
- 7. Compute the distance d_m , m = 1, 2, 3 from point p_q to each of the three vertices of the triangle t_i .
- 8. Compute the Xi coefficient, χ_i , for point p_i by using Eq. (2), and the average distance, $s_i = (d_1 + d_2 + d_3)/3$.
- 9. Perform the Xi-Alpha test for point p_q . If $(\chi_i * alpha * h_i) \ge s_i$, then reject the point p_q and return to step 4.
- 10. Perform the Xi-Beta test for point p_q . If two out of three of $d_m < (\chi_i * h_{min} / beta)$ for any m = 1, 2, 3, then reject the point p_q and return to step 4.
- 11. Accept the point p_q for insertion by the Delaunay triangulation algorithm and add point p_q into P.
- 12. Repeat steps 4 to 11 until all points in P are considered.
- 13. Perform the Delaunay triangulation of the inserted points in P.

14. If number of inserted points is greater than *threshold*, then go to step 3; otherwise stop the algorithm.

The proposed algorithm above does not guarantee the good mesh topology. The mesh relaxation [20] based on an edge-swapping technique is highly recommended for well-shaped mesh improvement. The objective of this method is to make the topology of elements closer to equilateral triangles by swapping edges to equalize the vertex degrees (number of edges linked to each point) toward the value of six. Finally, the Laplacian smoothing is applied to smooth the meshes. This main algorithm for combining together the mesh generation from the Delaunay triangulation, the mesh refinement procedure, and the adaptive remeshing technique is demonstrated by flow-chart as shown in Fig. 1.

Algorithm evaluation

To evaluate the performance of the adaptive remeshing technique with the Delaunay triangulation, the specification of element size, h_l , is given as an analytical function for two-dimensional domain. The adaptive mesh generation process first generates an initial mesh from the domain, then the values of the element sizes at all points are computed by the given function. The mesh generation coupled with the adaptive remeshing procedure is repeated until the resulting mesh is globally stable. The three examples of adaptive mesh generation with the analytical element size-specification function presented herein are: (1) adaptive meshes along centerline of a rectangular domain, (2) adaptive meshes along a diagonal of a square domain, and (3) alpha-shape adaptive meshes in a square domain.

Adaptive meshes along centerline of a rectangular domain: The first example presents an adaptive mesh generation in a 3×5 rectangular domain. The element sizes at positions in the domain are given by the distribution function,

$$h(x,y) = 0.42 - \frac{1}{\sqrt{2\pi}\sigma} e^{-\left[\frac{y-\mu}{2\sigma}\right]^2}$$
(3)

where y is the variable and the values of μ and σ are constants equal to zero and one, respectively. Figure 2 shows a series of the meshes generated by three successive adaptation of the coarse initial mesh. The value of mesh generation coefficients, α , β , χ_{min} , χ_{max} are 0.5, 0.6, 0.75, and 1.10, respectively. Due to the prescribed distribution function, Eq. (3), small element sizes are specified around the centerline of the domain. The figures show the pattern of graded elements along narrow band around the centerline of the domain. The value of χ_{min} limits number of points insertion along centerline of the domain, while the value of χ_{max} allows more nodes to be inserted into the other regions.

The specification of scale range and limiting χ , χ_{min} and χ_{max} , have strong effects on the resulting meshes as shown in Fig. 2. Without the scale range, the mesh is composed of small elements concentrated around line a (see Fig. 3) with progressively larger elements outwards as $h_a < h_b$, h_c . The scale range function sorts the nodal spacing values into prescribed intervals according to χ_{min} and χ_{max} . In each interval, the generated element sizes are relatively uniform. With them, a mesh consisting of relatively uniform elements in a wider centerline band of the domain is generated. This mesh has better physical correlation with the behaviors of shocks.

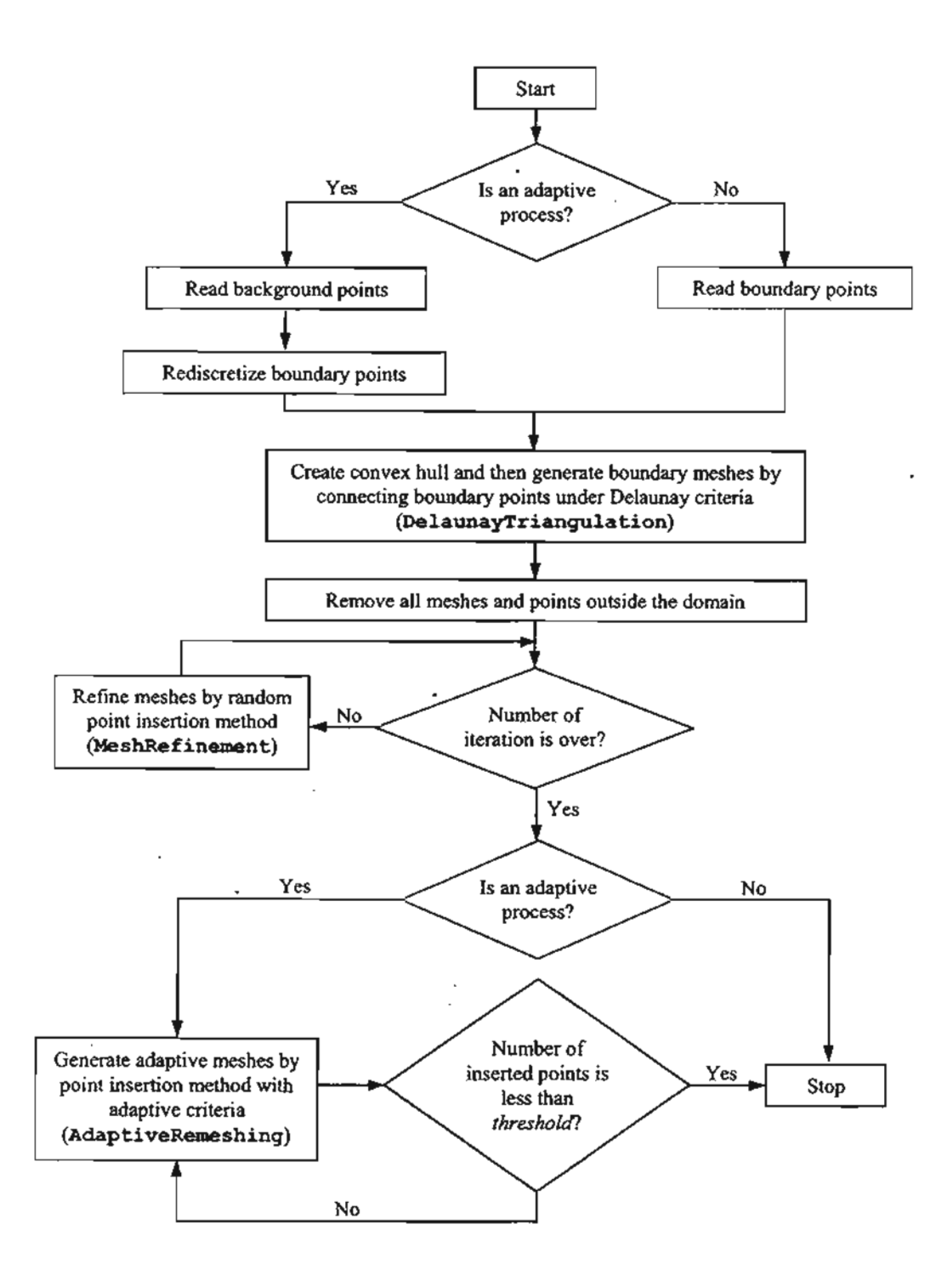


Fig. 1. Flow-chart for a main algorithm of mesh generation and adaptation.

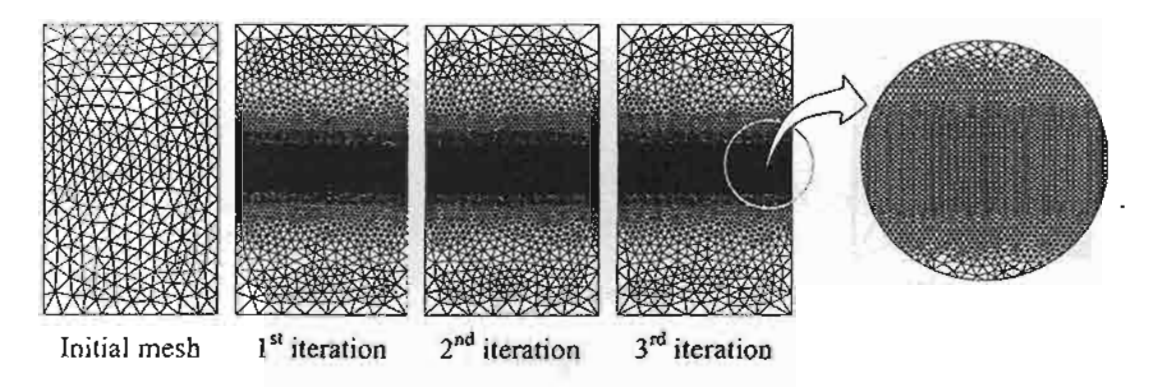


Fig. 2. Adaptive meshes along centerline of a rectangular domain.

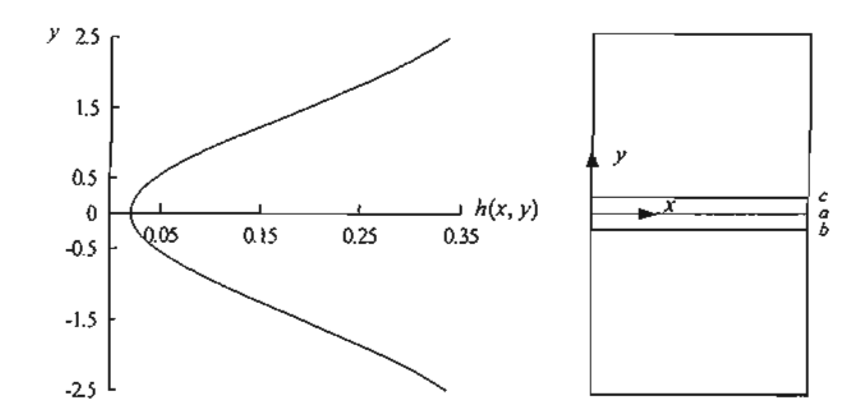


Fig. 3. Distribution of element sizes along the y direction.

Adaptive meshes along a diagonal of a square domain: The second example concerns with an adaptive mesh generation in a unit square domain. The element sizes are calculated by the function in Eq. (4) where the constant α is equal to 0.5 for this test case,

$$h(x,y) = 2y(1-y) \left[\tan^{-1} \beta - \frac{\alpha(1-2x)}{\sqrt{2}(1+\beta^2)} + \frac{\alpha^2 \beta x(1-x)}{2(1+\beta^2)^2} \right] + 2x(1-x) \left[\tan^{-1} \beta - \frac{\alpha(1-2y)}{\sqrt{2}(1+\beta^2)} + \frac{\alpha^2 \beta y(1-y)}{2(1+\beta^2)^2} \right]$$
(4)

where $\beta = \alpha[(x+y)/\sqrt{2}-0.8]$. Because this function generates both negative and positive values, the only positive values of this function are used to determine the element size by scaling into the new range of 0.001 and 0.2. Figure 4 shows the sequence of adaptive meshes generated by five iterations based on a coarse initial mesh. The value of mesh generation coefficients, α , β , χ_{min} , χ_{max} are 0.5, 0.6, 0.4, and 0.75, respectively. The combination of the values of χ_{min} and χ_{max} , narrows the band along the diagonal line with small elements.

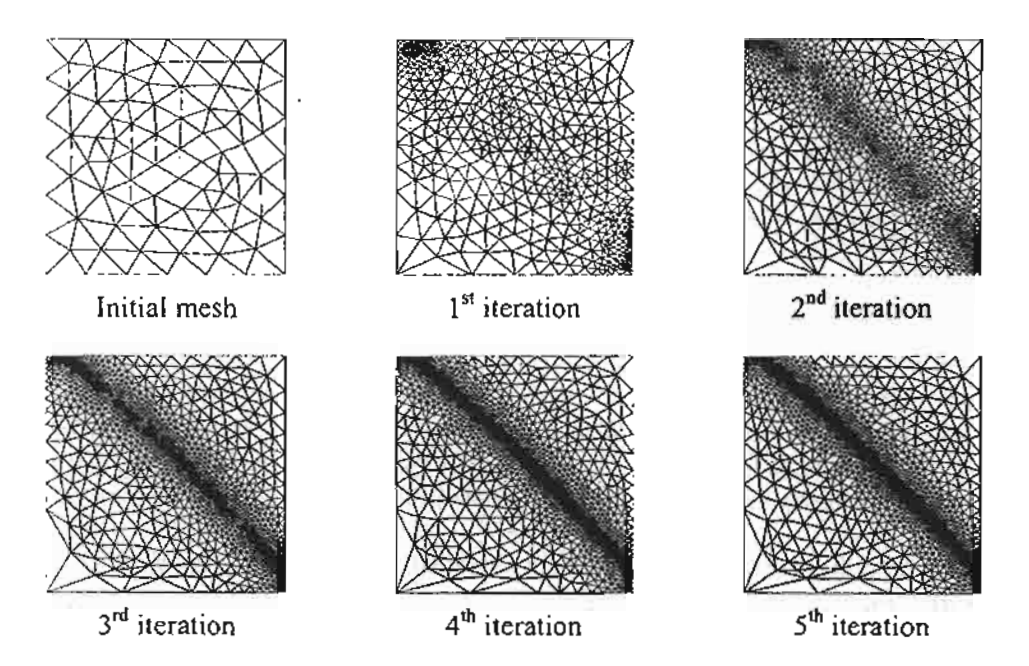


Fig. 4. Adaptive meshes along a diagonal of a square domain.

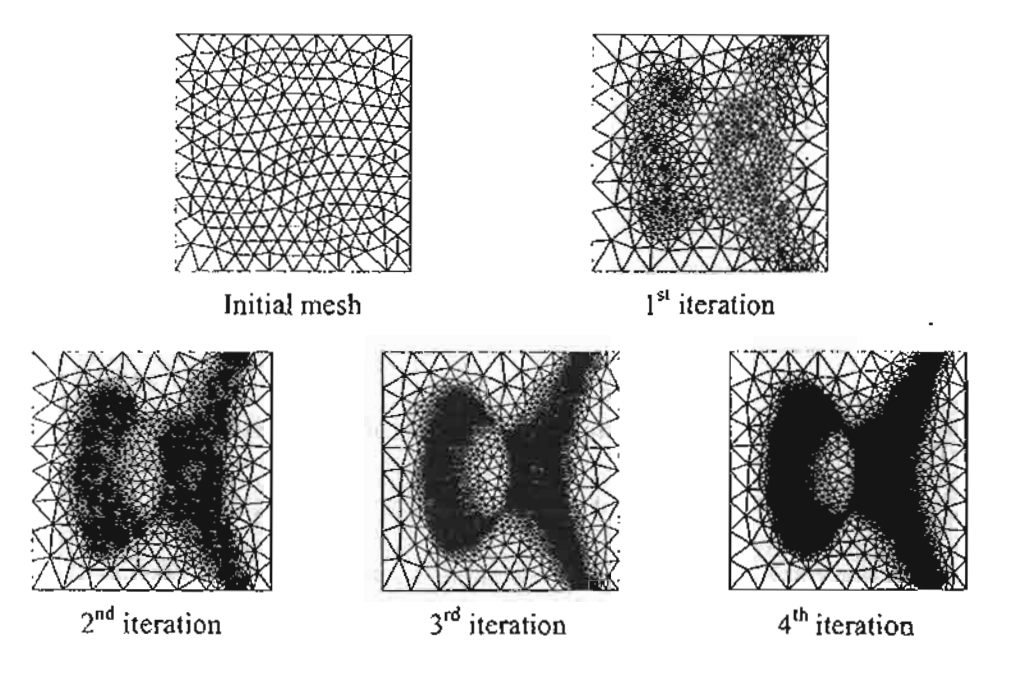


Fig. 5. Alpha-shape adaptive meshes in a square domain.

Alpha-shape adaptive meshes in a square domain: The third example generates an alpha-shape adaptive mesh in a square domain as shown in Fig. 5. The alpha shape function [13] is used to calculate element sizes in an 8×8 square domain,

$$h(x,y) = \begin{cases} \min(0.2(\lambda - 1)^3 + 0.005, 1.0) & \text{if } \lambda \ge 1\\ \min(0.2(\lambda - 1)^2 + 0.01, 1.0) & \text{if } \lambda < 1 \end{cases}$$
 (5)

where the value of parameter λ is determined from $x^3 - y^2 + 2 - 3\lambda x = 0$. The value of mesh generation coefficients, α , β , χ_{min} , χ_{max} are 0.5, 0.6, 0.5, and 0.85, respectively.

HIGH-SPEED COMPRESSIBLE FLOW SOLVER

The performance of the Delaunay triangulation, the automatic point creation procedure, and the adaptive remeshing technique has been evaluated by solving high-speed compressible flow problems. The Roe's flux-difference splitting method is used for compressible flow due to its efficiency with mathematical clarity. This section briefly explains the method and its flexibility in combining with adaptive unstructured meshes to further improve the solution accuracy.

In some certain problems, however, the Roe's scheme may not provide correct solutions for the compressible Euler computation. Unphysical numerical solutions may arise from the implementation of the one-dimensional upwinding numerical flux function onto the multidimensional formulation. To avoid such solutions, a mixed entropy fix method that combines the entropy fix method of Van Leer et al. [18] and the modified multidimensional dissipation method by Pandolfi and D'Ambrosio [19], is proposed in this paper. Details of these entropy fix methods are presented herein and their performance are determined by test cases.

Roe's flux-difference splitting scheme

The governing equations of the two-dimensional Euler equations for inviscid flows are given by,

$$\frac{\partial}{\partial t} \int_{\Omega} U d\Omega + \int_{\partial \Omega} F \cdot \hat{n} dS = 0 \tag{6}$$

where U is the vector of conservation variables, F is the numerical flux vector and \hat{n} is the unit normal vector of the surface boundary. The perfect gas equation of state is in the form,

$$p = \rho e(\gamma - 1) \tag{7}$$

where p is the pressure, p is the density, e is the internal energy, and y is the specific heat ratio. According to the Roe's scheme [14], the numerical flux vector at the cell interface between the left cell L and the right cell R is,

$$F_{n} = \frac{1}{2} (F_{nL} + F_{nR}) - \frac{1}{2} \sum_{k=1}^{4} \alpha_{k} |\lambda_{k}| r_{k}$$
 (8)

where α_k is the wave strength of the k^{th} wave, λ_k is the eigenvalue, and r_k is the corresponding right eigenvector. The eigenvalues in the above Eq. (8) are,

$$\lambda = \begin{bmatrix} V_n - a & V_n & V_n + a \end{bmatrix}^T \tag{9}$$

where V_n is the normal velocity, and a is the speed of sound at the cell interface.

The mixed entropy fix method

Some unphysical solutions such as an expansion shock or the carbuncle phenomenon may be produced from the original Roe's scheme (Roe). To avoid such solutions, the entropy fix methods [17-19,21-23] have been introduced. After extensive investigation, the Van Leer et al.'s entropy fix method [18] has been found to perform very well for flows with unphysical expansion shocks such as flow over a forward facing step. Meanwhile, the Pandolfi and D'Ambrosio's modified multidimensional method of the H-correction entropy fix [19] can efficiently correct the numerical instability when the dissipation added to the entropy and shear waves is very low such as in the flow over the blunt body problem. Thus, this paper proposes a mixed entropy fix method (RoeVLPA) that combines the two above schemes together by replacing the original eigenvalues as follows.

$$\left|\lambda_{1,4}\right| = \begin{cases} \left|\lambda_{1,4}\right| &, \left|\lambda_{1,4}\right| \ge 2\eta^{\nu_L} \\ \frac{\left|\lambda_{1,4}\right|^2}{4\eta^{\nu_L}} + \eta^{\nu_L} &, \left|\lambda_{1,4}\right| < 2\eta^{\nu_L} \end{cases}$$
(10a)

$$\left|\lambda_{2,3}\right| = \max\left(\left|\lambda_{2,3}\right|, \eta^{PA}\right) \tag{10b}$$

where $\eta^{\nu L}$ and $\eta^{\rho A}$ are determined from,

$$\eta^{\nu L} = \max(\lambda_k - \lambda_L, 0) \tag{11}$$

$$\eta^{PA} = \max(\eta_2, \eta_3, \eta_4, \eta_5) \tag{12}$$

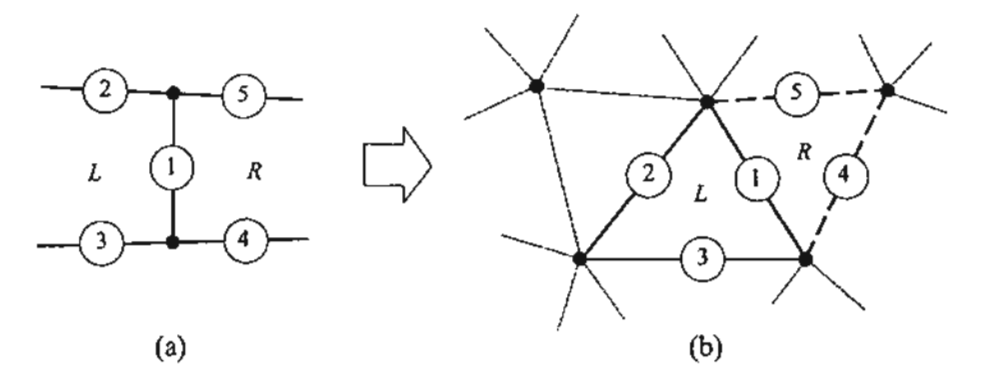


Fig. 6. Cell interfaces of: (a) structured uniform mesh; (b) unstructured triangular mesh.

The values η_i , i = 2 to 5 as shown in Figs. 6(a)-(b) for both the structured and unstructured meshes are determined from,

$$\eta_i = 0.5 \max_{k} (\left| \lambda_{kR} - \lambda_{kL} \right|) \tag{13}$$

where L and R denote the left and right elements, respectively. This mixed entropy fix method is equivalent to the Van Leer *et al.*'s entropy fix method in handling the acoustic waves (k = 1 and 4) and the Pandolfi and D'Ambrosio version of the H-correction entropy fix for the entropy and shear waves (k = 2 and 3). The proposed mixed entropy fix method has been evaluated in this paper using three test cases involving expansion shocks, the carbuncle phenomenon, and the odd-even decoupling on structured triangular meshes.

The expansion shocks: As mentioned earlier, the original Roe's scheme may produce unphysical expansion shocks on some certain problems because it does not satisfy the entropy condition. To illustrate this phenomenon, a Mach 3 flow over a forward facing step [24] is investigated. The density contours computed from the Roe and RoeVLPA are shown in Figs. 7(a)-(b), respectively. The figure shows that the RoeVLPA does not produce an unphysical expansion shock on top of the facing step corner as occurred in the solution from the original Roe's scheme.

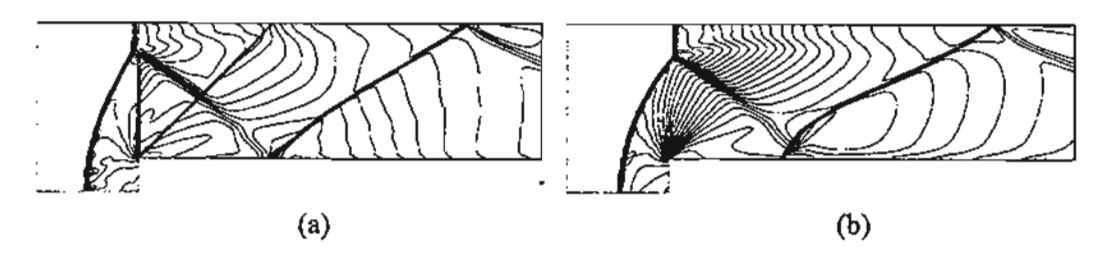


Fig. 7. Mach 3 flow over a forward facing step: (a) Roe; and (b) RoeVLPA.

The Quirk's test (odd-even decoupling): Another test case is a Mach 6 moving shock along odd-even grid perturbation in a straight duct [16]. The computational domain consists of a uniform triangular mesh with 800 and 20 equal intervals respectively along the axial and the transverse directions of the duct. The grids along the duct centerline are perturbed in the transverse direction with magnitude of $\pm 10^{-6}$. It is found that the Roe, as shown in Fig. 8(a), suffers from the numerical instabilities. On the other hand, the RoeVLPA provides accurate shock resolution as shown in Fig. 8(b).

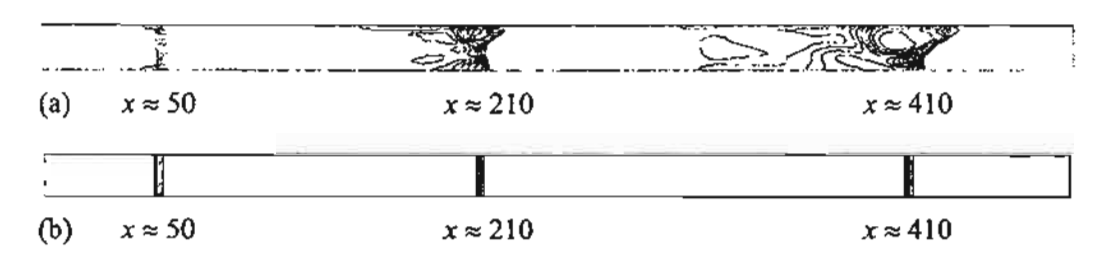


Fig. 8. Mach 6 moving shock along odd-even grid perturbation: (a) Roe; and (b) RoeVLPA.

The carbuncle phenomenon: An unrealistic flow solution, the so called carbuncle phenomenon, of a steady-state flow over a blunt body from the original Roe's scheme was first reported by Perry and Imlay [15]. Such phenomenon refers to a spurious bump on the bow shock near the flow centerline ahead the blunt body. The phenomenon is highly grid-dependent [19], but does not require a large number of grid points to be apparent [25]. Figures 9(a)-(c) show that the carbuncle phenomenon does not appear in RoeVLPA, while the solutions using the original Roe's scheme exhibit the carbuncle phenomenon in the meshes with high element aspect ratio.

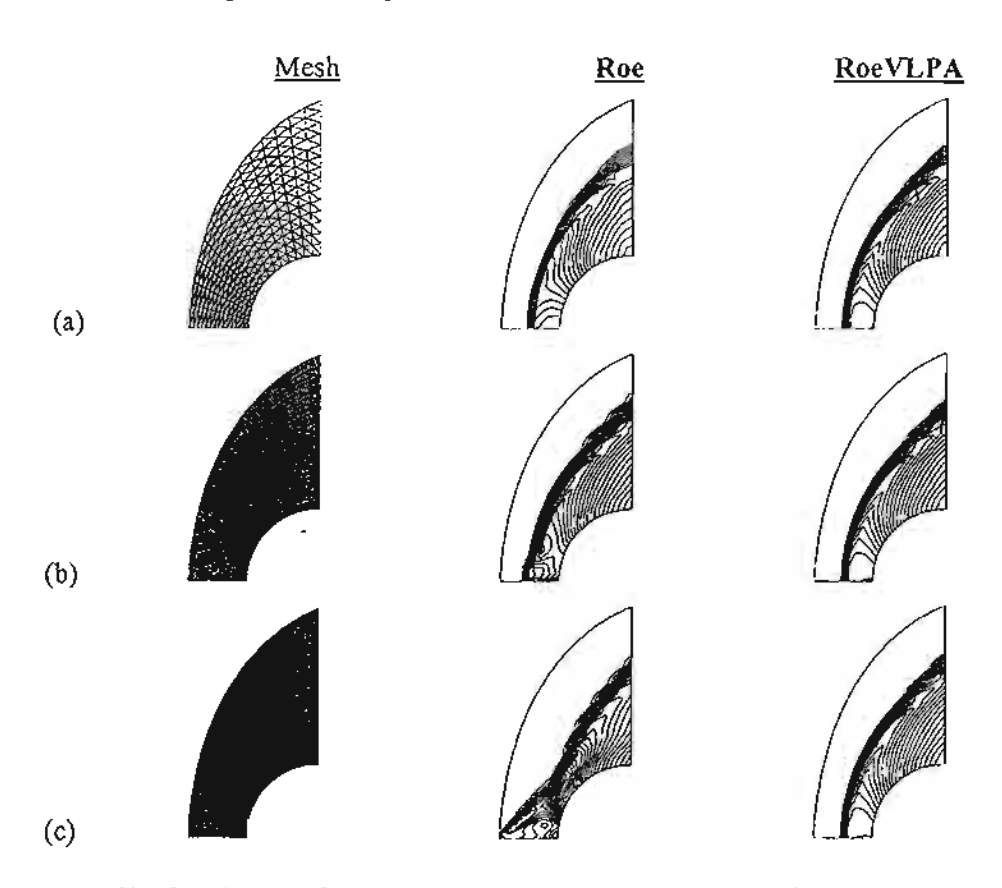


Fig. 9. Mach 15 flow over a blunt body, enlarged view of the mesh and computed density contours: (a) first mesh; (b) second mesh; and (c) third mesh.

HIGHER-ORDER EXTENSION AND APPLICATION ON UNSTRUCTURED TRIANGULAR MESHES

Linear reconstruction and limiter

Solution accuracy from the first-order formulation described in the preceding section can be improved by implementing higher-order approximations for both the space and time. A higher-order spatial discretization is achieved by applying the Taylor' series expansion to the cell-centered solution for each cell face [26]. For instance, the solutions at the midpoint of an element edge between node 1 and 2 shown in Fig. 10, can be reconstructed from,

$$q_{f_{12}} = q_C + \frac{\Psi_C}{3} \left[\frac{(q_1 + q_2)}{2} - q_3 \right]$$
 (14)

where $q = [\rho \ u \ v \ p]^T$ consists of the primitive variables of the density, the velocity components, and the pressure, respectively; q_c is the solution at the element centroid; q_n , n = 1, 2, 3 are the solutions at nodes. In this paper, the pseudo-Laplacian method proposed by Holmes and Connell [27] is used to determine nodal quantities,

$$q_{n} = \sum_{i=1}^{N} (w_{i} q_{C,i}) / \sum_{i=1}^{N} w_{i}$$
 (15)

where q_{CJ} are the surrounding cell-centered values of node n, and N is the number of the surrounding cells. The cell weights w_i are determined from,

$$w_i = 1 + \lambda_x (x_i - x_n) + \lambda_y (y_i - y_n)$$
 (16)

with the Lagrange multipliers, λ_x and λ_y , defined by,

$$\lambda_{x} = \frac{\sum_{i=1}^{N} (x_{i} - x_{n})(y_{i} - y_{n}) \sum_{i=1}^{N} (y_{i} - y_{n}) - \sum_{i=1}^{N} (y_{i} - y_{n})^{2} \sum_{i=1}^{N} (x_{i} - x_{n})}{\sum_{i=1}^{N} (x_{i} - x_{n})^{2} \sum_{i=1}^{N} (y_{i} - y_{n})^{2} - \left[\sum_{i=1}^{N} (x_{i} - x_{n})(y_{i} - y_{n}) \right]^{2}}$$
(17a)

$$\lambda_{y} = \frac{\sum_{i=1}^{N} (x_{i} - x_{n})(y_{i} - y_{n}) \sum_{i=1}^{N} (x_{i} - x_{n}) - \sum_{i=1}^{N} (x_{i} - x_{n})^{2} \sum_{i=1}^{N} (y_{i} - y_{n})}{\sum_{i=1}^{N} (x_{i} - x_{n})^{2} \sum_{i=1}^{N} (y_{i} - y_{n})^{2} - \left[\sum_{i=1}^{N} (x_{i} - x_{n})(y_{i} - y_{n}) \right]^{2}}$$
(17b)

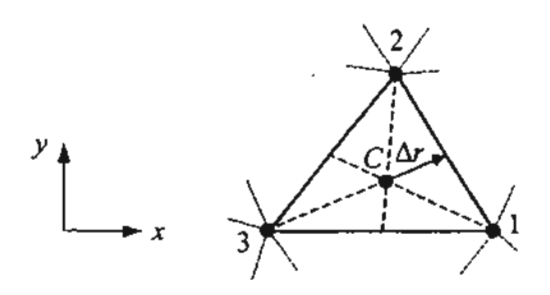


Fig. 10. Linear reconstruction on a typical triangular element.

The cell weights, w_i , may differ significantly from unity for some severe distorted meshes as indicated in Ref. [27], which also suggests weights should be in the range of 0 to 2. In this paper, the weight clipping is slightly different by modifying only the value of weights of boundary meshes. If any weight becomes negative, its absolute value is used for simplicity. Several examples presented below have shown that such modification performs well. The

 Ψ_c in Eq. (14) represents the limiter for preventing spurious oscillation that may occur in the region of high gradients. In this study, Vekatakrishnan's limiter function [28] is selected to improve the convergence.

Second-order temporal discretization

The second-order temporal accuracy is achieved by implementing the second-order accurate Runge-Kutta time stepping method [29],

$$U_{i}^{*} = U_{i}^{n} - \frac{\Delta t}{\Omega_{i}} \sum_{j=1}^{3} F^{n} \cdot n_{j}$$

$$U_{i}^{n+1} = \frac{1}{2} \left[U_{i}^{n} + U_{i}^{*} - \frac{\Delta t}{\Omega_{i}} \sum_{j=1}^{3} F^{*} \cdot n_{j} \right]$$
(18)

where Δt is the time step. To reduce computational effort, the local element time steps are used for steady-state analysis, while the minimum global time step based on spectral radii [30] is used for the transient analysis.

Numerical evaluation

The increase in order of accuracy of the Roe's scheme with the proposed entropy fix method, described in the preceding section, is evaluated by solving several test cases on both structured and adaptive unstructured triangular meshes. The selected test cases are: (1) Symmetric rarefaction wave, (2) Oblique shock reflection at a wall, and (3) Mach 1.4 flow past a 4% bump.

Symmetric rarefaction wave: The initial conditions of the fluids on the left and right sides of the tube are given by $(\rho, u, p)_L = (7.0, -1.0, 0.2)$ and $(\rho, u, p)_R = (7.0, 1.0, 0.2)$. Such initial conditions [30] are chosen to produce vacuum at x = 0. The 1.0×0.1 computational domain is, respectively, divided into 400 and 40 equal intervals in the x and y directions by triangular elements. Figures 11(a)-(c) show the computed density, pressure and u-velocity distributions along the tube length as compared to the solution from the HLLC method [31] and the exact solution at time t = 0.3. The HLLC method is chosen because of its capability for capturing shocks, contact discontinuities and rarefactions. The solutions obtained from RoeVLPA and HLLC methods compare well with the exact solution as highlighted on the upper right portion of Fig. 11.

Oblique shock reflection at a wall: The problem statement of an oblique shock reflection at a wall [32] on the 4.0×1.0 domain is presented in Fig. 12. The analysis process starts by creating a relatively uniform mesh as shown in Fig. 13(a). The fluid analysis is then performed to generate the corresponding solution such as the density contours as shown in Fig. 13(b). This flow solution is then used to generate an adaptive mesh. The entire process is repeated to generate the third adaptive mesh and its corresponding solutions as shown in Figs. 13(c)-(d). Figures 14(a)-(b) show comparative density and pressure distributions between the exact and computed solutions at y = 0.5.

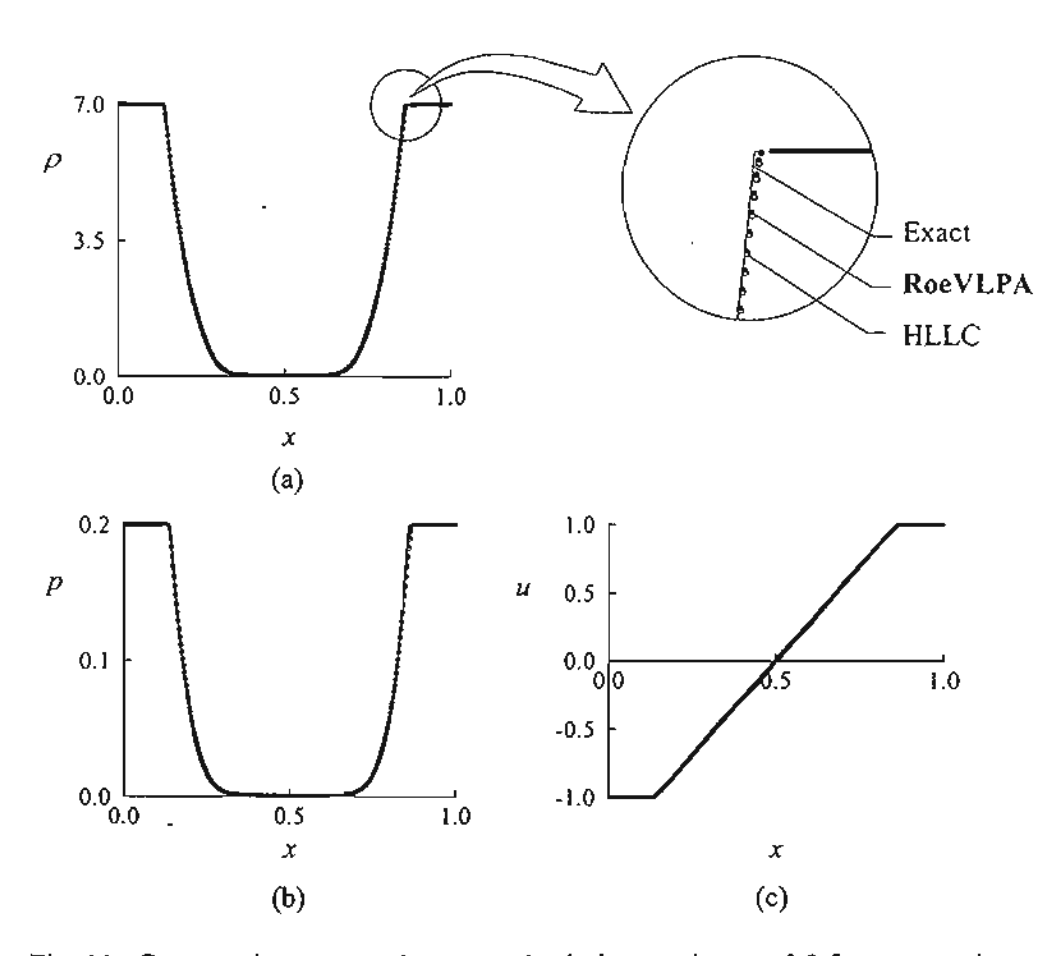


Fig. 11. Comparative exact and computed solutions at time t = 0.3 for symmetric rarefaction wave problem: (a) density distributions; (b) pressure distributions; and (c) u-velocity distributions.

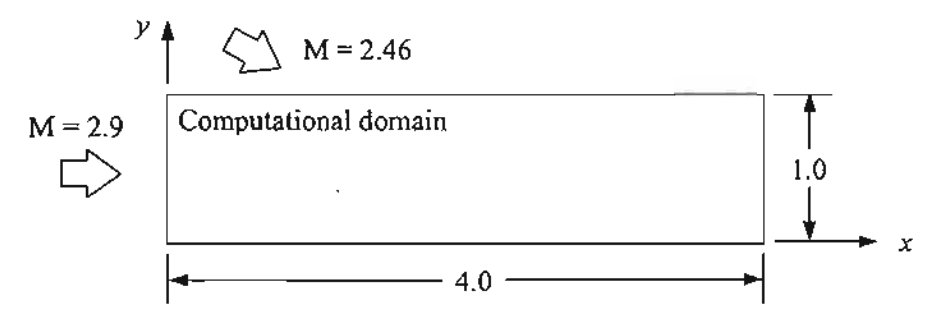
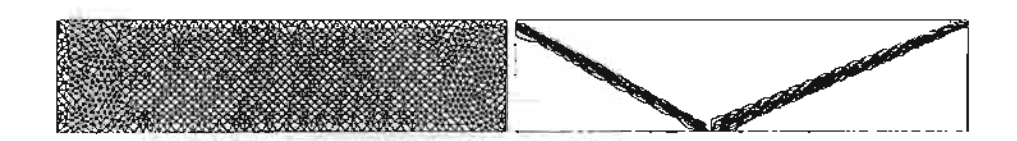


Fig. 12. Problem statement of an oblique shock reflection at a wall.



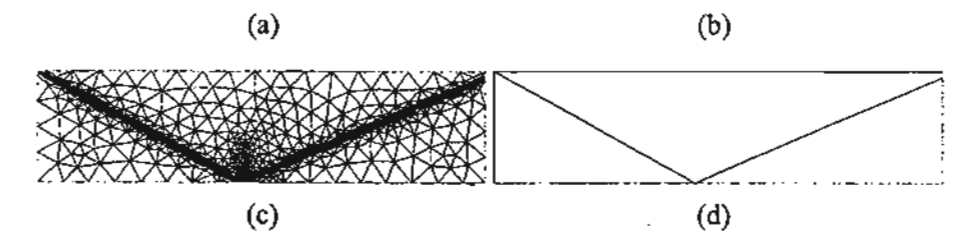


Fig. 13. An oblique shock reflection at a wall: (a)-(b) Initial mesh and the corresponding density contours; and (c)-(d) Third adaptive mesh and the corresponding density contours.

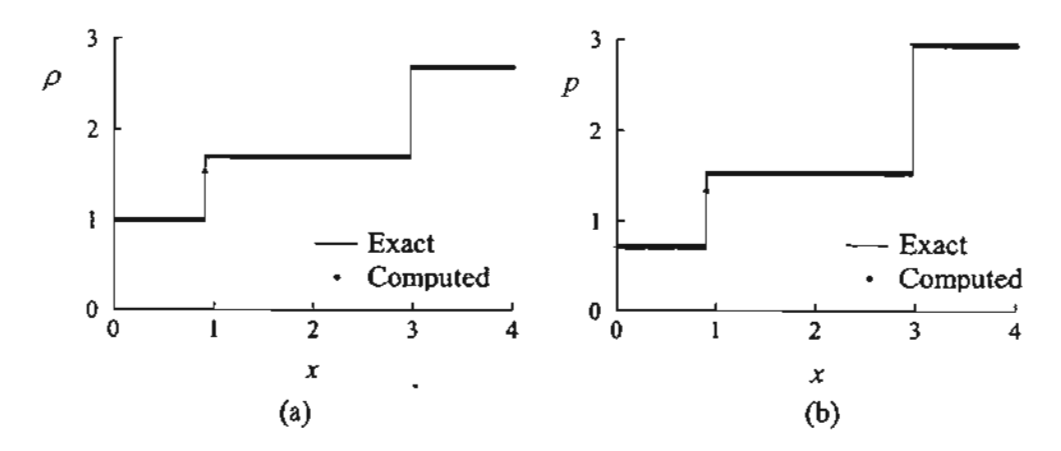


Fig. 14. Comparative solutions of an oblique shock reflection at a wall:

(a) density distribution; and (b) pressure distribution.

Mach 1.4 flow past a 4% bump: The problem statement of a Mach 1.4 flow past a 4% bump is presented in Fig. 15. Figures 16(a)-(b) show a structured mesh and its corresponding computed pressure contours by the higher-order scheme. The fourth adaptive mesh and its corresponding computed pressure contours by the higher-order scheme are shown in Figs. 17(a)-(b). The results highlight the capability of the combined method to capture lambda shock structure [33] and detailed flow phenomena with sharp shocks and their reflections. Figure 18 shows the density distributions along upper wall obtained from the higher-order RoeVLPA on both the structured and the adaptive meshes, as compared to the solution of Ref. [34].

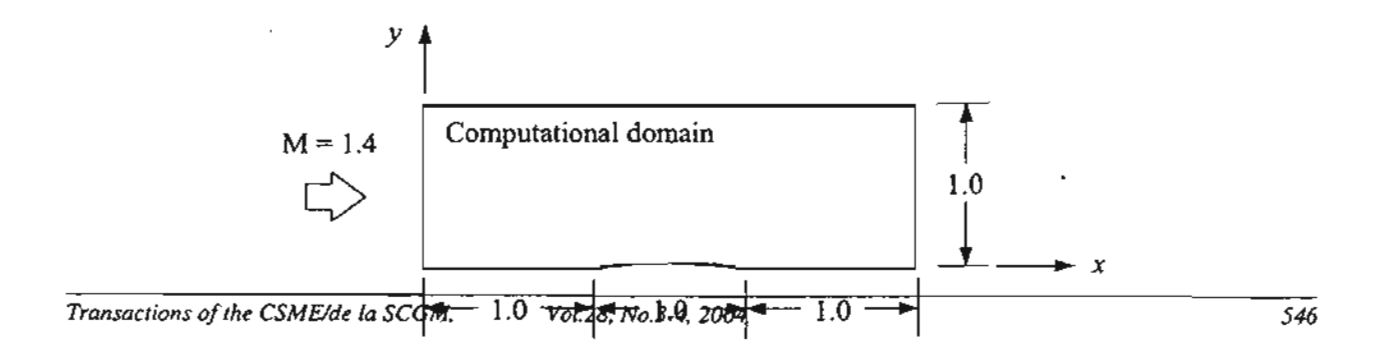


Fig. 15. Problem statement of a Mach 1.4 flow past a 4% bump.

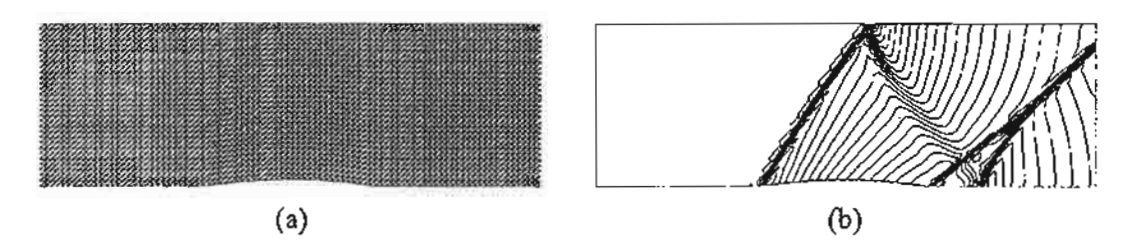


Fig. 16. Mach 1.4 flow past a 4% bump: (a) Structured mesh; and (b) Pressure contours.

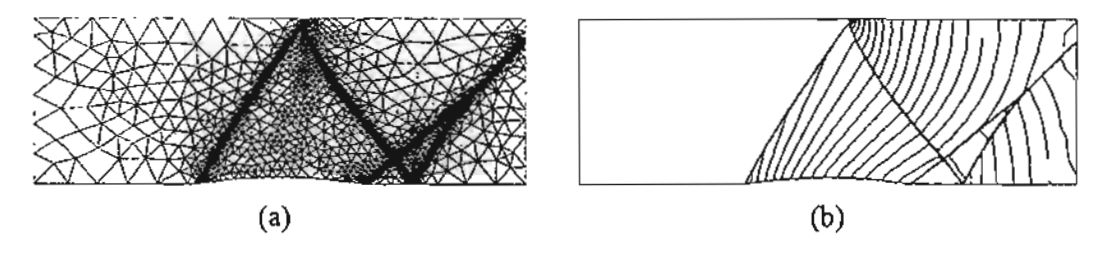


Fig. 17. Mach 1.4 flow past a 4% bump: (a) Fourth adaptive mesh; and (b) Pressure contours.

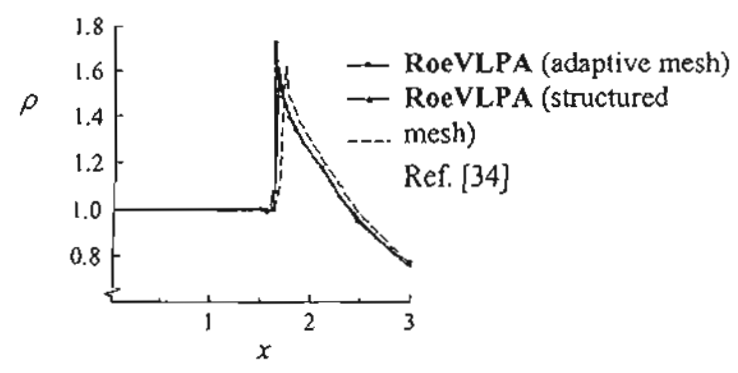


Fig. 18. Comparative density solutions of a Mach 1.4 flow past a 4% bump along the upper wall.

CONCLUSION

A mixed entropy fix method for Roe's flux-difference splitting scheme for the analyzes of two-dimensional high-speed compressible flow with mesh adaptation was presented. The mesh adaptation algorithm was evaluated by discretizing domains of three examples with prescribed element size functions. To capture steep variations of the solution effectively, a new element size scaling function was introduced into the adaptive meshing technique. A mixed entropy fix method was proposed to improve numerical stability of the Roe's flux-difference splitting scheme for solving high-speed compressible flow problems. The method combines the entropy fixes by Van Leer et al. [18] together with Pandolfi and D'Ambrosio [19]. The method was evaluated by several well-known test cases and found to eliminate unphysical solutions that may arise from the use of the original Roe's scheme. The method was then combined with the adaptive mesh generation technique to demonstrate the simulation applicability on arbitrary unstructured meshes for high-speed compressible flow problems.

ACKNOWLEDGEMENT

The authors are pleased to acknowledge the Thailand Research Fund (TRF) for supporting this research work.

REFERENCES

- 1 Bowyer, A., Computing Dirichlet Tessellations, Comp. J., 24, 1981, pp. 162-166.
- Watson, D.F., Computing the n-Dimensional Delaunay Tessellation with Application to Voronoi Polytopes, Comp. J., 24, 1981, pp. 167-172.
- 3 Jin, H. and Wiberg, N.E., Two-Dimensional Mesh Generation, Adaptive Remeshing and Refinement, Int. J. Numer. Methods in Eng., 1990, 29, pp.1501-1526.
- 4 Rebay, S., Efficient Unstructured Mesh Generation by Means of Delaunay Triangulation and Bowyer-Watson Algorithm, J. Comput. Phys., 1993, 106, pp. 125-138.
- 5 Marchant, M.J. and Weatherill, N.P., Adaptivity Techniques for Compressible Inviscid Flows, Comput. Methods Appl. Mech. Eng., 106, 1993, pp. 83-106.
- 6 Karamete, B.K., Tokdemir, T. and Ger, M., Unstructured Grid Generation and a Simple Triangulation Algorithm for Arbitrary 2-D Geometries using Object Oriented Programming, Int. J. Numer. Methods in Eng., 40, 1997, pp. 251-268.
- 7 Phongthanapanich, S. and Dechaumphai, P., Evaluation of Combined Delaunay Triangulation and Remeshing for Finite Element Analysis of Conductive Heat Transfer, Trans. of the CSME, 27, 2004.
- 8 Peraire, J., Vahdati, M., Morgan, K. and Zienkiewicz, O.C., Adaptive Remeshing for Compressible Flow Computations, J. Comput. Phys., 72, 1987, pp. 449-466.
- 9 Probert, J., Hassan, O., Peraire, J. and Morgan, K., An Adaptive Finite Element Method for Transient Compressible Flows, Int. J. Numer. Methods in Eng., 32, 1991, pp. 1145-1159.
- 10 Marcum, D.L., Weatherill, N.P., Marchant, M.J. and Beaven F., Adaptive Unstructured Grid Generation for Viscous Flow Applications, AIAA Paper 95-1726CP, 12th AIAA Computational Fluid Dynamics Conference, San Diego, CA, 1995.
- 11 Borouchaki, H., Castro-Diaz, M.J., George, P.L., Hecht, F. and Mohammadi, B., Anisotropic Adaptive Mesh Generation in Two Dimensions for CFD, 5th International

- Conference On Numerical Grid Generation in Computational Field Simulations, Mississppi State University, 1996, pp.197-206.
- 12 Borouchaki, H., George, P.L. and Mohammadi, B., Delaunay Mesh Generation Governed by Metric Specifications. Part I. Algorithms. Finite Elem. Anal. Des., 25, 1997, pp. 61-83.
- 13 Borouchaki, H., George, P.L. and Mohammadi, B., Delaunay Mesh Generation Governed by Metric Specifications. Part II. Application, *Finite Elem. Anal. Des.*, 25, 1997, pp. 85-109.
- 14 Roe, P.L., Approximate Riemann Solvers, Parameter Vectors, and Difference Schemes, J. Comp. Phys., 43, 1981, pp. 357-372.
- 15 Perry, K.M. and Imlay, S.T., Blunt-body Flow Simulations, *AIAA Paper-88-2904*, 24th AIAA, SAE, ASME and ASEE Joint Propulsion Conference, Boston, MA, 1988.
- 16 Quirk, J.J., A Contribution to the Great Riemann Solver Debate, Int. J. Numer. Meth. Fluids, 18, 1994, pp. 555-574.
- 17 Harten, A., High Resolution Schemes for Hyperbolic Conservation Laws, J. Comp. Phys., 49, 1983, pp. 357-393.
- 18 Van Leer, B., Lee, W.T. and Powell, K.G., Sonic-Point Capturing, AIAA Paper-89-1945-CP, 9th Computational Fluid Dynamics Conference, Buffalo, New York, 1989.
- 19 Pandolfi, M. and D'Ambrosio, D., Numerical Instabilities in Upwind Methods: Analysis and Cures for the "Carbuncle" Phenomenon, J. Comp. Phys., 166, 2001, pp. 271-301.
- 20 Frey, W.H., Mesh Relaxation: A New Technique for Improving Triangulations, Int. J. Numer. Methods in Eng., 31, 1991, pp. 1121-1133.
- 21 Lin, H.C., Dissipation Additions to Flux-Difference Splitting, J. Comp. Phys., 117, 1995, pp. 20-27.
- 22 Sanders, R., Morano, E., Druguet, M.C., Multidimensional Dissipation for Upwind Schemes: Stability and Applications to Gas Dynamics, J. Comp. Phys., 145, 1998, pp. 511-537.
- 23 Dechaumphai, P. and Phongthanapanich, S., High-Speed Compressible Flow Solutions by Adaptive Cell-Centered Upwinding Algorithm with Modified H-Correction Entropy Fix, Adv. Eng. Software, 34, 2003, pp. 533-538.
- 24 Woodward, P. and Colella, P., The Numerical Simulation of Two-Dimensional Fluid Flow with Strong Shocks, J. Comp. Phys., 54, 1984, pp. 115-173.
- 25 Gressier, J. and Moschetta, J.M., Robustness versus Accuracy in Shock-Wave Computations, Int. J. Numer. Meth. Fluids, 33, 2000, pp. 313-332.
- 26 Frink, N.T., Recent Progress toward a Three-Dimensional Unstructured Navier-Stokes Flow Solver, AIAA Paper-94-0061, 32th Aerospace Sciences Meeting, Reno, Nevada, 1994.
- 27 Holmes, D.G. and Connell, S.D., Solution of the 2D Navier-Stokes Equations on Unstructured Adaptive Grids, AIAA Paper-89-1932-CP, 9th Computational Fluid Dynamics Conference, Buffalo, New York, 1989.
- 28 Vekatakrishnan, V., Convergence to Steady State Solutions of the Euler Equations on Unstructured Grids with Limiters, J. Comp. Phys., 118, 1995, pp. 120-130.
- 29 Shu, C.W. and Osher, S., Efficient Implementation of Essentially Non-Oscillatory Shock-Capturing Schemes, J. Comp. Phys., 77, 1988, pp. 439-471.
- 30 Linde, T. and Roe, P.L., Robust Euler Codes. AIAA Paper-97-2098, 13th Computational Fluid Dynamics Conference, Snowmass Village, CO, 1997.
- 31 Toro E.F., Spruce, M. and Speares, W., Restoration of the Contact Surface in the HLL-Riemann Solver, ShockWaves, 4, 1994, pp. 25-34.

บทความทางวิชาการ เรื่อง

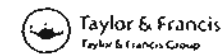
Evaluation of the Damping Functions in Low-Reynolds-Number Non-Linear q-zeta Turbulence Model

Published in the

International Journal of Computational Fluid Dynamics

Vol. 19, No. 3, pp. 225-234

2005



Evaluation of the damping functions in low-Reynolds-number non-linear $q - \zeta$ turbulence model

V. JUNTASARO†*, P. DECHAUMPHAI‡ and A.J. MARQUIS¶§

†Computational Mechanics Laboratory (CML), Department of Mechanical Engineering, Faculty of Engineering, Kasetsan University, Bangkhen, Bangkok 10900, Thailand †Department of Mechanical Engineering, Chulalongkom University, Bangkok, Thailand †Department of Mechanical Engineering, Imperial College of Science, Technology and Medicines, London, UK

(Received 6 May 2004)

The present work concerns the evaluation of the damping functions in the low-Reynolds-number non-linear $q = \zeta$ turbulence model to improve the accuracy of the predicted results. Different expressions for the damping function (f_{μ}) are studied to find the most suitable use in low-Reynolds-number turbulence models, followed by the re-optimisation of the constants in the expression of C_{μ} for the non-linear $q = \zeta$ model. The non-linear form is considered as a result of the inability of the model in linear form to predict the correct anisotropy near solid boundaries. The fully developed turbulent incompressible channel flow is used as a test case. The modified model is evaluated for complex flows via the numerical modelling of the turbulent compressible flow in an S-shaped DRA M2129 circular-to-circular diffusing duct at subsonic Mach number. The predicted results are in good agreement with the experimental data.

Keywords: Damping functions; Non-linear $q - \zeta$ turbulence model; Complex flows; S-shaped diffusing duct

I. Introduction

The errors in predicted solutions using computational fluid dynamics are due to two main sources, numerical and physical. The present work concerns the physical errors resulting from the modelling of the Reynolds-stress term, the additional term arising from averaging in the instantaneous conservation equations for turbulent flows. Two broadly speaking approaches are usually adopted. In the first, the near-wall region is bridged by wall functions based on the Law of the Wall and is economical in terms of computer time and storage, however, it can only be used where the flow is attached since the friction velocity $U_r =$ $\sqrt{\tau_{\rm tr}/\rho}$ is undefined in separation regions. In the second approach, the transport equations are solved down to the wall and damping functions are introduced to account for the turbulence damping effects near the wall. This second approach is called low-Reynolds-number turbulence modelling and is the approach adopted in this work.

The $q - \zeta$ model has been proposed by Gibson and Dafa' Alla (1994), where the two dependent variables are $q(=\sqrt{k})$ and $\zeta(=\varepsilon/2q)$. The square root of the turbulence kinetic energy q is preferred to k because in the region

very close to the wall, q varies linearly with distance y and similarly the destruction rate of q, ζ is better behaved than the energy dissipation rates ε or $\bar{\varepsilon}$, of the $k-\varepsilon$ model; thus, the equations for q and ζ may be solved on a relatively coarse calculation mesh. Furthermore, both q and ζ are zero at the wall and numerical problems are alleviated because there is no need to calculate terms like $D=2\nu(\partial\sqrt{k}/\partial y^2)$ which are needed to provide a derived boundary condition for ε in the $k-\varepsilon$ model.

The linear $q = \zeta$ model is based on the linear stress-strain relationship of Boussinesq (1877), which cannot be predicted accurately near wall turbulent flows, especially in the presence of strong adverse pressure gradients, and those with separation and re-attachment.

Lien et al. (1996) proposed the non-linear low-Reynolds-number $k - \varepsilon$ model, by adopting ideas proposed by Pope (1975) and Shih et al. (1993) in respect of sensitising the eddy-viscosity directly to strain and vorticity invariants. The approach is simple, easy to implement and performs well in both transitional and fully turbulent flows. It is important to note that the desirable reduction of shear stress in impingement and separated zones relative to that returned by the linear form is mainly

^{*}Corresponding author E-mail: ovrsk@ku.ac.th

[§] E-mail: a.marquis@ic.ac.uk

226 V. Juntasaro et al.

due to the functional dependence of $C_{\mu}(S, \Omega)$, where S and Ω are the strain rate and the vorticity rate, respectively, and the anisotropic behaviour of the turbulent stresses only makes a marginal contribution to it.

Ong (1997) adopted the approach of Lien et al. (1996) and has proposed a non-linear $q - \zeta$ turbulence model. Ong applied the non-linear $q - \zeta$ model to fully-developed turbulent channel flow and produced the correct rising trend of the rate of dissipation ε^+ in the near-wall region, however, the distributions of U^+ and shear stress uv^+ are not well predicted in the logarithmic region. This may have been due to the use of non-optimised constants in the C_{μ} formulation or an inappropriate damping function (f_{μ}) , each of which may need to be re-optimised.

According to Patel et al. (1985), the proposed formulation for f_{μ} should agree with that deduced from experimental or DNS data. Patel et al. compared the behaviour of f_{μ} from different low-Reynolds-number models with that deduced from experimental data, and Rodi and Mansour (1995) repeated the comparison with DNS data and proposed a new expression for f_{μ} . The fully developed channel flow results at Re_{τ} = 180 and 395 were improved by the use of this f_{μ} .

The present work aims to find the most suitable expression of damping function and the optimised constants for non-linear $q - \zeta$ model, to improve the accuracy of the predicted results, using the fully developed turbulent channel flow as a test case. The performance of the modified model is then evaluated with the view of its capability in predicting three-dimensional complex flows where effects of streamline curvature and flow separations are important. The model is applied to the flow within the DRA M2129 circular-to-circular intake configuration at subsonic Mach number.

2. Mathematical formulation

2.1 Governing equations

The instantaneous mass, momentum and energy conservation equations are written in Cartesian tensor form as:

$$\frac{\partial \rho}{\partial t} + \frac{\partial \rho u_i}{\partial x_i} = 0 \tag{1}$$

$$\frac{\partial \rho u_i}{\partial t} + \frac{\partial \rho u_i u_j}{\partial x_j} = -\frac{\partial p}{\partial x_i} + \frac{\partial t_{ij}}{\partial x_j}$$
 (2)

$$\frac{\partial}{\partial t} \left\{ \rho \left(e + \frac{1}{2} u_i u_i \right) \right\} + \frac{\partial}{\partial x_j} \left\{ \rho u_j \left(e + \frac{1}{2} u_i u_i + \frac{p}{\rho} \right) \right\} \\
= \frac{\partial u_i t_{ij}}{\partial x_i} - \frac{\partial q_j}{\partial x_j} \tag{3}$$

where e is the specific internal energy, t_{ij} is the viscous stress tensor, and q_j is the heat flux vector. The pressure, density and temperature are related by an equation of

state, which for a perfect gas is,

$$p = \rho RT \tag{4}$$

where R is the gas constant. The heat flux vector $\{q_j\}$ is usually obtained from Fourier's law, i.e.

$$q_j = -k_{\rm T} \frac{\partial T}{\partial x_i} \tag{5}$$

where k_T is the thermal conductivity. The viscous stress tensor (t_{ij}) for a Newtonian fluid is expressed as

$$t_{ij} = \mu \left[\left(\frac{\partial u_i}{\partial x_i} + \frac{\partial u_j}{\partial x_i} \right) - \frac{2}{3} \delta_{ij} \frac{\partial u_k}{\partial x_k} \right]. \tag{6}$$

The energy equation (3) can also be written in terms of total energy $E = e + (1/2)u_iu_i$ and total enthalpy $H = h + (1/2)u_iu_i$ as

$$\frac{\partial \rho E}{\partial t} + \frac{\partial \rho u_j H}{\partial x_j} = \frac{\partial u_i t_{ij}}{\partial x_i} - \frac{\partial q_j}{\partial x_j}.$$
 (7)

If the fluid is assumed to be calorically perfect, i.e. the specific heat coefficients C_p and C_v are constant, then the specific internal energy $e = C_v T$ and the specific enthalpy $h = C_p T$.

The differential conservation equations for mass, momentum and energy presented in the previous section are written in the instantaneous form, and they are only valid on an instantaneous basis in turbulent flows, therefore, it is necessary to convert these instantaneous equations to the time averaged form. Two time-averaging procedures are commonly used for the instantaneous equations, the conventional unweighted time averaging (Reynolds averaging) and the density-weighted time averaging (Favre averaging). The Favre averaging is helpful to simplify the formulation of the turbulent equations when density varies and it is used in this work.

The Favre-averaged mean equations of motion for steady compressible flows can then be written as:

$$\frac{\partial \bar{\rho} \tilde{u}_i}{\partial r_i} = 0 \tag{8}$$

$$\frac{\partial \bar{\rho} u_i u_j}{\partial x_j} = -\frac{\partial \bar{p}}{\partial x_i} + \frac{\partial}{\partial x_j} (\bar{t}_{ij} + \tau_{ij}) \tag{9}$$

$$\frac{\partial \bar{\rho} \bar{u}_{j} \bar{E}}{\partial x_{j}} = \frac{\partial}{\partial x_{j}} (\bar{u}_{i} (\bar{t}_{ij} + \tau_{ij}))
+ \frac{\partial}{\partial x_{j}} \left(\overline{t_{ij} u_{i}^{"}} - \overline{p' u_{j}^{"}} - \frac{1}{2} \bar{\rho} u_{i}^{"} u_{i}^{"} u_{j}^{"} \right)
- \frac{\partial}{\partial x_{j}} (\bar{q}_{j} + \bar{\rho} u_{j}^{"} h^{"}) - \frac{\partial \bar{u}_{j} \bar{p}}{\partial x_{j}}$$
(10)

$$\bar{p} = \bar{\rho}R\bar{T} = (\gamma - 1)\bar{\rho}(\hat{E} - K - k) \tag{11}$$

with the mean viscous stress tensor as:

$$\bar{\iota}_{ij} = \mu \left[\left(\frac{\partial \bar{u}_i}{\partial x_j} + \frac{\partial \tilde{u}_j}{\partial x_i} \right) - \frac{2}{3} \delta_{ij} \frac{\partial \tilde{u}_k}{\partial x_k} \right]$$
 (12)

The Favre-averaged mean conservation equation for mass (8) has the same form as its instantaneous equation (1), the mean momentum equation (9) is different from the instantaneous equation (2) only by the presence of the Favre-averaged Reynolds-stress tensor τ_{ij} , while the Favre-averaged mean energy equation (10) has four extra terms, in addition to the Reynolds-stress tensor term τ_{ij} , that require modelling, i.e. the turbulent heat flux $\bar{\rho}u_j^{\ \mu}h^{\mu}$, the molecular diffusion $\bar{t}_{ij}u_i^{\ \mu}$, the turbulent transport $(1/2)\bar{\rho}u_i^{\ \mu}u_j^{\ \mu}$, and the pressure diffusion $\bar{p}'u_j^{\ \mu}$, and are modelled as in Wilcox (1993).

2.2 Turbulence models

2.2.1 Low-Reynolds-number linear $k - \varepsilon$ turbulence model. Following the Boussinesq (1877) approximation, the Favre-averaged Reynolds-stress tensor τ_{tt} is written as

$$\tau_{ij} = -\frac{1}{\rho u_i^{\prime\prime} u_j^{\prime\prime}}$$

$$= -\frac{2}{3} \delta_{ij} \left(\bar{\rho} k + \mu_i \frac{\partial \bar{u}_k}{\partial x_k} \right) + \mu_i \left(\frac{\partial \bar{u}_i}{\partial x_j} + \frac{\partial \bar{u}_j}{\partial x_i} \right)$$
(13)

where the eddy viscosity μ_i is defined in terms of k and ε as

$$\mu_i = \bar{\rho} C_\mu f_\mu \frac{k^2}{\varepsilon} \tag{14}$$

For a numerically convenient boundary condition at the wall, ε is written as $\varepsilon = \varepsilon + D$ where D is chosen such that $\varepsilon = 0$ at the wall. Thus, the steady flow transport equations for k and ε are written as:

$$\frac{\partial \tilde{\rho} \, \tilde{u}_{j} k}{\partial x_{j}} = \frac{\partial}{\partial x_{j}} \left(\overline{t_{ij} u_{i}''} - \overline{p' u_{j}''} - \frac{1}{2} \, \tilde{\rho} u_{i}'' u_{i}'' u_{j}'' \right)$$

$$+ \tau_{ij} \frac{\partial \tilde{u}_{i}}{\partial x_{j}} - \tilde{\rho} (\tilde{\epsilon} + D) - \overline{u_{i}''} \frac{\partial \tilde{\rho}}{\partial x_{i}}$$

$$production production pressure work$$

$$+ \overline{p' \frac{\partial u_{i}''}{\partial x_{j}}}$$

$$pressure dilatation (15)$$

$$\frac{\partial \bar{\rho} \, \bar{u}_{j} \bar{\varepsilon}}{\partial x_{j}} = \frac{\partial}{\partial x_{j}} \left(\mu \frac{\partial \bar{\varepsilon}}{\partial x_{j}} \right) + \frac{\partial \bar{\rho} \bar{D}'_{\varepsilon j}}{\partial x_{j}} + (\bar{G}_{\varepsilon})_{\text{production}}
- (\bar{\rho} \bar{D}_{\varepsilon}) - \frac{4}{3} \bar{\rho} \bar{\varepsilon} \frac{\partial \bar{u}_{k}}{\partial x_{k}} + \bar{\rho} \bar{\varepsilon} \tag{16}$$

where

$$\begin{split} \tilde{G}_{\varepsilon} &= \tilde{\rho} \tilde{P} = f_{\varepsilon 1} C_{\varepsilon 1} \frac{\varepsilon}{k} \tau_{ij} \left(\frac{\partial \tilde{u}_{i}}{\partial x_{j}} + \frac{1}{3} \frac{\partial \tilde{u}_{k}}{\partial x_{k}} \delta_{ij} \right) \\ \tilde{D}_{\varepsilon} &= f_{\varepsilon 2} C_{\varepsilon 2} \frac{\varepsilon^{2}}{k} \\ \tilde{\rho} \tilde{D}_{\varepsilon j}^{t} &= \frac{\mu_{t}}{\sigma_{\varepsilon}} \frac{\partial \varepsilon}{\partial x_{j}} \end{split}$$

The damping functions f_{e1} , f_{e2} , f_{μ} , and the closure constants C_{e1} , C_{e2} and σ_e vary between different versions of low-Reynolds-number $k-\varepsilon$ model. The version used in this work is that proposed by Launder and Sharma (1974), because its damping function (f_{μ}) is expressed in terms of turbulent Reynolds number $\text{Re}_t = k^2/\nu\varepsilon$ and is preferred to those which comprises f_{μ} in terms of distance from the wall, $y^+(=yU_{\tau}/\nu)$. Formulations in terms of y^+ are unfavourable mainly because U_{τ} is meaningless at a stagnation point and because the calculation of y^+ in a corner of the flow domain is ambiguous.

In spite of its simplicity and popularity, the low-Reynolds-number $k - \varepsilon$ model does have some disadvantages. In wall-bounded flows the model requires a fine grid to resolve the small scale motion near the wall because both k and ε vary as y^2 and large changes in both k and ε occur in the near wall region. In addition, the lack of a natural boundary condition for ε at the wall, where it is not zero, leads to the use of a derived boundary condition, which augments numerical stiffness by tying the wall value of ε to derivatives of k.

2.2.2 Low-Reynolds-number linear $q - \zeta$ turbulence model. The eddy viscosity μ_t can be defined in terms of $q(=\sqrt{k})$ and $\zeta(=\bar{\epsilon}/2q)$ as

$$\mu_t = \bar{\rho} C_\mu f_\mu \frac{q^3}{2\zeta} \tag{17}$$

and the Favre-averaged mean equations for q and ζ are expressed as

$$\frac{\partial \bar{\rho}\bar{u}_{j}\zeta}{\partial x_{j}} = \frac{\partial}{\partial x_{j}} \left(\mu \frac{\partial \zeta}{\partial x_{j}}\right) + \frac{\partial \bar{\rho}\bar{D}_{\zeta j}^{\prime}}{\partial x_{j}} + \frac{\bar{G}_{\zeta}}{\text{production}}
- \bar{\rho}\bar{D}_{\zeta} - \frac{4}{3}\bar{\rho}\zeta \frac{\partial \bar{u}_{k}}{\partial x_{k}} + \bar{\rho}\psi$$
(19)

V. Juntasaro et al.

where

228

$$\begin{split} \tilde{G}_{\zeta} &= \frac{\tilde{\rho}\tilde{P}}{2q} = f_{\zeta 1}C_{\zeta 1}\frac{\zeta}{q^{2}}\tau_{ij}\left(\frac{\partial\tilde{u}_{i}}{\partial x_{j}} + \frac{1}{3}\frac{\partial\tilde{u}_{k}}{\partial x_{k}}\delta_{ij}\right) \\ \tilde{D}_{\zeta} &= f_{\zeta 2}C_{\zeta 2}\frac{\zeta^{2}}{q} \\ \\ \tilde{\rho}\tilde{D}'_{\zeta j} &= \frac{\mu_{i}}{\sigma_{\zeta}}\frac{\partial\zeta}{\partial x_{j}} \end{split}$$

where σ_{ξ} , $C_{\xi 1}f_{\xi 1}$, $C_{\xi 2}f_{\xi 2}$ and Ψ are equivalent to σ_{ε} , $2C_{\varepsilon 1}f_{\varepsilon 1}-1$, $2C_{\varepsilon 2}f_{\varepsilon 2}-1$ and E/2q, respectively, in the low-Reynolds-number $k-\varepsilon$ models. The constants $(\sigma_k, \sigma_{\varepsilon}, C_{\mu}, C_{\varepsilon 1}, C_{\varepsilon 2})$, damping functions $(f_{\varepsilon 1}, f_{\varepsilon 2})$ and E are adopted from the low-Reynolds-number $k-\varepsilon$ model of Launder and Sharma (1974).

The damping function f_{μ} proposed by Gibson and Dafa'Alla (1994), is written as

$$f_{\mu} = \exp\left(\frac{-6}{(1 + \frac{Re_{t}}{50})^{2}}\right) \left(1 + 3\exp\left(\frac{-Re_{t}}{10}\right)\right)$$
 (20)

where the turbulent Reynolds number is defined as

$$Re_{t} = \frac{q^3}{2\nu\zeta}.$$
 (21)

2.2.3 Low-Reynolds-number non-linear $q - \zeta$ turbulence model. The non-linear $q - \zeta$ model is introduced to increase the accuracy in predicting the correct anisotropic behaviour near the wall, while maintaining the simplicity of the two-equation models. The non-linear model used in this work treats C_{μ} as a variable rather than a constant and the non-linear Reynolds-stress expression of Pope (1975) is used instead of the linear expression of Boussinesq (1877).

In the present work, the Reynolds-stress expression of Pope (1975), further simplified by Shih *et al.* (1993) and Lien *et al.* (1996), is generalised to account for compressibility effects, and it is written in terms of k and $\bar{\epsilon}$ as

$$\tau_{ij} = -\overline{\rho u_i'' u_j''}$$

$$= \overline{\rho} f_{\mu} C_{\mu} \frac{k^2}{\overline{\epsilon}} 2S_{ij}^* - \overline{\rho} f_{\mu} \frac{k^2}{\overline{\epsilon}^2} Q_{ij}^* - \frac{2}{3} \overline{\rho} k \delta_{ij} \qquad (22)$$
linear seem quadratic term

and in terms of q and ζ as

$$\tau_{ij} = -\overline{\rho} u_i^n u_j^n$$

$$= \overline{\rho} f_\mu C_\mu \frac{q^3}{2\zeta} S_{ij}^* - \overline{\rho} f_\mu \frac{q^4}{4\zeta_s^2} Q_{ij}^* - \frac{2}{3} \overline{\rho} q^2 \delta_{ij} \qquad (23)$$
tipear term quadratic term

where

$$S_{ij}^* = S_{ij} - \frac{1}{3} \delta_{ij} S_{kk}, \quad Q_{ij}^* = Q_{ij} - \frac{1}{3} \delta_{ij} Q_{kk}$$

where the mean strain rate S_{ij} and vorticity Ω_{ij} are given by

$$S_{ij} = \frac{1}{2} \left(\frac{\partial \tilde{u}_i}{\partial x_j} + \frac{\partial \tilde{u}_j}{\partial x_i} \right), \quad \Omega_{ij} = \frac{1}{2} \left(\frac{\partial \tilde{u}_i}{\partial x_j} - \frac{\partial \tilde{u}_j}{\partial x_i} \right).$$

The quadratic term is defined as

$$Q_{ij} = q_1 S_{ik} S_{jk} + q_2 (S_{ik} \Omega_{jk} + S_{jk} \Omega_{ik}) + q_3 \Omega_{ik} \Omega_{jk} q_1$$

$$= \frac{3}{f(\bar{S})},$$

$$q_2 = \frac{15}{f(\bar{S})}, \quad q_3 = \frac{19}{f(\bar{S})}$$

where

$$f(\tilde{S}) = 1000 + \tilde{S}^3$$

$$\tilde{S} = \frac{q}{2\zeta} \sqrt{2S_{ij}S_{ij}}, \quad \tilde{\Omega} = \frac{q}{2\zeta} \sqrt{2\Omega_{ij}\Omega_{ij}}$$

 C_{μ} is treated as a variable and defined as

$$C_{\mu} = \frac{2/3}{A_1 + f_{\mu} \tilde{S} + A_2 f_{\mu} \tilde{\Omega}}$$
 (24)

where the damping function f_{μ} of Cotton and Kirwin (1995) is used and constants A_1 and A_2 are re-optimised to 4 and 0.5 (section 3) using fully developed turbulent channel flow as a test case, and the f_{μ} of Cotton and Kirwin is written as:

$$f_{\mu} = 1 - 0.97 \exp\left(\frac{-Re_t}{160}\right)$$

- 0.0045 Re_t exp $\left(-\left(\frac{Re_t}{200}\right)^3\right)$ (25)

3. Re-evaluation of f_{μ} and C_{μ}

This section presents a comparative study of different expressions for the damping function, (f_{μ}) , to find the most suitable for use in low-Reynolds-number turbulence models, followed by the re-optimisation of the constants in the expression of C_{μ} for the non-linear $q-\zeta$ model. The fully developed turbulent channel flow is used as a test case because it is simple and has well-established reliable DNS data.

The results presented and compared against the DNS data of Kim et al. (1987) are calculated on a non-uniform independent grid of 65 nodes across the flow. The non-dimensional axial velocity U^+ , turbulence kinetic energy k^+ , dissipation rate ϵ^+ and shear Reynolds-stress \overline{uv}^+ are

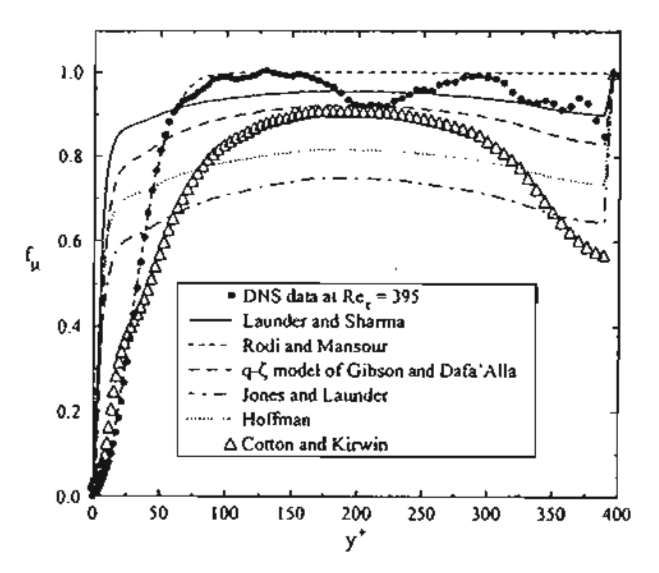


Figure 1. Distribution of $f_n(v^+)$.

plotted against distance from the wall y^+ in figures 3 and 4 for Re_r(= U_rh/ν) of 180 and 395, respectively.

The comparative study of different expressions for damping functions (f_{μ}) is first considered. For two-dimensional boundary layers, the distribution of f_{μ} can be obtained (Patel et al. 1985) from:

$$\mathcal{L}_{\mu} = \frac{1 - \epsilon_{\mu} \epsilon_{\mu}}{C_{\mu} k_{\mu} \left(\frac{\epsilon_{\mu}}{d\epsilon_{\mu}}\right)} \tag{26}$$

The DNS turbulent channel flow data at $Re_{\tau} = 395$ are substituted in the above equation in order to obtain the distribution for f_{μ} and this is then compared (figure 1) with the expressions in table 1. The expression of Rodi and Mansour (1995) agrees well with the DNS data but unfortunately is expressed in terms of y^+ and it is more desirable to express f_{μ} in terms of Re_{μ} , section 2.2.1, and to this end figure 2 replots figure 1 in terms of Re_{μ} . In order to find a more accurate expression for f_{μ} , the DNS data are curve fitted and the resulting expression is used for f_{μ} . However, this produces no improvement in accuracy compared to expressions used by other workers

Table 1. Expression of f_{μ} .

Launder and Sharma (1974)	$\exp\left(\frac{-3.4}{(1+\frac{8\alpha}{2})^2}\right)$
Rodi and Mansour (1995)	$1 = \exp(-0.0002y^{2} - 0.00065y^{+2})$
Gibson and Dafa Alfa (1994)	$\exp\left(\frac{-6}{\left(1+\frac{R_{f_2}}{4}\right)^2}\right)\left(1+3\exp\left(\frac{-R_{f_2}}{10}\right)\right)$
Jones and Launder (1972)	$\exp\left(\frac{-2.5}{1+\frac{R_{\odot}}{4}}\right)$
Hoffman (1975)	$\exp\left(\frac{-1}{1+\frac{Nc_2}{4}}\right)$
Cotton and Kirwin (1995)	$t = 0.97 \exp(\frac{-R_{\odot}}{160}) = 0.0045$
	$Re_i \exp\left(-\left(\frac{Re_i}{500}\right)^3\right)$

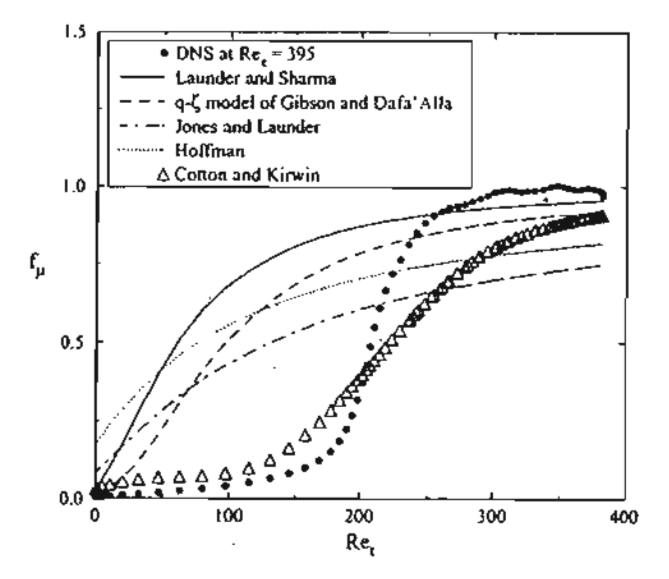


Figure 2. Distribution of $f_{\mu}(Re_i)$.

which may be due to the difficulty of obtaining an accurate curve-fit. In a last attempt to use the f_{μ} distribution derived from the DNS data, a "table lookup" approach is adopted but while the trends of the DNS data are reproduced the agreement is not close (figure 4) and this is probably due to two reasons. The first reason is that the previous idea that an accuracy of the results will be improved by the use of f_{μ} expression that follows the DNS curve is not true, and the second reason is that Remay not be the most suitable parameter to be used in f_{μ} expression and a more suitable parameter may be required.

The comparison of the accuracy of the channel flow predictions (figures 3 and 4) using different expressions for f_{μ} , table 1 shows that the linear $q = \zeta$ model with the f_{μ} formulation of Cotton and Kirwin (1995) exhibits a closer agreement of k^+ and ϵ^+ to the DNS data than the original formulation of Gibson and Dafa' Alla (1994). The peak of k + is well predicted resulting in the correct nearwall trend of e+. Unfortunately, the predicted axial velocity U^+ from the linear $q - \zeta$ model with the f_{μ} formulation of Cotton and Kirwin does not follow the loglaw profile in the logarithmic region. Furthermore, the normal Reynolds-stresses are not accurately predicted (figures 5 and 6) because the model is based on Boussinesq (1877) approximation and as a result, the three components of normal Reynolds-stress $\overline{u}\overline{u}^+, \overline{v}\overline{v}^+$ and www are all predicted to be equal and this disagrees with the DNS data.

The non-linear $q = \zeta$ model of Ong (1997) based on non-linear Reynolds-stresses expression of Pope (1975) with variable $C_{\mu\nu}$ i.e.

$$C_{\mu} = \frac{2/3}{A_1 + f_{\mu}\bar{S} + A_2 f_{\mu}\bar{\Omega}}, A_1 = 2.5 \text{ and } A_2 = 0.9$$
 (27)

predicts anisotropic behaviour near the wall (figures 5 and 6). However, the distributions of U^+ and shear stress

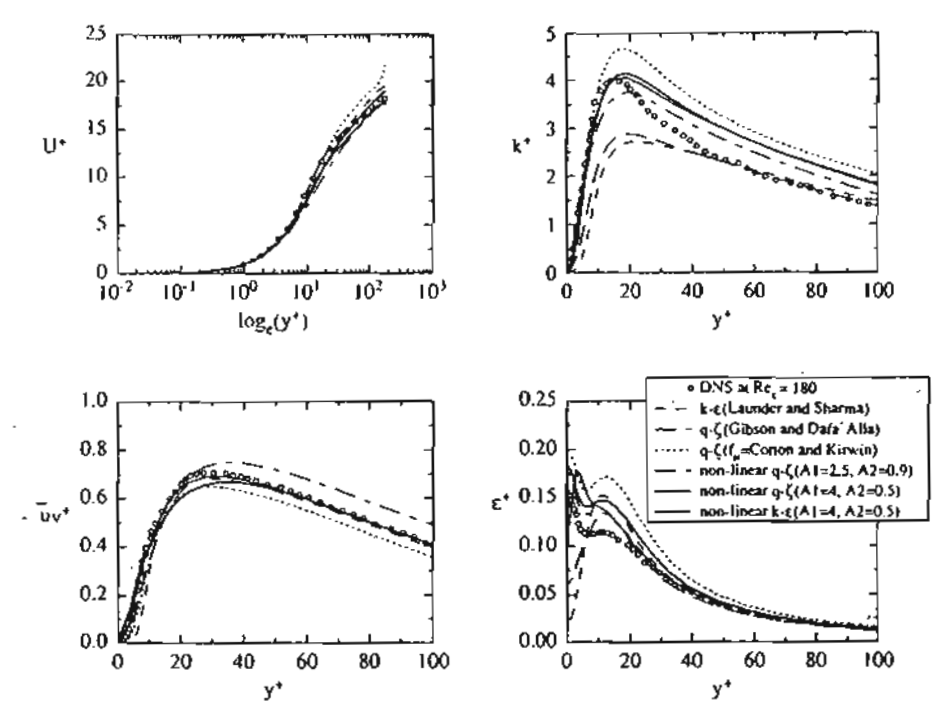


Figure 3. Fully developed turbulent channel flow at Re, = 180.

 \overline{uv}^+ are not well predicted in the logarithmic region and the peak of k^+ is also lower than the linear $q - \zeta$ model using f_{μ} of Cotton and Kirwin.

The non-linear $q = \zeta$ model is thus modified via the two constants A_1 and A_2 , equation (27), and are re-optimised to 4 and 0.5, respectively. The predicted U^+ and \overline{uv}^+ are now closer to the DNS data in the logarithmic region and the peak of k^+ is improved (figures 3 and 4).

4. Subsonic flow in a circular-to-circular S-shaped diffusing duct

This section presents the modelling of subsonic flow in the DRA M2129 circular-to-circular S-shaped diffusing duct, whose test conditions correspond to AGARD (1991) test case 3.2. The inlet Mach number is 0.412 and the Reynolds number is 1.15×10^6 . The DRA

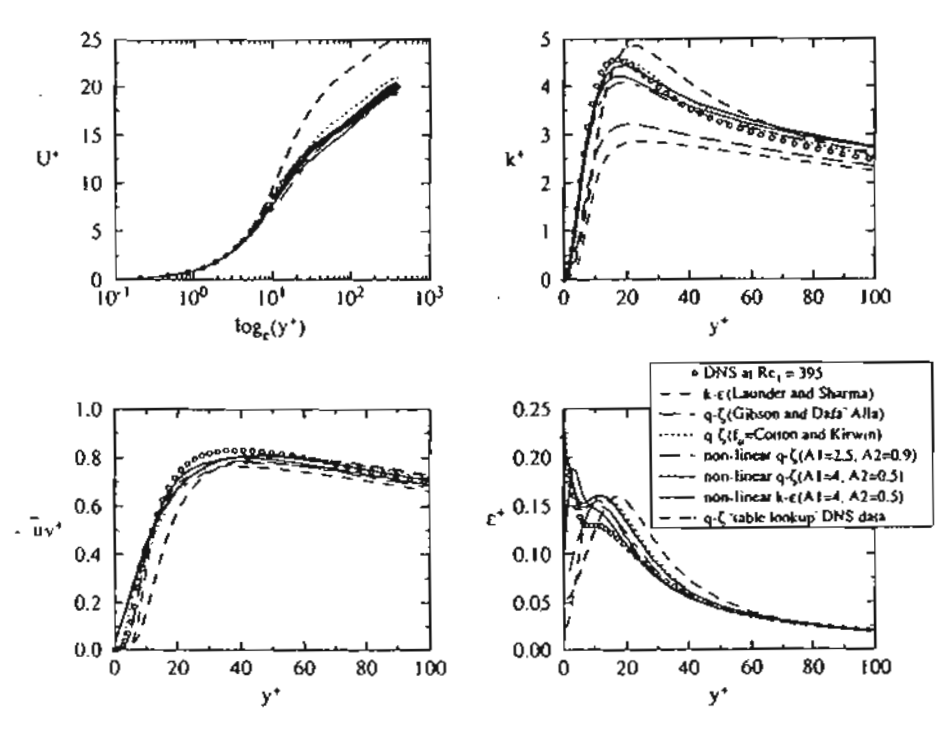


Figure 4. Fully developed turbulent channel flow at Re, = 395.

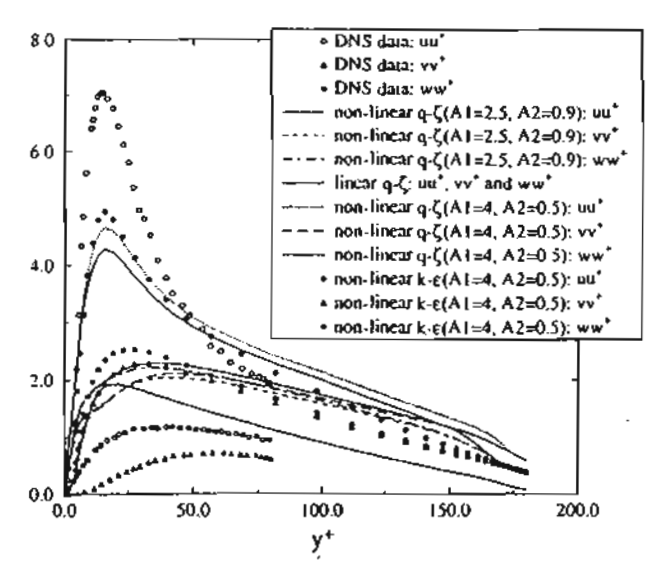


Figure 5. Normal Reynolds-stresses at Re, = 180.

(Defence Research Agency, former Royal Aerospace Establishment) wind tunnel test data of Gibb and Jackson (1992) and the predictions from the non-linear $q - \zeta$ model of Ong (1997) will be used for comparison.

4.1 Computational domain and numerics

The wind tunnel model of circular-to-circular S-duct used by DRA has inlet $(D_{\rm inlet})$ and exit $(D_{\rm exit})$ diameters of 128.8 and 152.4 mm, respectively, a length (L) of 457.2 mm, an offset between the centre-line of the inlet and exit planes $O_f/L=0.3$, and a duct area ratio between the exit and inlet planes (A_R) of 1.4. Table 2 describes the variation of the diameter and offset along the duct and a three-dimensional perspective view of the S-duct geometry is shown in figure 7.

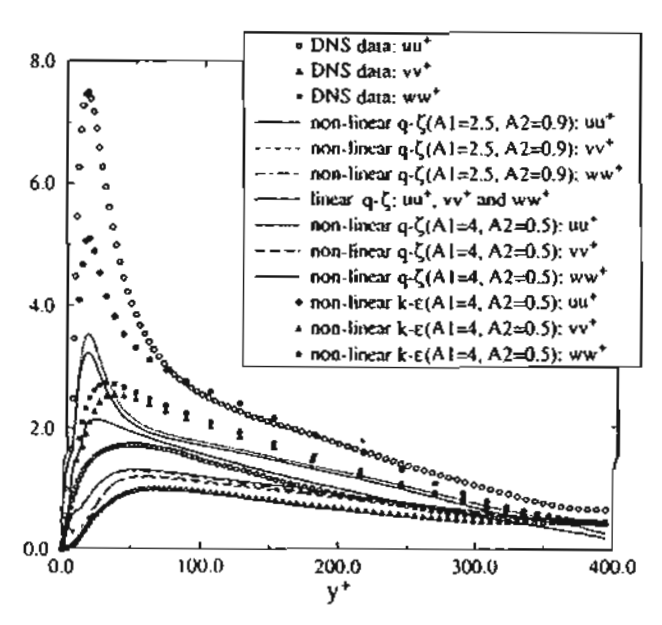


Figure 6. Normal Reynolds-stresses at Re, = 395.

Table 2. Profiles of the M2129 circular-to-circular \$-bend.

Diameter (D)	$\frac{n - p_{\text{out}}}{p_{\text{out}} - p_{\text{out}}} = 3\left[1 - \left(\frac{\chi}{t}\right)^4\right] - 4\left[1 - \left(\frac{\chi}{t}\right)\right]^4 + 1$
Offset (Z)	$\frac{2}{L} = \frac{Q_L}{2L} \left[1 - \cos\left(\pi \frac{\chi}{L}\right) \right]$

The actual wind tunnel model described in AGARD (1991) test cases also comprises a constant area circular section upstream of the duct, whose length is $0.85D_{\rm exit}$, or 129.5 mm. Therefore, the inflow boundary of the S-duct is implemented at a station that is $70 \,\mathrm{mm} \ (\approx 0.46 D_{\mathrm{exit}})$ upstream of the inlet plane, and the inflow boundary conditions for the dependent variables of the duct are obtained from a separate developing pipe flow computation. In this separate pipe flow computation, the inflow velocity profile is assumed to be uniform and the boundary layer is allowed to develop from zero thickness at its inflow. The turbulence kinetic energy at the inflow of the pipe calculation is prescribed based on a 8% turbulence intensity, and the turbulence length-scale (l_m) is prescribed using the formulation of Patankar and Spalding (1970) that $l_m = \lambda \delta$ in the core flow; λ is a constant of 0.09 and δ is the duct height. Further information regarding the inlet is presented in Table 3. The outflow boundary is located at about 0.21D_{exit} downstream of the exit plane, and the region between the exit plane and the out flow boundary is bridged by a straight circular duct conducting the flow to ambient air.

The S-duct geometry is symmetrical about X-Z plane (figure 7), hence, only half of the duct is modelled, and since an O-grid conforms well to a circular cross-section, it is employed in the present configuration using transfinite interpolation with grid clustering near the wall to generate the near-orthogonal grid. The domain is discretised into an independent grid of 55 (circumferential) by 45 (radial) by 62 (streamwise) grid points.

The modifications with respect to turbulence models made in this work are implemented in an existing computer program called BOFFIN which was originally written by Jones (1988). The program uses a finite volume scheme with a collocated grid arrangement to solve 3D flow through complex geometries using boundary fitted co-ordinates.

4.2 Flow in the plane of symmetry

In the wind tunnel test, the velocity field within the diffusing duct was not measured, however, surface flow visualisation was performed (figure 8) and this is used for comparison against the computations. In figure 8, the flow direction is from left to right with the upper part of the duct on the top and the lower part on the bottom of the figure. From the experimental data, a region of flow separation is observed on the bottom surface, and by using the marking tapes on the test section as a reference distance, the onset of separation is at $X/D_{\rm exit} \approx 1.0$ in the first bend, and the flow re-attaches after $X/D_{\rm exit} \approx 2.45$ in the second bend.

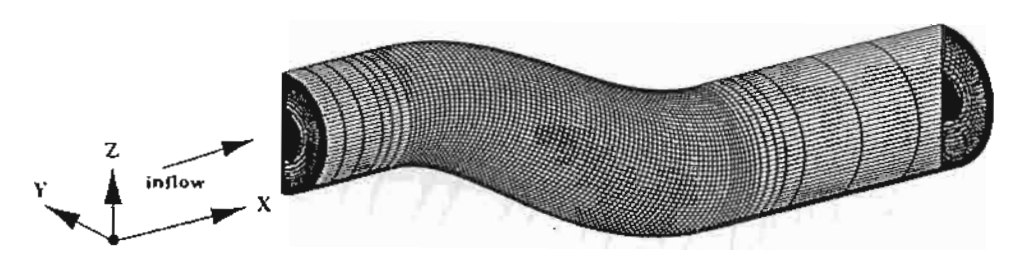


Figure 7. Three-dimensional perspective view of the S-duct geometry.

Table 3 Inflow conditions (AGARD AR-270).

Total pressure	1 01123 × 10 ⁵ Pa
Total temperature	293 K
Throat Mach number	0.412
Inlet Reynolds number	1.15×10 ⁶

Figure 9 presents the computed mean axial velocity profiles in the plane of symmetry. The figure shows that the flow is accelerated along the convex curvature over the first bend and the boundary layers are thicker on the bottom surface after the first bend. The separation bubble is identified in figure 9 by joining the locations with zero mean axial velocity at successive stations. The modified non-linear $q = \zeta$ model predicts the onset of separation at $X/D_{\rm exit} \approx 1.10$, and re-attachment at $X/D_{\rm exit} \approx 2.70$. The modified non-linear $q - \zeta$ model shows an improvement on the predicted location of the separation over Ong $(X/D_{\rm exit} \approx 1.30)$, however, the predicted re-attachment location has not improved and is still over-predicted. This is probably because the present calculation does not include the bullet (after-body) at the exit plane of the wind tunnel model. The bullet is not included because the present work concentrates on the development of the turbulence model and it is more appropriate to simplify the geometry. A summary of the predicted locations of the separation bubbles is presented in table 4.

4.3 Surface pressure predictions

Figure 10 compares the predictions of surface pressure along the top, side and bottom surfaces of the duct with the wind tunnel test data. Static pressures on the respective surfaces of the wall are normalised by the inlet total pressure and plotted against the normalised length of the duct.

The pressure distribution along the bottom surface of the experimental data shows an abrupt change in the pressure gradient at $X/D_{\rm exit} \approx 1.0$ and at $X/D_{\rm exit} \approx 2.45$, which correspond to the locations of the separation and reattachment observed in the surface flow visualisation in figure 8, respectively. The modified non-linear $q - \zeta$ model predicts an abrupt change in the pressure gradient at $X/D_{\rm exit} \approx 1.10$, which coincides with the predicted location of the separation in the axial velocity profiles in the plane of symmetry, and represents an improvement with respect to the non-linear $q - \zeta$ model of Ong which over-predicted the separation $(X/D_{\rm exit} \approx 1.30)$ (figure 9).

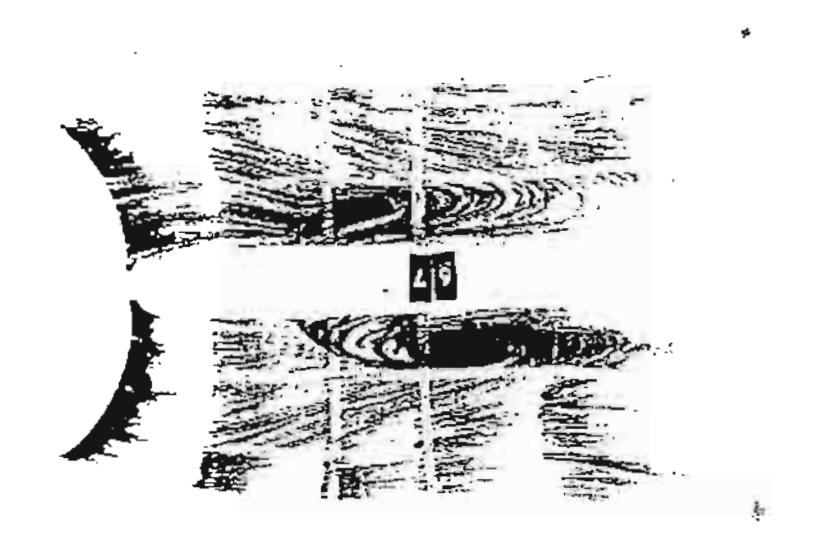
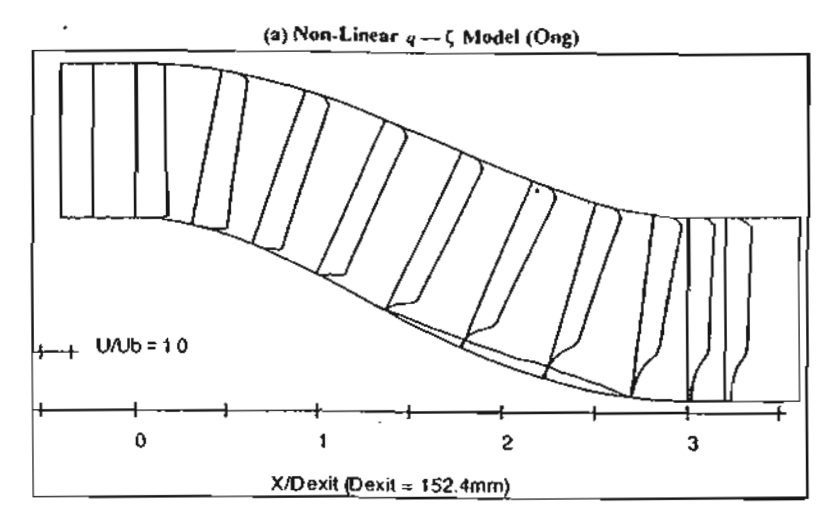


Figure 8. Surface flow visualisation (not to scale).



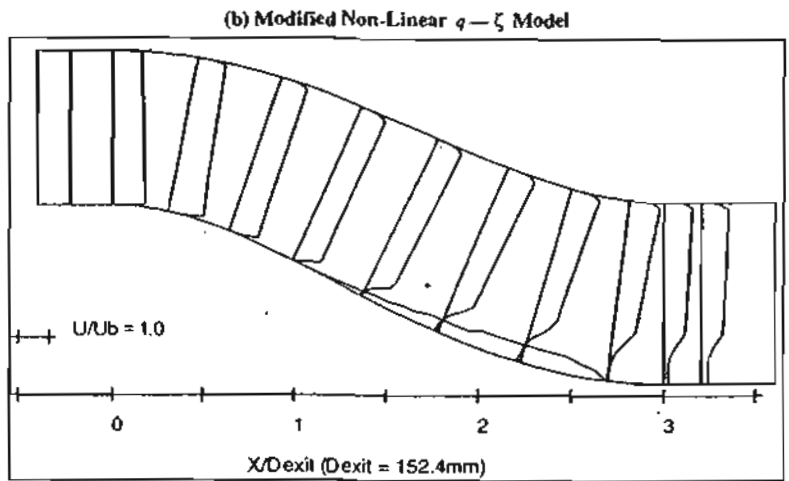


Figure 9. Axial velocity profiles in the plane of symmetry.

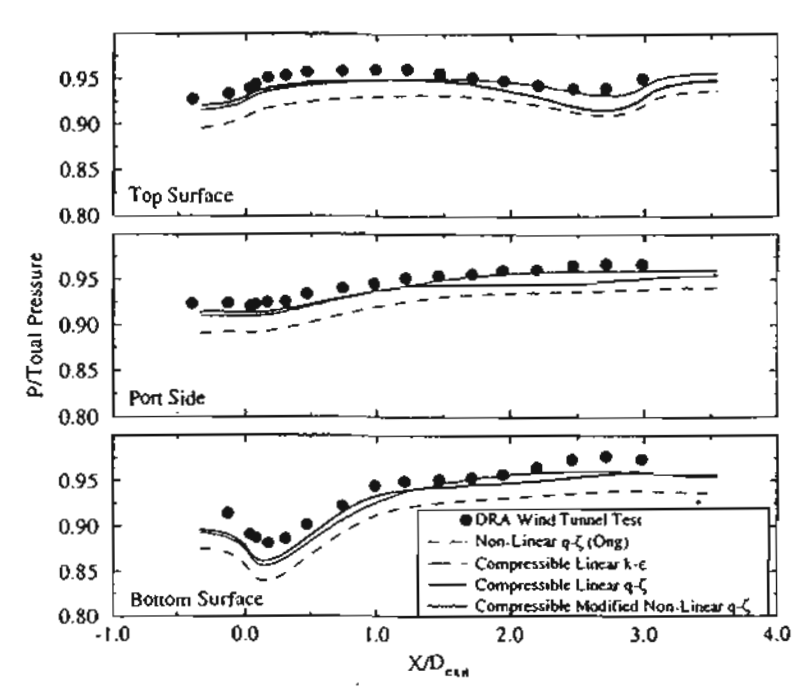


Figure 10. Normalised static pressure along the top surface, port side and bottom surface.

Table 4. Size of the predicted separation.

Furbulence model	Bubble length, X/D _{exit}	
	Onset	Re-attochment
Experiment	3.0	2 45
Non-linear $q = \zeta$ (Ong)	1.30	2.70
Modified non-linear $q = \zeta$	1.10	2.70

5. Conclusions

A comparative study of different expressions for damping functions (f_n) is made to find the most suitable use in low-Reynolds-number turbulence models using the fully developed turbulent channel flow as a basis for comparison. The non-linear $q - \zeta$ model is then modified via the two constants in C_{μ} using the re-optimised values $A_1 = 4$ and $A_2 = 0.5$. The predictions using the non-linear $q = \zeta$ model with the damping function f_{μ} of Cotton and Kirwin and the re-optimised constants in the expression of C_{μ} show the best agreement with the DNS data. The modified model is then evaluated for more complex flow problems in three-dimensional turbulent flow in an Sshaped diffusing duct where the effects of stream line curvature and flow separation are important. The comparison between the predicted results and the experimental data shows that the modified model is able to predict the main flow features in complex flows accurately.

Acknowledgements

The authors would like to thank Professor W.P. Jones for letting the authors use his computer program called BOFFIN as the basic program in the authors' work. This research is partially supported by the Thailand Research Fund (TRF). Special thanks are due to Assistant Professor Ekachai Juntasaro.

References

- AGARD, Air intakes for high speed vehicles, Technical Report AGARD-AR-270, 1991.
- Boussinesq, J., Theory de L'ecoulment Tourbillant, Memoires Presentes Par Divers Savants Sciences Mathematique at Physiques, Academic de Sciences, 1877, 23, 46-50
- Cotton, M.A. and Kirwin, P.J., A variant of the low-Reynolds-number two-equation turbulence model applied to variable property mixed convection flows. *Int. J. Heat Fluid Flow*, 1995, 16(6), 486–492.
- Gibb, J. and Jackson, M., Some preliminary results from tests using vortex generators in the circular/circular diffusing S-duct model M2129. Technical report. 1992, DRA, Bedford, Bedfordshire, UK.
- Gibson, M.M. and Dafa Alla, A.A., Two-equation model for turbulent wall flow. AIAA J., 1994, 33(8), 1514-1518.
- Hoffman, G.H., Improved form of the low Reynolds number k = e turbulence model. Phys. Fluids, 1975, 18, 309-312.
- Jones, W.P., BOFFIN: A computer program for flow and combustion in complex geometries. *Technical report*. Department of Chemical Engineering, Imperial College of Science, Technology and Medicine. 1000
- Jones, W.P. and Launder, B.E., The prediction of laminarization with a two-equation model of turbulence. *Int. J. Heat Mass Transfer*, 1972, 15, 301-314.
- Kim, J., Moin, P. and Moser, R., Turbulence statistics in fully developed channel flow at low Reynolds number. J. Fluid Mech., 1987, 177, 133-166.
- Launder, B.E. and Sharma, B.I., Application of the energy dissipation model of turbulence to the calculation of flow near a spinning disc. Lett. Heat Moss Transfer, 1974, 1, 131-138.
- Lien, F.S., Chen, W.L. and Leschziner, M.A., Low Reynolds-number eddy-viscosity modelling based on non-linear stress-strain/vorticity relations. In Engineering Turbulence Modelling and Experiments 3, edited by W. Rodi and G. Bergeles, pp. 91-100, 1996 (Elsevier Science B.V.: Amsterdam).
- Ong, L.Y., Experimental and numerical studies of S-shaped diffusing ducts Ph.D. Thesis, Department of Mechanical Engineering, Imperial College of Science, Technology and Medicine, University of Landon, 1997.
- Patankar, S.V. and Spalding, D.B., Heat and Mass Transfer in Boundary Layers, 1970 (Intertext Books: London).
- Patei, V.C., Rodi, W. and Scheuerer, G., Turbulence models for near-wall and low reynolds numbers flows: a review. AIAA J., 1985, 23(9): 1308-1319.
- Pope, S.B., A more general effective-viscosity hypothesis. J. Fluid Mech., 1985, 72, 331-340.
- Rodi, W. and Mansor, N.N., Low Reynolds number k = ε modelling with the aid of direct simulation data. J. Fluid Mech., 1995, 250, 509-529.
- Shih, T.H., Zhu, J. and Lumley, J.L., 1993. A realizable Reynolds stress algebraic equation model, Technical Report NASA TM-105993
- Wilcox, D.C., 1993. Turbulence Modeling for CFD, DCW Industries Inc.

บทความทางวิชาการ เรื่อง

Adaptive Delaunay Triangulation with Multidimensional Dissipation Scheme for High-Speed Compressible Flow Analysis

Published in the

Journal of Applied Mathematics and Mechanics

Vol. 26, No. 10, pp. 1341-1356 2005 ©Editorial Committee of Appl. Math. Mech. , ISSN 0253-4827

Article ID: 0253-4827(2005)10-1341-16

ADAPTIVE DELAUNAY TRIANGULATION WITH MULTIDIMENSIONAL DISSIPATION SCHEME FOR HIGH-SPEED COMPRESSIBLE FLOW ANALYSIS*

P. Dechaumphai, S. Phongthanapanich

(Mechanical Engineering Department, Chulalongkorn University, Bangkok 10330, Thailand)

(Communicated by ZHOU Zhe-wei)

Abstract: Adaptive Delaunay triangulation is combined with the cell-centered upwinding algorithm to analyze inviscid high-speed compressible flow problems. The multidimensional dissipation scheme was developed and included in the upwinding algorithm for unstructured triangular meshes to improve the computed shock wave resolution. The solution accuracy is further improved by coupling an error estimation procedure to a remeshing algorithm that generates small elements in regions with large change of solution gradients, and at the same time, larger elements in other regions. The proposed scheme is further extended to achieve higher-order spatial and temporal solution accuracy. Efficiency of the combined procedure is evaluated by analyzing supersonic shocks and shock propagation behaviors for both the steady and unsteady high-speed compressible flows.

Key words: adaptive meth movement; Delaunay triangulation; cell-centered upwinding; high-speed compressible flow

Chinese Library Classification: O354.5; O241.82 Document code: A 2000 Mathematics Subject Classification: 76N15; 76L05; 65M12; 65N50

Introduction

High-speed compressible flows normally involve many complex flow phenomena, such as shock waves, flow expansions, and shock-shock interactions^[1]. Effects of these phenomena are critical in the design of high-speed structures. These flows are characterized by steep solution gradients that need robust analyses and computational techniques as well as dense meshes to obtain good resolution of flow behaviors. Several algorithms had been introduced into the computational modelings, such as the Taylor-Galerkin^[2], the Petrov-Galerkin^[3], the least-squares^[4], and the cell-centered upwinding algorithms^[5].

Among these algorithms, the cell-centered upwinding algorithm based on the Roe's

^{*} Received Mar. 10,2004

Project supported by the Thailand Research Fund (TRF)

Corresponding author P. Dechaumphai, Professor, Doctor, E-mail:fmepde@eng.chula.ac.th

flux averaging⁽⁶⁾ is selected for solutions in this paper due to its efficiency to provide solution accuracy with less computational effort. The algorithm, however, may produce unrealistic results near shock waves especially for flow at high mach numbers. One of such results is referred as the carbuncle phenomenon^[7] that arises due to the use of one-dimensional upwinding numerical flux for multidimensional problems. To avoid this effect, the H-correction entropy fix^[8] has been introduced and applied to the standard cell-centered upwinding algorithm for structured rectangular meshes. In this paper, the H-correction entropy fix is modified for unstructured triangular meshes arbitrarily generated from the adaptive Delaunay triangulation technique.

The Delaunay triangulation and an adaptive remeshing technique are implemented to improve solution accuracy of the numerical analysis. The Delaunay triangulation^[9,10] used in the construction of triangular meshes for arbitrary two-dimensional geometries, will be first described. Since the Delaunay triangulation in itself does not include procedures for creating nodes inside the domain, additional nodes are generated by an algorithm that was developed by Weatherill and Hassan^[11] and introduced as Object Oriented Programming by Karamete et al. ^[12]. Hence, the proposed procedure can construct meshes with required nodal density and triangulation regularity for arbitrary two-dimensional domains.

To further improve the analysis solution accuracy, an adaptive remeshing procedure is also implemented into the Delaunay triangulation. An entirely new mesh is generated according to the solutions of a previous mesh. An error indicator identifies and activates the adaptive remeshing in regions where finer elements are required. A cell-centered upwinding computer program has been developed and verified by problems with exact solutions prior to solving practical problems. In recent years, various grid adaptation methods, such as adaptive remeshing or adaptive mesh refinement (AMR)^[13-20], have been proposed to improve numerical accuracy for computational fluid dynamics. The AMR is easier to implement on structured grid but needs efficient hierarchy data structure handling routine to manage information that transfers between grid levels. Such difficulty increases if unstructured triangular grids are selected to discretize more complex domain. Currently, implementation of unstructured grids using adaptive remeshing technique is common because of straightforward data structure handling routine. However, the unstructured mesh regeneration is time consuming. The AMR method thus normally requires less computational time as compared to the adaptive remeshing technique.

The paper first outlines the Euler equations used in the analysis of high-speed compressible flows and the solution procedure that lead to the computer program development. The basic concepts of the Delaunay triangulation and the adaptive remeshing technique are then described. The presented scheme is further extended to higher-order solution accuracy and then evaluated by several test cases. Finally, the combined procedure is evaluated by analyzing a series of both the steady-state and transient high-speed compressible flow problems.

1 Higher-Order Cell-Centered Upwinding Algorithm

1.1 Governing differential equations

The Euler equations for inviscid high-speed compressible flows consist of conservation

of mass, momentums, and energy. These equations, in two dimensions, are written in the conservation form^[21] as

$$\frac{\partial U}{\partial t} + \frac{\partial E}{\partial x} + \frac{\partial G}{\partial y} = 0. \tag{1}$$

The vector U is the conservation variables and is defined by $[\rho \quad \rho u \quad \rho v \quad \rho \varepsilon]^T$, where ρ is the fluid density, u and v are the velocity components in x- and y-directions, respectively, and ε is the total energy. The vectors E and G consist of the inviscid fluxes in the x- and y-directions, respectively, and the vector G contains the force and energy terms associated with the body force as

$$E = \begin{cases} \rho u \\ \rho u^{2} + p \\ \rho uv \\ \rho u\varepsilon + pu \end{cases}, \quad G = \begin{cases} \rho v \\ \rho uv \\ \rho v^{2} + p \\ \rho v\varepsilon + pv \end{cases}, \quad J = \begin{cases} 0 \\ \rho f_{x} \\ \rho f_{y} \\ \rho (uf_{x} + vf_{y}) \end{cases}, \tag{2}$$

where p is the pressure, f_x and f_y are the x and y components of gravitational force. The total energy is composed of the internal and the kinetic energy defined by $\varepsilon = e + (u^2 + v^2)/2$. The internal energy e is assumed to satisfy the stiffened gas equation of state for compressible medium^[22].

$$\rho e = (p + \gamma p_{\infty})/(\gamma - 1), \qquad (3)$$

where γ is a constant and p_{∞} is a pressure-like constant. For water, $\gamma = 5.5$ and $p_{\infty} = 492$ MPa. Eq. (3) is equivalent to the gas equation of state when $p_{\infty} = 0$ and γ is the specific heat ratio.

1.2 Cell-centered upwinding formulation

By integrating Eq. (1) over a control volume, Ω , and applying the divergence theorem to the resulting flux integral.

$$\frac{\partial}{\partial t} \int_{\Omega} U d\Omega + \int_{\partial \Omega} F \cdot n dS = \int_{\Omega} J d\Omega, \qquad (4)$$

where F is the numerical flux vector and n is the unit normal vector of the cell boundary. The numerical flux vector at the cell interface between the left cell L and the right cell R according to the Roe's scheme^[6,21] is

$$F_{n} = \frac{1}{2} (F_{nL} + F_{nR}) - \frac{1}{2} \sum_{k=1}^{4} \alpha_{k} | \lambda_{k} | r_{k}, \qquad (5)$$

where α_k is the wave strength of the kth wave, λ_k is the eigenvalue, and r_k is the corresponding right eigenvector. The eigenvalues in the above Eq. (5) are

$$\lambda_{k} = \begin{bmatrix} V_{n} - a & V_{n} & V_{n} & V_{n} + a \end{bmatrix}^{\mathsf{T}}, \tag{6}$$

where V_n is the normal velocity, and a is the speed of sound at the cell interface. To avoid such unphysical solutions due to the original Roe's scheme does not admit entropy condition^[23], the eigenvalues $|\hat{\lambda}|$ are modified according to Ref. [8] yielding the $|\hat{\lambda}|$ such that

$$|\hat{\lambda}|^* = \max(|\hat{\lambda}|, \eta^H), \tag{7}$$

where η^H is called *H*-correction entropy fix. For the triangular cell interfaces as shown in Fig. 1, the proposed *H*-correction entropy fix is

$$\eta'' = 0.5 \max(\eta_1, \eta_2, \eta_3, \eta_4, \eta_5),$$
 (8)

where η_i , i = 1 to 5 are determined from $\eta_i = 0.5 \text{ max}(||\lambda_{iR} - \lambda_{iL}||)$.

By substituting Eq. (5) into Eq. (4) and applying an explicit time marching algorithm, the increment of the element conservation variables at the new time step m + 1 can be determined from

$$\Delta U^{m+1} = -\frac{\Delta t}{2\Omega} \sum_{n=1}^{3} \delta \left[\left(F_{nL} + F_{nR} \right) - \sum_{k=1}^{4} \alpha_{k} \left| \lambda_{k} \right| r_{k} \right] + \frac{\Delta t}{\Omega} \int_{\Omega} J d\Omega, \tag{9}$$

where Δt is the time step and δ is the length of element side. The nodal conservation variables are then computed by averaging the quantities from all elements surrounding that node.

1.3 Linear reconstruction and second-order temporal discretization

Solution accuracy from the first-order formulation described in the preceding section can be improved by implementing a higher-order formulation for both the space and time. A higher-order spatial discretization is achieved by applying the Taylor' series expansion to the cell-centered solution for each cell face^[24]. For instance, the solutions at the midpoint of an element edge between nodes 1 and 2 shown in Fig. 2, can be reconstructed from

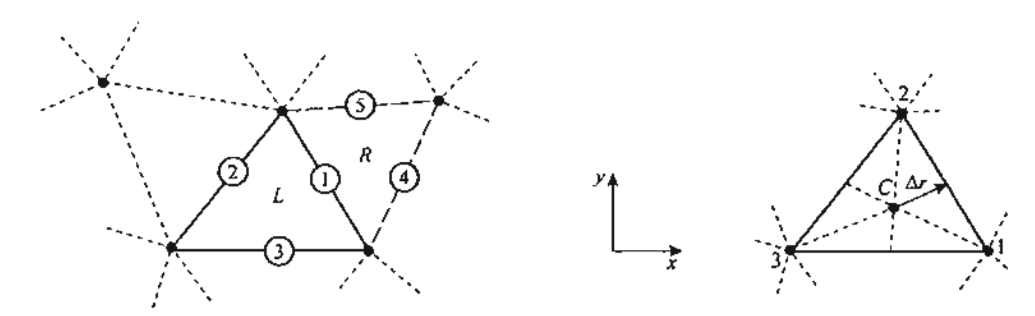


Fig. 1 Cell interfaces of a typical unstructured triangular mesh

Fig. 2 Linear reconstruction on a typical triangular element

$$q_{f_{0.1}} = q_c + \frac{\Psi_c}{3} \left[\frac{(q_1 + q_2)}{2} - q_3 \right], \tag{10}$$

where $q = [\rho \ u \ v \ p]^T$ consists the primitive variables of the density, the velocity components, and the pressure, respectively; q_c is the solution at the element centroid; q_a , n = 1,2,3 are the solutions at nodes. In this paper, the inverse-distance weighting from the centroid to the nodes that preserves the principle of positivity^[25] is used

centroid to the nodes that preserves the principle of positivity^[25] is used
$$q_n = \sum_{i=1}^N \frac{q_{C,i}}{\mid r_i \mid} / \sum_{i=1}^N \frac{1}{\mid r_i \mid},$$
(11)

where $q_{c,i}$ are the surrounding cell-centered values of node i, $|r_i|$ is the distance from the centroid to node i, and N is the number of the surrounding cells. The Ψ_c in Eq. (10) represents the limiter for preventing spurious oscillation that may occur in the region of high gradients. In this study, Vekatakrishnan's limiter function [26] is selected.

The second-order temporal accuracy is achieved by implementing the second-order accurate Runge-Kutta time stepping method^[27]

$$U_{i}^{*} = U_{i}^{n} - \frac{\Delta t}{\Omega_{i}} \sum_{j=1}^{3} F^{n} \cdot n_{j}, \quad U_{i}^{n+1} = \frac{1}{2} \left[U_{i}^{0} + U_{i}^{*} - \frac{\Delta t}{\Omega_{i}} \sum_{j=1}^{3} F^{*} \cdot n_{j} \right].$$
 (12)

To reduce computational effort, the local element time steps are used for steady-state analysis, while the minimum global time step proposed in Ref. [28] is used for the transient analysis.

2 Delaunay Triangulation

2.1 Mesh generation procedure

For a given set of points in space, $\{P_k\}$, $k=1,\cdots,n$, the regions $\{V_k\}$, $k=1,\cdots,n$, are boundaries assigned to each point P_k and represent the space closer to P_k than to any other points in the set. Therefore, these regions satisfy

$$V_{k} = \{P_{i}: | p - P_{i}| < | p - P_{j}|, \forall j \neq i\}.$$
 (13)

If all points which have some segments of a Voronoi boundary in common are joined, the resulting shape is a Delaunay triangulation. This defining characteristic of the Delaunay triangles is called the empty circumcircle property. The key idea of the Bowyer-Watson algorithm^[9,10] based on the in-circle criterion is summarized in the Algorithm I below.

Algorithm I Delaunay Triangulation (P, T)

- 1. Let $P = \{p_k, k = 1, \dots, n\}$ be the set of nodes on the domain boundaries and are stored in sequence of counter-clockwise direction for all outside boundaries and clockwise direction for all inside boundaries. Let T be the empty set of Delaunay triangles.
- 2. Create an initial convex hull triangle that contains all boundary nodes and add the triangle to T.
- 3. Read next boundary node p_i from P and search for triangle t_i in T which contains the node p_i . The search starts from the triangle which was last formed and uses Lawson's algorithm^[11,12] to march from one triangle to the next in the direction of p_i . This algorithm performs the path searching strategy and removes the need to search through the entire domain.
- 4. Destroy surrounding triangles of t_i which lie within a circle centered at a vertex of the Voronoi diagram. Delete these triangles from T and, then, form new triangles that are connected to the node p_i . These triangles must pass the in-circle criterion. Add new forming triangles into T and determine the neighboring triangles of the triangles.
 - 5. Repeat Steps 3 and 4 until all nodes in P are considered.
- 6. Search for all triangles that have one or more vertices connected to any vertices of initial convex hull triangles outside the domain or lie inside holes in the domain and delete these triangles from T.

2.2 Automatic point creation procedure

The Delaunay triangulation algorithm described previously does not provide the procedure for creating new nodes inside the domain. So far, researchers have introduced several approaches [11,12,15,29,30] for creating new interior nodes by refining boundary triangles such that the set of boundary points guide new node placements. The automatic point creation procedure in this paper is derived from the algorithm suggested by Weatherill and Hassan [11]. The shape and size of triangles or density of nodes inside the domain are controlled by two coefficients, the Alpha and the Beta coefficients. The Alpha coefficient controls node density by changing the allowable shape of the formed triangles while the Beta

coefficient controls the regularity of triangulation by forbidding the insertion of a new node within a specified distance from others in the same sweep of the triangles within the field. The suggested values of both the Alpha and the Beta coefficients for coarse and fine triangular meshes are 0.8 and 0.9, and 0.5 and 0.6, respectively. The detailed implementation of the automatic node creation procedure is described in Algorithm II as follows:

Algorithm Π MeshRefinement (P, T, alpha, beta)

- 1. Let $P = \{p_k, k = 1, \dots, n\}$, be the set of nodes on the boundaries of domain that are stored in sequence of counter-clockwise direction for outside boundaries and clockwise direction for inside boundaries. Let V be the empty set of newly inserted nodes and let T be the set of Delaunay triangles which are constructed by Algorithm I.
 - 2. Compute the point distribution function dp_i for each boundary nodes p_i by

$$dp_i = \frac{1}{M} \sum_{j=1}^{M} ||p_j - p_i||.$$
 (14)

- 3. Read triangle t_i from T. Define the centroid of the triangle t_i as node Q, then compute the point distribution function of node Q using Eq. (14). Compute the distance d_m , m = 1, 2, 3, from node Q to each of the three vertices of the triangle t_i .
 - 4. Perform the Alpha and Beta tests for node Q.

If $d_m < (\alpha \cdot dp_q)$ for any m = 1, 2, 3, then reject the node Q and return to Step 3; otherwise compute the distance s_j for any $j = 1, \dots, N$ from node Q, that is to be inserted, to the other nodes.

If $s_j < (\beta \cdot dp_q)$ for any $j = 1, \dots, N$, then reject the node Q and go to Step 3; otherwise accept the node Q for insertion by the Delaunay triangulation algorithm (Algorithm I) and add node Q and V.

- 5. Repeat Step 3 and 4 until all triangles in T are considered.
- 6. Perform the Delaunay triangulation for the derived nodes in V by Algorithm 1.

The shapes and sizes of triangles formed from the previous step can be improved by applying a mesh smoothing technique such as the Laplacian smoothing technique^[30]. The basic idea of a new node insertion at the centroid of triangle is depicted in Fig. 3. A demonstration of a domain refinement by creating a new node inside the domain using Algorithms I and II is shown in Fig. 4. The new node that conforms to both the Alpha and Beta testing criteria is inserted at the centroid of the triangle and applied the in-circle testing criterion to all neighborhood triangles.

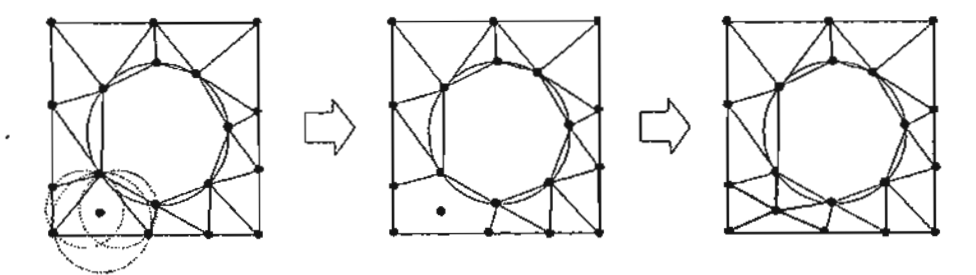


Fig. 3 Mesh refinement with automatic point creation scheme (Algorithm II)

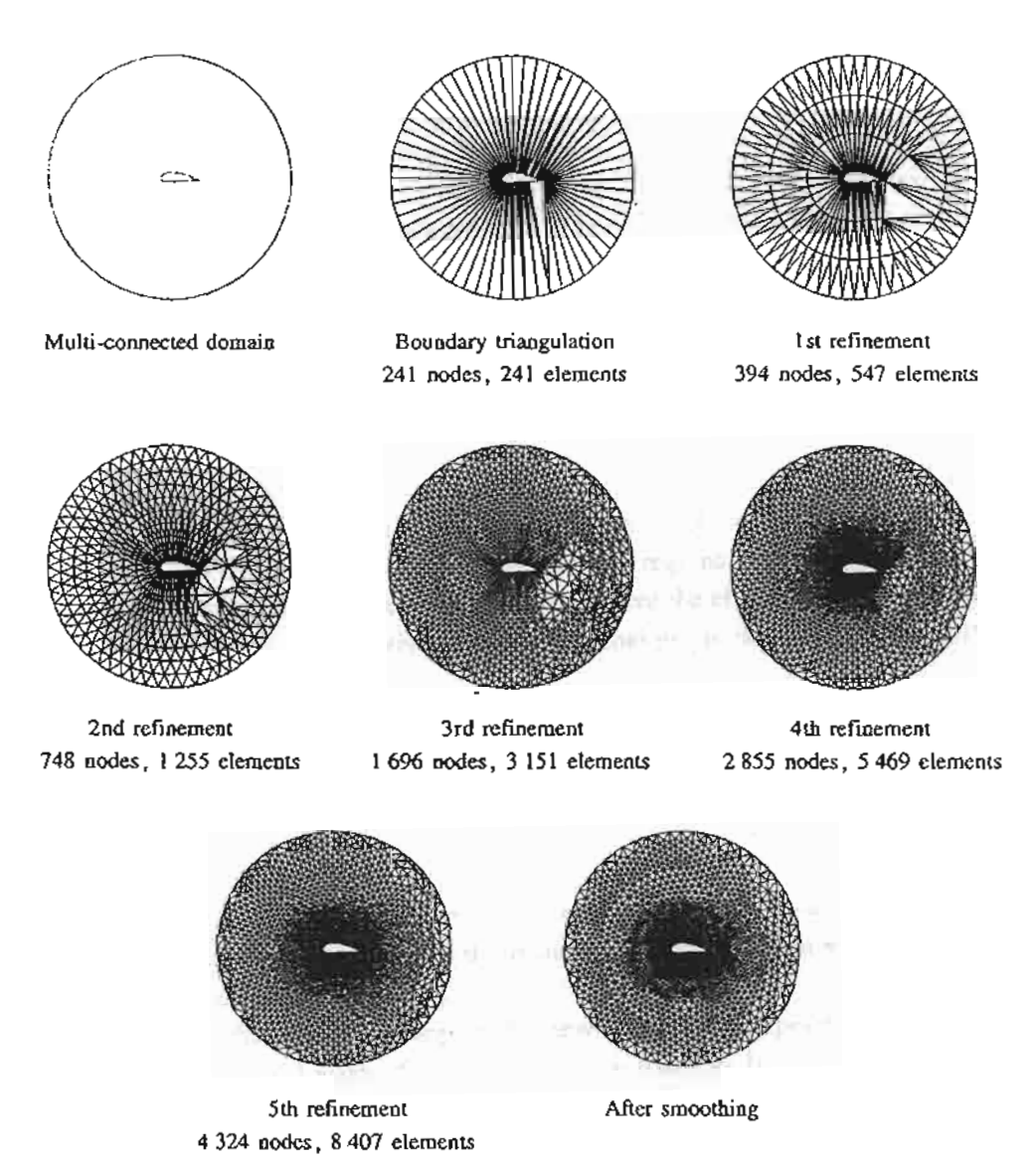


Fig. 4 Mesh refinement and smoothing for computational domain of an airfoil

Adaptive Remeshing Technique

3.1 Element size determination

In high-speed compressible flows, flow properties, such as the density and pressure, change abruptly across the shock waves. Small elements are thus needed along the shock waves to capture a good resolution shock wave. The second derivatives of any key variables ϕ , such as density, in the principal directions x and y where the cross-derivatives vanish^[17] are used as the indicator for the placement of small elements in the region where changes in the density gradients are large. The proper element size h_i is computed by requiring that the error should be uniform for all elements,

$$h_i^2 \lambda_i = h_{\min}^2 \lambda_{\max} = \text{const}, \tag{15}$$

where λ_i is the higher principal quantity of the element considered,

$$\lambda_i = \max\left(\left|\frac{\partial^2 \phi}{\partial x^2}\right|, \left|\frac{\partial^2 \phi}{\partial y^2}\right|\right). \tag{16}$$

In the above Eq. (15), λ_{max} is the maximum principal quantity for all elements and h_{min} is the minimum element size specified by users. The regions, which will be refined or coarsened by AdaptiveRemeshing algorithm below, are identified by a dimensionless error indicator, the pressure-switch coefficient^[16] as

$$E_{I} = C_{v} \sum_{f \in I} |2\phi_{f} - \phi_{f} - \phi_{g}| / \sum_{e \in I} (|\phi_{f} - \phi_{f}| + |\phi_{f} - \phi_{g}|), \qquad (17)$$

where C_{ν} is the constant equal to 1 for this paper.

3.2 Adaptive mesh generation

The proposed adaptive mesh regeneration is based on the concepts of the Delaunay triangulation and the mesh refinement as described by Algorithms I and II. The new mesh is constructed using the information from the previous mesh or background mesh, such that the new mesh are composed of small elements in the regions with large changes of solution gradients, and large elements in the other regions where the changes of solution gradients are small. Detailed process of adaptive remeshing technique is described in Algorithm III as follows.

Algorithm III AdaptiveRemeshing (P, T, alpha, beta, h_{min}, h_{max})

- 1. Let $P = \{p_k, k = 1, \dots, n\}$ be the set of nodes of the background mesh. Let $T = \{t_l, l = 1, \dots, m\}$ be the set of triangles of the background mesh.
 - 2. Let N_P be the empty set of nodes and N_T be the empty set of triangles.
- 3. Calculate the new proper element size h_i of all the nodes of the background mesh by Eqs. (15) and (16). Then rediscretize all boundaries of the domain based on the new proper elements size h_i and recompute the point distribution function dp_i for all the boundary nodes before adding all nodes into N_p .
- 4. Obtain nodal solution values of the new mesh by interpolating the nodal solution values of the background mesh. Construct boundary triangles from the new boundary nodes in N_P by Algorithm I and store all the new triangles into N_T .
- 5. Refine the boundary triangles based on the given values of the Alpha and Beta coefficients by Algorithm II and store all new inserted nodes into N_p .
 - 6. Read next interior node p_i of the background mesh from P.
- 7. Search triangle t_i in N_T which contains the node p_i using the method described in Step 3 of Algorithm I. Then calculate the centroid of the triangle t_i and define it as node Q, and compute the point distribution function of node Q by Eq. (14).
- 8. Compute the distance d_m , m = 1,2,3 from node Q to each of the three vertices of the triangle t_i .
 - 9. If h_i > average of d_m for m = 1,2,3 then go to Step 6.
 - 10. Compute the X_i coefficient, χ_i , for each boundary nodes p_i by

$$\chi_i = \text{ScaleRange}\left(\frac{h_{\text{mex}} - dp_i}{h_{\text{max}} - h_{\text{min}}}, 0, 1, \chi_{\text{min}}, \chi_{\text{max}}\right), \tag{18}$$

where ScaleRange() is the scale range function which scales the 0-1 range to the new

range $\chi_{min} - \chi_{max}$.

11. Perform the χ_i test for node Q.

If two out of three of $d_m < (\chi_* \cdot h_{\min})$ for any m = 1, 2, 3, then reject the node Q and return to Step 6; otherwise compute the average distance, $s = (d_1 + d_2 + d_3)/3$.

- If $s < (\chi_i \cdot dp_a)$ or $h_i < h_{min}$ then reject the node Q and go to Step 6.
- 12. Accept the node Q for insertion by the Delaunay triangulation algorithm (Algorithm 1) and add node Q into N_p .
 - 13. Repeat Steps 6 to 12 until all nodes in P are considered.
- 14. Perform the Delaunay triangulation of the inserted nodes in N_P by Algorithm I and smooth the mesh.

The coefficient χ_i controls the node insertion in the regions of high solution gradient and ensure undue distortion of the regularity of the triangulation. The value of χ_{min} limits number of nodes insertion in high gradient region such as shock, while the value of upper limit χ_{max} allows more nodes to be inserted into the lesser solution gradient such as tails of expansion fan. Practical experience with this described procedure for high-speed compressible flow problems suggest the values of χ_{min} and χ_{max} as 0.5 and 0.7, respectively.

4 Algorithm Evaluation

To demonstrate the capability of the adaptive remeshing technique with the Delaunay triangulation for increasing the flow solution accuracy, five simulations of both steady-state and transient high-speed compressible flows are evaluated. The two examples of steady flow and three examples of transient flow are (1) Mach 15.3 flow past a cylinder, (2) Mach 3 flow past a 15 degrees wedge, (3) Sod shock tube, (4) Mach 2 shock reflection over a circular arc surface, and (5) shock wave propagation from underwater explosions.

4.1 Mach 15.3 flow past a cylinder

The problem statement of a steady-state Mach 15.3 flow past a cylinder^{8} is described in Fig. 5. There is a detached bow shock in front of the cylinder with subsonic flow region near the centerline between the bow shock and the cylinder. Away from this region, the flow

behind the weaker part of the bow shock becomes supersonic with steep variation of all flow variables. Figure 6 shows the final adaptive mesh consisting of $18\,537$ nodes and $36\,986$ elements, as well as the resulting density, pressure and Mach number contours. With this mesh, good flow resolution quality including sharp bow shock is obtained as shown in Figs. 6(b) - 6(d). The convergence history of the final adaptive mesh represented by the volume-weighted error E measurement $^{[31]}$ is shown in Fig. 7. The error reduced about three orders of magnitude after 2 500 iterations.

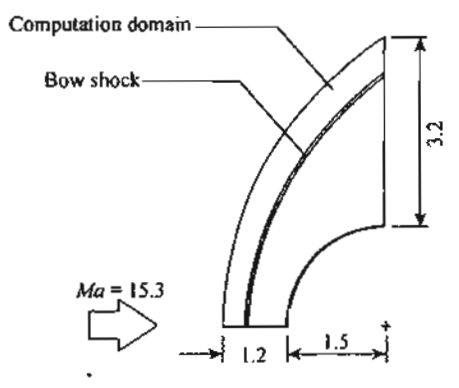
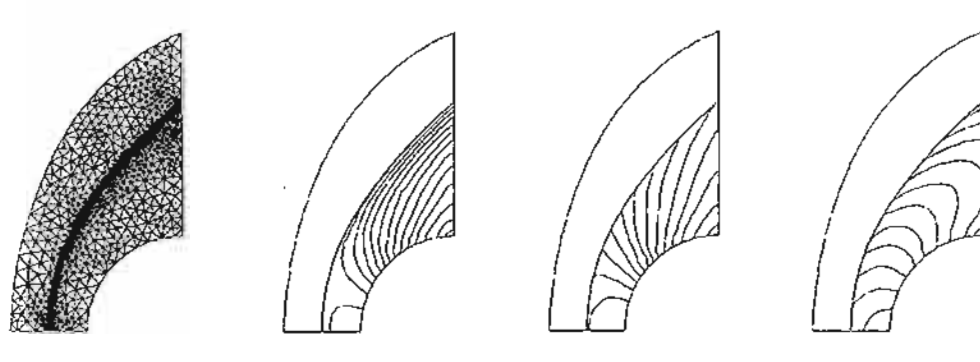


Fig. 5 Problem statement of a Mach 15.3 flow past a cylinder



(a) Final adaptive mesh

(b) Density contours

(c) Pressure contours Fig. 6 Mach 15.3 flow past a cylinder

(d) Mach number contours

4.2 Mach 3 flow past a 15 degrees wedge

The problem statement of a Mach 3 flow past a 15 degrees wedge on the domain 1.5 x 1.0 is presented in Fig. 8. The flow enters the left boundary of the computational domain and creates an oblique shock wave. The final adaptive mesh consists of 10 543 nodes and 21 013 elements, and the corresponding density contours of the problem are shown in Figs. 9(a) - 9(b), respectively. Small clustered elements along the shock line are generated from the error indicator given by Eq. (15) and the adaptive remeshing algorithm described. Figures 10(a) - 10(b) show the predicted density and Mach number solution of the final adaptive mesh along section A-A compared to the exact solutions^[1]. The figures indicate good solution accuracy obtained from the combined adaptive remeshing technique and higher-order accurate scheme.

4.3 Sod Shock tube

The one-dimensional shock tube test case, the so called Sod shock tube^[32], is solved by using a two-dimensional domain. The initial conditions of the fluids on the left and right sides are given by $(\rho, u, p)_L = (1.0, 0.0, 1.0)$ and $(\rho, u, p)_R = (0.125, 0.0, 0.1)$. The 1.0×0.1 computational domain is divided into 400 and 40 equal intervals in the x and y directions, respectively. The domain is discretized with uniform triangular elements. Figures 11(a) - 11(f) show the computed density, pressure and u-velocity distributions along the tube length which are compared with the exact solutions at time t = 0.15. The figures show that the higher-order extension of Roe's scheme with the mixed entropy fix method provides more accurate solutions than its first-order solutions.

Mach 2 shock reflection over a circular arc surface

The computational domain for a Mach 2 shock reflection over a circular arc surface is illustrated in Fig. 12. Figure 13 shows series of the transient adaptive meshes and the corresponding computed density contours at different time instants. The transient adaptive meshes consist of approximately 16 000 elements in the early time before the normal shock reaches the circular arc surface, and are increased to approximately 18 000 elements at bottom right image of Fig. 13. The figures highlight the detailed flow solution that could be captured by using the combined adaptive mesh algorithm and the higher-order flux-difference splitting scheme with the H-correction entropy fix method.

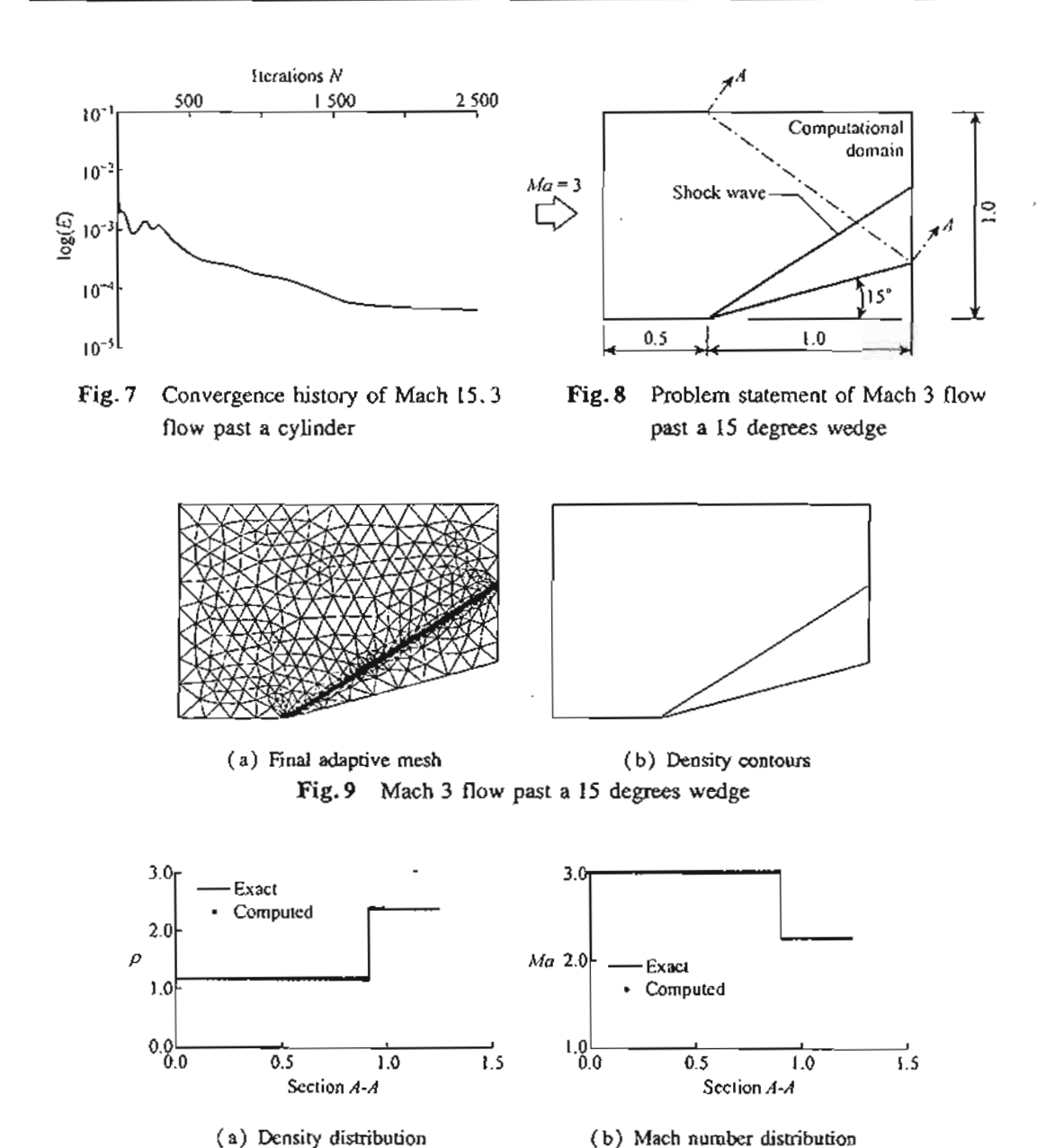


Fig. 10 Comparative Mach number distributions between the exact and computed solutions along section A-A for Mach 3 flow past a 15 degrees wedge

4.5 Shock wave propagation from underwater explosions

To further evaluate the efficiency of the combined adaptive Delaunay triangulation and the cell-centered upwinding algorithm, the shock wave propagation from an underwater explosion is studied. Figure 14 shows the problem statement describing the dimensions of the computational domain in meters and the shock wave phenomenon generated from the initial pressure of 12 GPa at the center of explosion. The figure also shows the location of mine

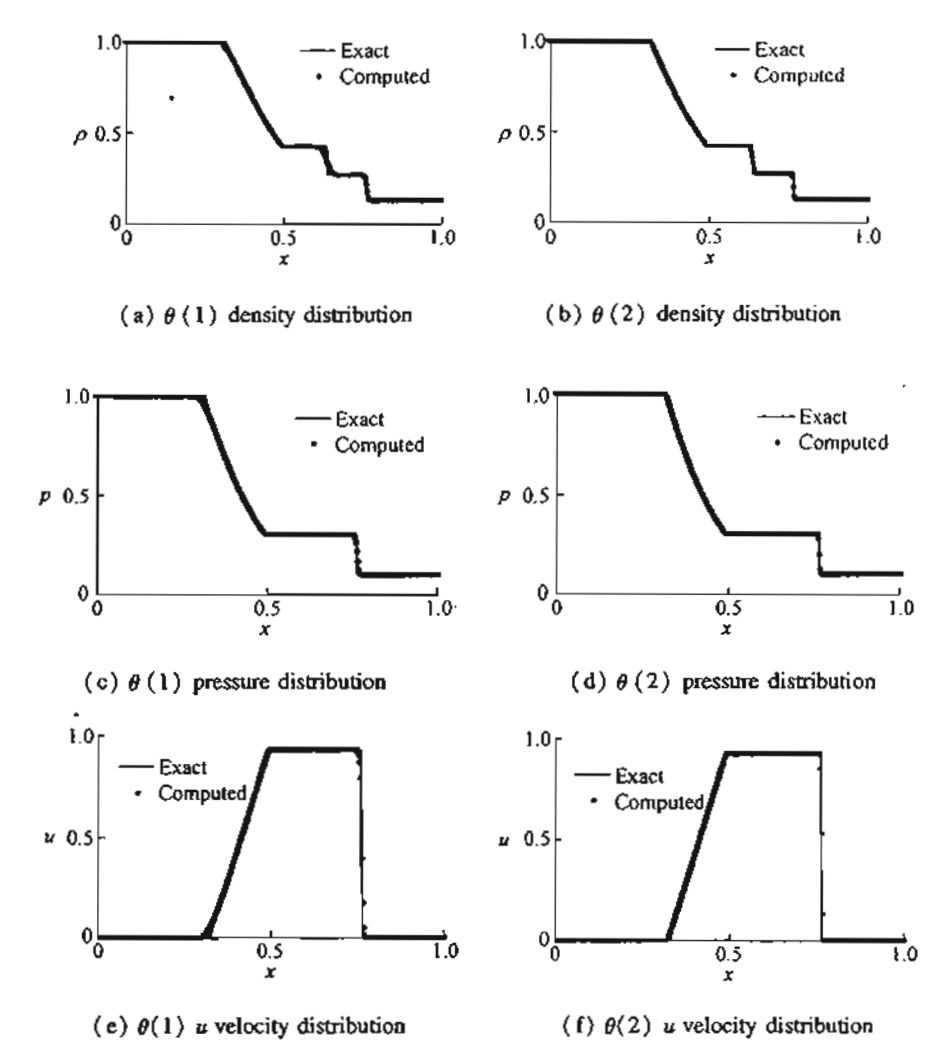


Fig. 11 Comparative computed and exact solutions at time t = 0.15 for Sod shock tube

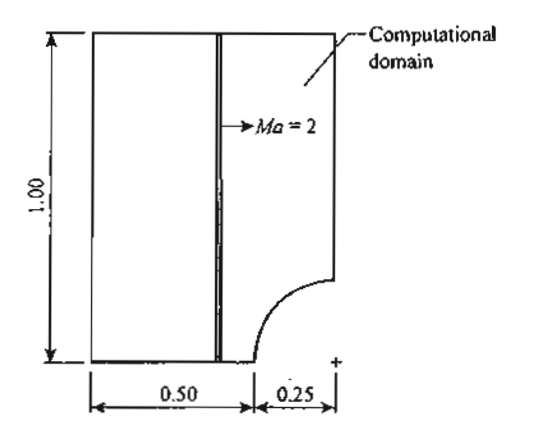


Fig. 12 Problem statement of Mach 2 shock reflection over a circular arc surface

which is at the front of the ship length and at 10 meters depth from water surface. Figure 15 shows series of the transient adaptive meshes and the corresponding predicted pressure contours at different times as the half-circular shock propagates from the center of explosion. Small elements are generated to capture the half-circular shock wave accurately, while larger elements are generated in other regions to minimize the total number of unknowns and the computational time. This half-circular shock wave reaches the ship hull at around time $t=5\,\mathrm{ms}$.

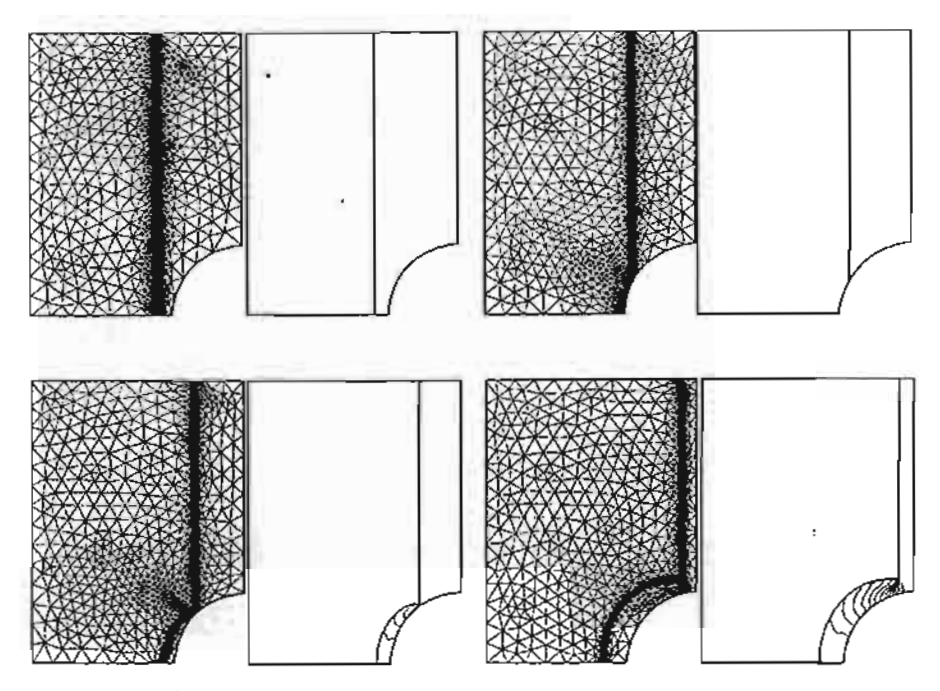


Fig. 13 Transient adaptive meshes and the computed density contours of Mach 2 shock reflection over a circular arc surface at four different stages of the computation

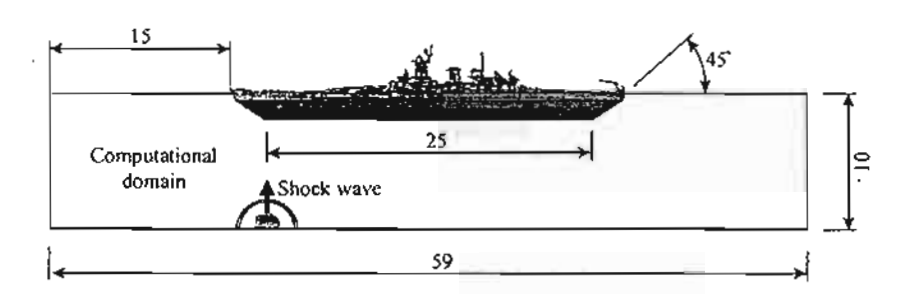


Fig. 14 Problem statement of shock wave propagation from an underwater explosion

5 Conclusions

The combined adaptive Delaunay triangulation and the cell-centered upwinding algorithm for the analysis of steady-state and transient inviscid high-speed compressible flows was presented. The cell-centered upwinding algorithm for solving the Euler equations was described first. The multidimensional dissipation scheme was developed for unstructured triangular meshes and included into the algorithm. The concept of the Delaunay triangulation for two-dimensional mesh construction was then explained. The mesh generation procedure with automatic point creation and mesh smoothing were described. The solution accuracy was further improved by incorporating an adaptive remeshing technique to the Delaunay triangulation algorithm and analyzing with higher-order Roe's flux difference splitting

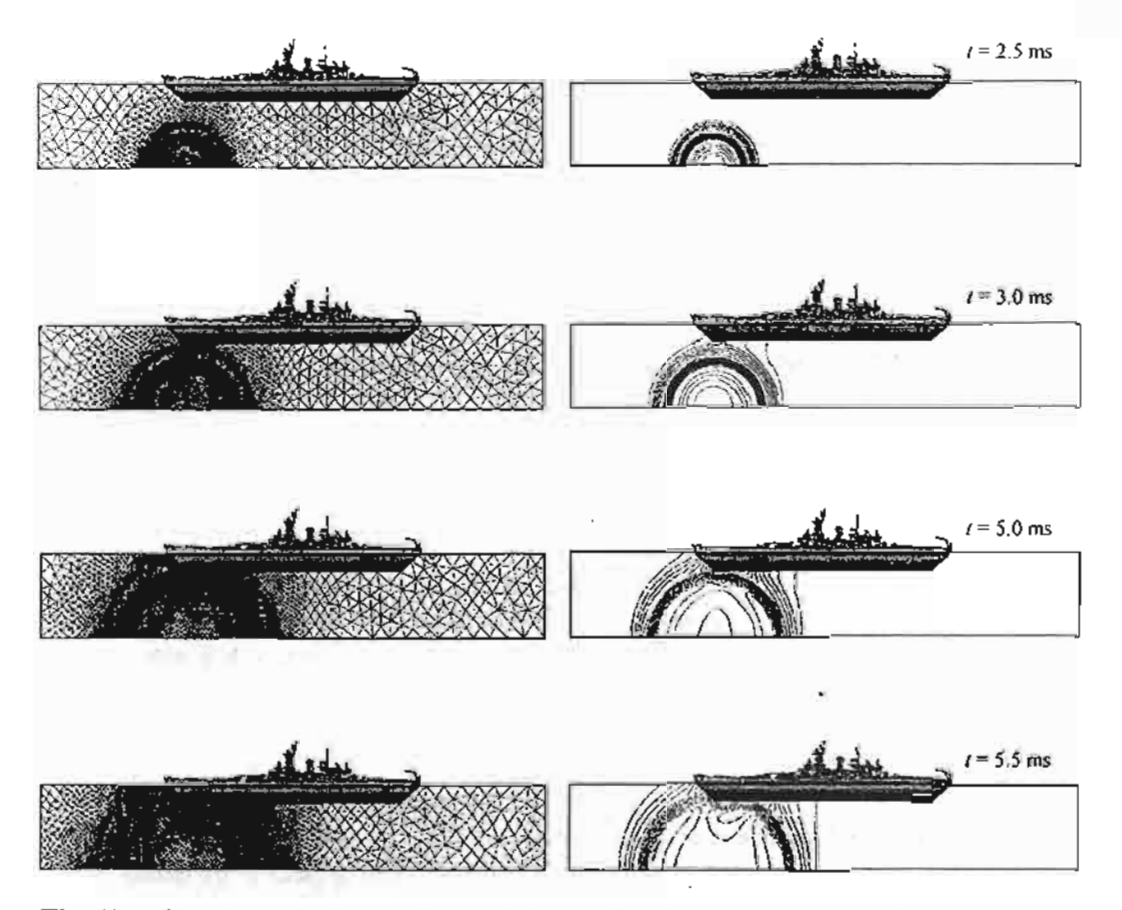


Fig. 15 Transient adaptive meshes and the predicted pressure contours for shock wave propagation from an underwater explosion

scheme. The adaptive remeshing technique places small elements around regions with large changes of flow solution gradients, at the same time larger elements are generated in other regions.

The results of the combined method shows the shock waves can be captured with high solution accuracy. These examples show that the adaptive Delaunay triangulation and the cell-centered algorithm increase the analysis solution accuracy, and at the same time, significantly reduce the total number of unknowns and the computational time for both the steady and unsteady compressible flow problems.

Acknowledgement The authors are pleased to acknowledge the Thailand Research Fund (TRF) and the Royal Thai Navy for supporting this research.

References:

- [1] Anderson J.D. Modern Compressible Flow with Historical Prospective [M]. 2nd edition. McGraw-Hill, New York, 1990.
- [2] Donea J. A Taylor-Galerkin method for convective transport problems[J]. Internat J Numer

- Methods in Engng, 1984, 20(1):101-119.
- [3] Huges T J R. Recent Progress in the Development and Understanding of SUPG Methods with Special Reference to the Compressible Euler and Navier-Stokes Methods in Fluids [M]. John Wiley, New York, 1987, 1261 1275.
- [4] Jiang B N, Carey G F. A stable last-squares finite element method for non-linear hyperbolic problems [J]. Internat J Numer Methods in Fluids, 1988, 8(9):933-942.
- [5] Gnoffo P A. Application of program LUARA to three-dimensional AOTV flow fields [R].
 AIAA Paper 86-0565, 1986.
- [6] Roe P L. Approximate Riemann solvers, parameter vectors, and difference schemes [J]. J Comput Phys, 1981, 43(2):357-372.
- [7] Quirk J J. A contribution to the great Riemann solver debate [J]. Internat J Numer Methods in Fluids, 1994, 18(6):555-574.
- [8] Sanders R, Morano E, Druguet M C. Multidimensional dissipation for upwind schemes: stability and applications to gas dynamics [J]. J Comput Phys, 1998, 145(2):511-537.
- [9] Bowyer A. Computing Dirichlet tessellations [1]. Comput J, 1981, 24(2):162 166.
- [10] Watson D F. Computing the *n*-dimensional Delaunay tessellation with application to Voronoi polytopes [J]. Comput J, 1981, 24(2):167-172.
- [11] Weatherill N P, Hassan O. Efficient three-dimension Delaunay triangulation with automatic point creation and imposed boundary constraints [J]. Internat J Numer Methods in Engng, 1994,37(12):2005-2039.
- [12] Karamete B K, Tokdemir T, Ger M. Unstructured grid generation and a simple triangulation algorithm for arbitrary 2-D mometries using object oriented programming [J]. Internat J Numer Methods in Engag, 1997, 40(2):251-268.
- [13] Peraire J, Vahdati M, Morgan K, Zienkiewicz O C. Adaptive remeshing for compressible flow computations [J]. J Comput Phys, 1987, 72(2):449-466.
- [14] Berger M J, Colella P. Local adaptive mesh refinement for shock hydrodynamics [J]. J Comput Phys, 1989, 82(1):67-84.
- [15] Jin H, Wiberg N E. Two-dimensional mesh generation, adaptive remeshing and refinement
 [J]. Internat J Numer Methods in Engng, 1990, 29(7):1501-1526.
- [16] Probert J, Hassan O, Peraire J, Morgan K. An adaptive finite element method for transient compressible flows [1]. Internat J Numer Methods in Engng, 1991, 32(5):1145-1159.
- [17] Dechaumphai P, Morgan K. Transient thermal-structural analysis using adaptive unstructured remeshing and mesh movement [A]. In: Thornton E A (ed). Thermal Structures and Materials for High-Speed Flight [C]. American Institute of Aeronautics and Astronautics, Washington D C, 1992, 205 228.
- [18] Quirk J J, Hanebutte U R. A parallel adaptive mesh refinement algorithm [R]. ICASE Report 93-63,1993.
- [19] Venkatakrishnan V. A perspective on unstructured grid flow solvers [R]. AIAA paper 95-0667,1995.
- [20] Sun M, Takayama K. Conservative smoothing on an adaptive quadrilateral grid[J]. *J Comput Phys*, 1999, 150(1):143-180.
- [21] Hirsch C. Numerical Computation of Internal and External Flows[M]. Vol 2. John Wiley & Sons, New York, 1998.
- [22] Shyue K M. An efficient shock-capturing algorithm for compressible multicomponent problems[J]. J Comput Phys, 1998, 142(1):208-242.

- [23] Harten A. High resolution schemes for hyperbolic conservation laws [J]. J Comput Phys., 1983,49(3):357-393.
- [24] Frink N T, Parikh P, Pirzadeh S. A fast upwind solver for the Euler equations on three-dimensional unstructured meshes [R]. AIAA Paper-91-0102; In: 29th Aerospace Sciences Meeting and Exhibit [C]. Reno, Navada, 1991.
- [25] Frink N T, Pirzadeh S Z. Tetrahedral finite-volume solutions to the Navier-Stokes equations on comlex configurations [R]. NASA/TM-1998-208961, 1998.
- [26] Vekatakrishnan V. Convergence to steady state solutions of the Euler equations on unstructured grids with limiters[J]. J Comput Phys, 1995, 118(1):120-130.
- [27] Shu C W, Osher S. Efficient implementation of essentially non-oscillatory shock-capturing schemes [J]. J Comput Phys, 1988, 77(2):439 471.
- [28] Linde T, Roe P L. Robust Eluer codes [R]. AIAA Paper-97-2098; In: 13th Computations Fluid Dynamics Conference [C]. Snowmass Village, CO, 1997.
- [29] Joe B, Simpson R B. Triangular meshes for regions of complicated shape[J]. Internat J Numer Methods in Engng, 1986, 23(5):751-778.
- [30] Frey W H. Selective refinement; a new strategy for automatic node placement in graded triangular meshes [J]. Internat J Numer Methods in Engng, 1987, 24(11):2183-2200.
- [31] Sun M, Takayama K. Error localization in solution-adaptive grid methods [J]. J Comput Phys, 2003, 190(1):346-350.
- [32] Sod G A. A survey of several finite difference methods for systems of nonlinear hyperbolic conservation laws [J]. J Comput Phys, 1978, 27(1):1-31.

บทความทางวิชาการ เรื่อง

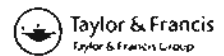
Comparative Study of Flux-limiters Based on MUST Differencing Scheme

Published in the

International Journal of Computational Fluid Dynamics

Vol. 18, No. 7, pp. 569-576

2004



Comparative Study of Flux-limiters Based on MUST Differencing Scheme

V. JUNTASAROa,* and A.J. MARQUISh,*

*Department of Mechanical Engineering, Faculty of Engineering, Computational Mechanics Laboratory (CML), Kasetsart University, Bangkhen, Bangkok 10900. Thailand: *Department of Mechanical Engineering, Imperial College of Science, Technology and Medicines, London, England, UK

(Received September 2002; In final form 5 May 2004)

A comparative study of a number of flux-limiters based on MUST methodology is presented in this paper to find the most suitable flux-limiter to be used in unsteady and steady convective flow calculations. The accuracy and convergence behaviour of these flux-limiters are assessed in five pure convection problems: (1) rotation of a cone-shaped scalar field, (2) advection of a square-shaped scalar field, (3) mixing of a hot with a cold front, (4) deformation of cone-shaped scalar field and (5) IAHR. The superbee flux-limiter results in the most accurate solutions in unsteady flow problems, and the Koren flux-limiter is the more appropriate in steady flow problems because of its good convergence behaviour.

Keywords: Differencing scheme; Flux-limiter; Convective flow; Steady flow; Unsteady flow; Unstructured mesh

INTRODUCTION

At present, convective terms in the governing equations can be discretised using various differencing schemes such as central differencing (CD), first-order upwind (FOU) and second-order upwind (SOU) differencing schemes. The solutions obtained using FOU appear to be more physically realistic than those using CD (i.e. the solutions are always bounded), although the results are diffusive; while SOU gives more accurate results than FOU, the results are unbounded. Thus, a non-linear function called a flux limiter was initially introduced by van Leer (1973, 1974) to prevent the appearance of overor undershoots of the computed solutions. Several SOU schemes incorporated via a flux limiter, called secondorder limited upwind (SOLU) schemes, were used successfully with structured grids. However, these schemes are still under development in the case of unstructured grids.

Tamamidis (1995) proposed a second-order fully upwind triangular-based differencing scheme with a flux limiter called monotonic upwind scheme for triangles (MUST) which is monotonic and accurate up to second order. MUST is different from the other triangular-based differencing schemes in that it uses a different approach in

The present work is therefore to compare accuracy and convergence behaviour of the results from five different flux-limiters: minmod, superbee, van leer, MUSCL and Koren based on MUST methodology on five pure convection test cases, to improve the understanding of differencing schemes for convection terms, and to find the most suitable flux-limiter to be used in unsteady and steady convective flow calculations.

CALCULATION METHODS

Governing Equations for 2D Pure Convection Flow

The following pure convection equation is considered in order to examine the performance of MUST in discretising convective term

$$\frac{\partial \phi}{\partial t} + \nabla \cdot \mathbf{f}(\phi) = 0 \tag{1}$$

calculating the gradient at the cell centre. In MUST, the cell-centered gradient is calculated using differences in the upwind direction of the considered node in order to ensure that the scheme is fully upwind. The results using MUST were found to be very good although only a simple flux limiter minmod was used.

^{*}Corresponding author, E-mail: fengvrj@ku.ac.th

E-mail: a.marquis@ic.ac.uk

where ϕ is a scalar function of two space dimensions and time

$$\mathbf{f}(\phi) = \begin{pmatrix} U \\ V \end{pmatrix} \phi,$$

where U and V are the two components of the velocity vector.

Discretisation Methods

Monotonic Upwind Scheme for Triangles (MUST)

Equation (1) is a governing equation representing a form of conservation law. It is integrated over the flow domain using Green's formula, assuming uniform values of ϕ over the cell faces. The semi-discrete form of the equation considered can be written as

$$A_i \frac{\partial \phi_i}{\partial t} = -\sum F_i^{jk} = R_i \tag{2}$$

where P_i^{jk} is the numerical flux through an edge jk of each cell i. The equation is then solved using an explicit fourth-order accurate Runge-Kutta time marching scheme (Jameson et al., 1981).

Using Roe's flux-difference splitting (Roe, 1981), the flux across an edge jk for unstructured grids can be obtained as

$$F^{jk} = \frac{1}{2} \left[F(\phi_L) + F(\phi_R) - |\alpha^{jk}| (\phi_R - \phi_L) \right]$$
 (3)

where α is the scaled characteristic speed defined as $\alpha = (\partial F/\partial \phi)$ and equal to U (the normal velocity to the cell face multiplied by the edge length) in the pure convective problems considered in this work.

The key point in achieving higher-order accuracy is the method to find the left and right values (ϕ_L and ϕ_R) in Eq. (3). Frink (1992) used Taylor series to obtain a second-order scheme by expanding the cell-centered solution to each cell face

$$\phi(x, y) = \phi(x_c, y_c) + \nabla \phi_c \cdot \Delta r + O(\Delta r^2), \tag{4}$$

where the subscript c denotes the cell-centered value. The gradient of ϕ is required at the cell centers for the above formulation.

Tamamidis (1995) proposed an approach in calculating the gradient at cell center to ensure that the scheme is fully upwind by using differences in the upwind direction. Following the notation of Fig. 1(a), in order to calculate the flux through the face 12 in triangle A, the second term in Eq. (4) is written in the finite-difference format as

$$\nabla \phi_A^- \cdot \Delta \mathbf{r}_{Af} = \left(\frac{\phi_A - \phi_3}{x_A - x_3}\right) (x_f - x_A) + \left(\frac{\phi_A - \phi_3}{y_A - y_3}\right) (y_f - y_A)$$
 (5)

where f is the mid-point on the face 12, and ϕ_3 can be calculated based on a reconstruction procedure, i.e. the cell-centered values are used to evaluate the vertex values.

Identifying the nodes in the upstream and downstream directions as in Fig. 1(b), the left and right values of ϕ on a cell face can be calculated as

$$\phi_{L} = \phi_{u_{1}} + \frac{1}{2} \psi(r) \left(\frac{\Delta \phi_{u_{1}u_{2}}}{\Delta x_{u_{1}u_{2}}} \Delta x_{fu_{1}} + \frac{\Delta \phi_{u_{1}u_{2}}}{\Delta y_{u_{1}u_{2}}} \Delta y_{fu_{1}} \right), \quad (6)$$

$$\phi_{R} = \phi_{d_{1}} + \frac{1}{2} \psi(r) \left(\frac{\Delta \phi_{d_{1}d_{2}}}{\Delta x_{d_{1}d_{2}}} \Delta x_{fd_{1}} + \frac{\Delta \phi_{d_{1}d_{2}}}{\Delta y_{d_{1}d_{2}}} \Delta y_{fd_{1}} \right), \quad (7)$$

where $\psi(r)$ is a flux limiter. In order to maintain the sign of the higher-order terms, the flux limiter is assumed to be non-negative.

In the FOU scheme, the cell-centered values of triangles on the left and right sides of the considered face are assumed to be the left and right values of the variable of that face. According to Fig. 1(a), the left and right values of the face 12 are $\phi_L = \phi_A$ and $\phi_R = \phi_B$.

Flux Limiters

The flux limiter is introduced in the higher-order differencing scheme to prevent the unwanted oscillations

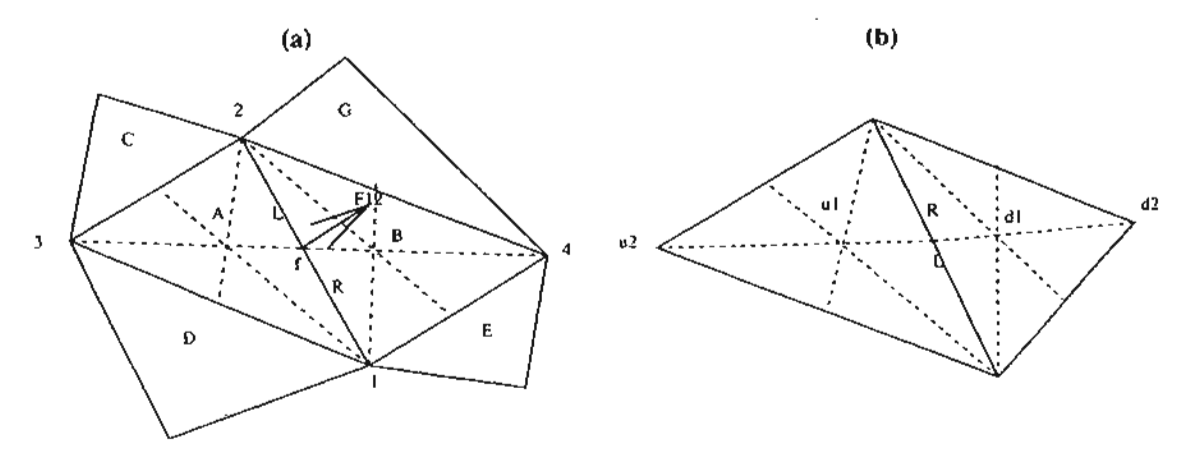
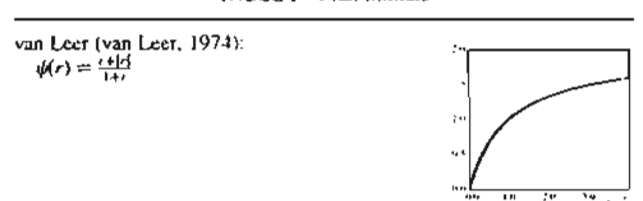
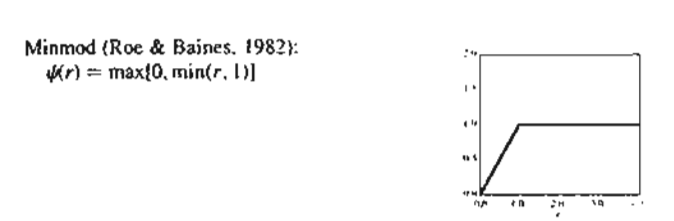
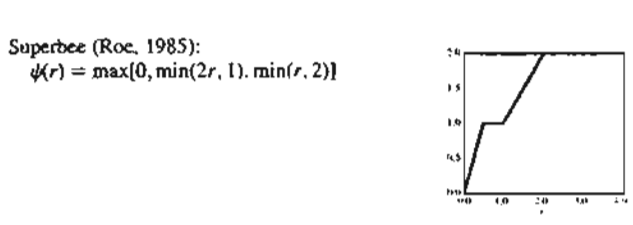


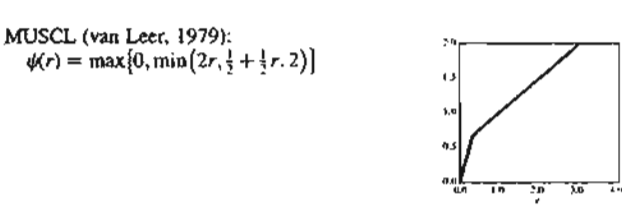
FIGURE 1 (a) Triangular mesh configuration (b) Definition of upwind and downwind nodes for MUST scheme.

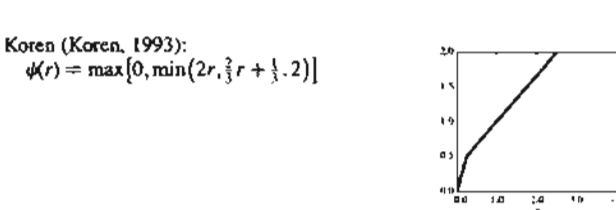
TABLE I Flux limiters











and to ensure bounded results, i.e. it is used to maintain the monotonic property of the scheme. Since the flux-limiter is assumed to be non-negative in MUST, only positive flux-limiters are considered in this work. The distribution of the considered flux limiters, ψ against consecutive gradient, r are plotted and presented in Table 1, where r is defined as

$$r = \frac{D - C}{C - U} \tag{8}$$

where D, C and U represent downstream, center and upwind values, respectively.

RESULTS AND DISCUSSION

Rotation of a Cone-shaped Scalar Field

This test case is chosen to test the ability of each differencing scheme in capturing steep gradients. A scalar "cone" field is

advected around by a steady velocity field and is defined by the initial conditions

$$\phi(x,y) = \begin{cases} 0 & \text{if } r > r_c \\ 5 \left[1 + \cos\left(\frac{r\pi}{r_c}\right)\right] & \text{if } r \le r_c \end{cases}$$

The domain is $x \ge -0.5$, $y \le 0.5$ and the cone is centered originally at $(x_0, y_0) = (0.0, 0.25)$ and the radius of the cone, $r_c = 0.1$. The distance from the cone center r is

$$r = \sqrt{(x - x_0)^2 + (y - y_0)^2}.$$
 (9)

The velocity field revolves counterclockwise about (0,0) with angular velocity $\omega = 2.0 \,\text{rad/s}$ and is given by

$$U(x,y) = -2y, (10)$$

$$V(x, y) = 2x. \tag{11}$$

A time step equal to 0.005 is used because the results using the time step ≤ 0.005 are not different. It can be seen from Fig. 2(a) that the MUST methodology results in less diffusive results than the FOU scheme and also the results are bounded. The steep gradients of the scalar field are very well captured by the superbee and Koren flux-limiters while the minmod scheme results in more diffusive results. This is reflected in the predicted maximum and minimum field values from each flux limiter in Table II where superbee predicts the highest and minmod predicts the lowest maximum value, respectively. The predicted minimum scalar field value is less than zero for all flux limiters except minmod. Although the predicted negative values are very small, a problem may arise in the case where the positive-definite values are important, e.g. heat transfer problem. Note that the grid-independent solutions are presented in all test cases.

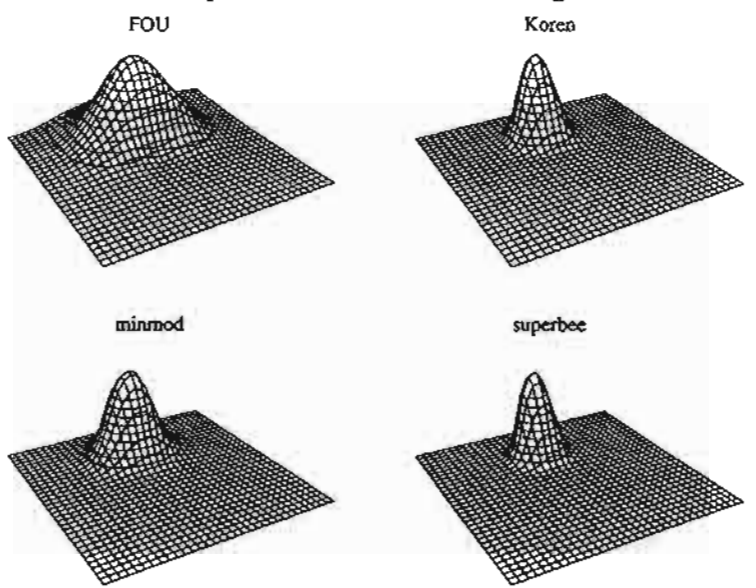
Advection of a Square-shaped Scalar Field

A square scalar field is advected by a uniform velocity field in this test case. The initial conditions are

$$\phi(x,y) = \begin{cases} 0 & \text{if } (|x+x_0|, |y-y_0|) > \frac{e}{2} \\ 10 & \text{if } (|x-x_0|, |y-y_0|) \le \frac{e}{2} \end{cases}.$$

Initially, the coordinates of the center of the square are at $(x_0, y_0) = (-1.5, -1.5)$ and the width of the square is a = 1.5. The domain of the problem is $x \ge -3$, $y \le 3$. The velocity field is steady with two velocity components equal to unity. The solutions are time-independent for $\delta t = 0.02$ and advanced for 140 time steps which correspond to the square field being advected for a length equal to 3.95 units from the initial location towards the opposite corner of the domain.

(a) The 3-D Perspective Plots of the Revolving Cone Problem



(b) The 3-D Perspective Plots of the Square Field Transport Problem

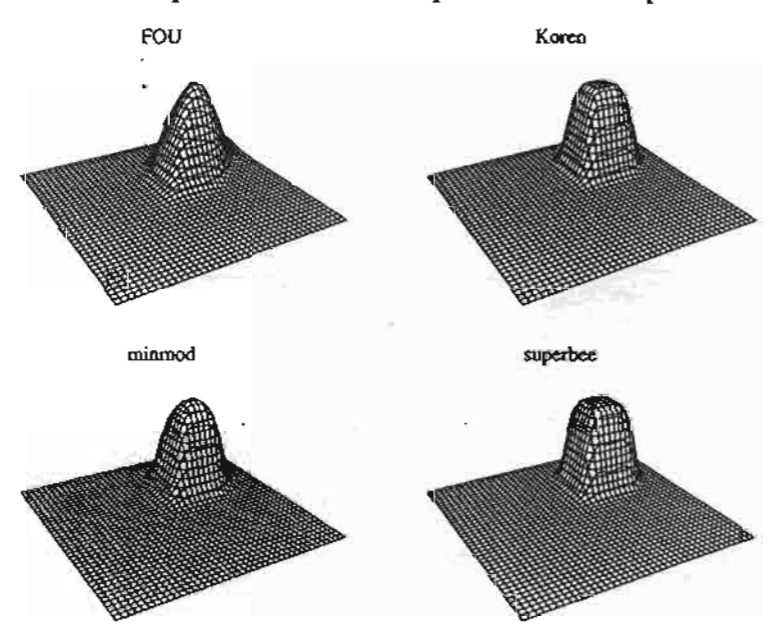


FIGURE 2 The 3-D perspective plots of the revolving cone problem and the square field transport problem.

TABLE II The maximum and minimum field values of each test case

Grid nodes	Test case 3.1 (64 × 64)		Test case 3.2 (80 × 80)		Test case 3.3 (64 \times 64)	Test case 3.4 (100 × 100)	
	Max	Min	Max	Min	L (×10 ⁻⁴)	Max	Min
FOU SOLU;	1.44	6.11×10^{-t7}	9.63	0.00	11.10	1.62	0.00
van Leer	5.74	-2.26×10^{-14}	9.93	-1.65×10^{-12}	4.53	1.88	-2.58×10^{-16}
Minmod	4.07	7.09×10^{-28}	9.92	0.00	6.04	1,77	0.00
Superbee	8.17	-4.54×10^{-6}	9.95	$\sim 1.40 \times 10^{-5}$	2.72	2.10	-6.11×10^{-7}
MUSCL	6.58	-9.70×10^{-7}	9.94	-3.93×10^{-6}	3.77	1.96	-2.84×10^{-7}
Koren	6.79	-6.06×10^{-7}	9.94	-2.69×10^{-6}	3.77	1.94	-1.05×10^{-7}

The predictions of the maximum ϕ value of the flow field using various flux limiters are not very different, however, the ability of the schemes in capturing the discontinuities can be observed from the 3-D perspective plots of the solutions with the *superbee* limiter giving the best performance in this case, as clearly shown in Fig. 2(b).

Mixing of a Hot with a Cold Front

In this test case, a rectangular domain has an initial profile of a narrow region of high gradient from top to bottom called a "front" which is then twisted by a steady rotational velocity field in a manner similar to that observed on daily weather maps (Doswell, 1984). The initial conditions are defined at t = 0 by

$$\phi(x,y) = -\tanh\left[\frac{y}{2}\cos\left(ft\right) - \frac{x}{2}\sin\left(ft\right)\right]. \tag{12}$$

The domain is $x \ge -4$, $y \le 4$ and

$$f = \frac{1}{r} \frac{f_t}{f_t},\tag{13}$$

where f is the frequency, r is the distance from the origin of the coordinate system, $f_t = (1/\cosh^2(r))\tanh(r)$ is the tangential velocity around the centre, and $f_{t_{max}} = 0.385$ is the maximum tangential velocity.

The expression of the steady velocity field is

$$U(x,y) = -\frac{y}{r} \frac{f_0}{f_{\text{box}}}, \tag{14}$$

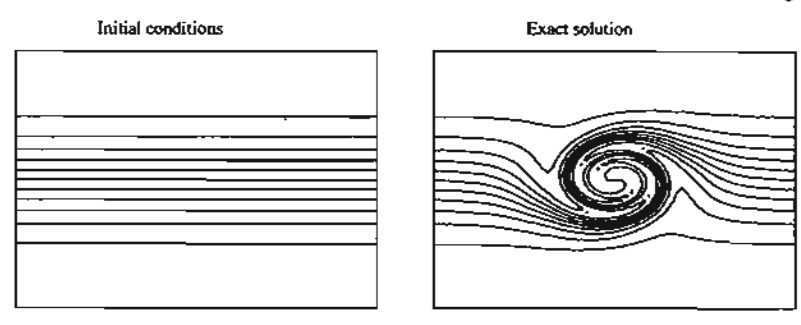
$$V(x,y) = -\frac{x}{r} \frac{f_{\rm t}}{f_{\rm least}}.$$
 (15)

The initial profile of the scalar field changes gradually from positive values at the bottom boundary to negative values at the top boundary. The solutions presented are after the front has twisted for four time units or 400 time steps. Since no scheme introduces oscillation in the solutions in this test problem, the maximum and minimum ϕ values of the flow field are not reported. However,

$$||L|| = (\sqrt{\sum |\phi - \overline{\phi_{\text{exact}}}|^2}/nx \times ny)$$

of 64 × 64 grid are tabulated in Table II to show the relative accuracy of the results using various flux limiters,

(a) Contour Plots of the Initial Conditions and Exact Solutions of the Mixing Test



(b) Contour Plots of the Numerical Solutions of the Mixing Test

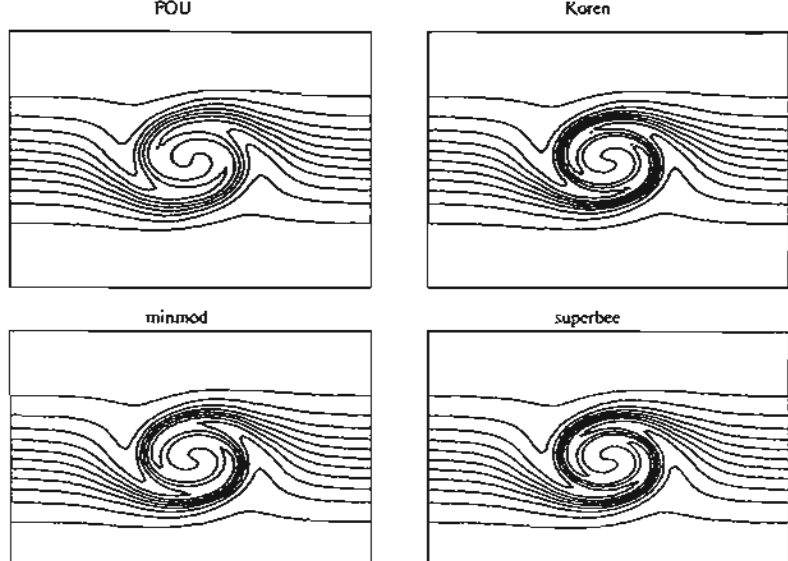


FIGURE 3 Contour plots of the mixing test.

and contour plots of 64×64 grid are presented in Fig. 3(b). The exact analytical solutions and initial conditions are also plotted in Fig. 3(a) for comparison. ||L|| from superbee is the lowest indicating that it is the most accurate, and similarly, minmod is the least accurate flux limiter because of its highest ||L||. Moreover, the contour plot from superbee is in very good agreement with that from the exact analytical solutions.

Deformation of a Cone-shaped Scalar Field

The deformation flow problem used here was first defined by Smolarkiewicz (1982) and its exact solutions were obtained by Staniforth *et al.* (1987). It is chosen to test the performance of the schemes in highly deformational flow. The steady flow field is defined by the following stream function

$$\varphi(x,y) = \frac{1}{4\pi} \sin(4\pi x) \cos(4\pi y) \tag{16}$$

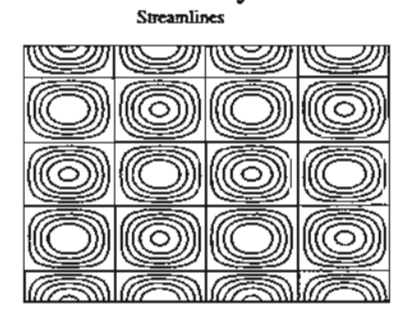
and the two velocity components are derived using $U = -(\partial \varphi/\partial y)$ and $V = (\partial \varphi/\partial x)$. Contours of the stream function and velocity vectors are shown in Fig. 4(a) and it can be seen that the velocity field is built up from sets of

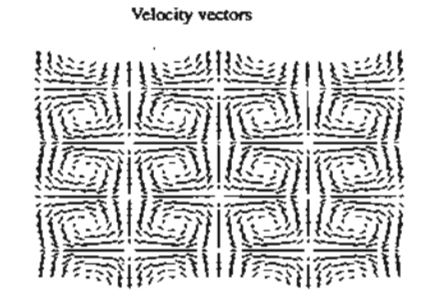
symmetrical counter-rotating vortices, each vertex occupying a square of side 25 units.

Initially, a cone of radius 15 units is centred on the centre of a square domain of side equal to one unit; the origin is specified at the bottom left-hand corner of the square. The problem has an initial condition as in test case 3.1. At t=0, the cone is in the area of six vortices but its main part is in the area of the two central ones, and then the solutions will be divided into two symmetrical parts which will move inside an area of these two central vortices. Since the fluid elements cannot cross the boundary streamline of the vortex, they cannot escape from the vortex in which they are initially located. Thus, the scalar distribution will be zero over the entire domain except over the six vortices at the centre where it is initially non-zero.

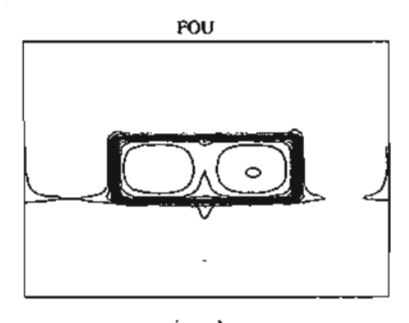
The integration time consists of 2400 time steps of 0.001 s, which produces results independent of time step. The maximum and minimum values from each scheme are reported in Table II and the isolines of the scalar distribution for various schemes are shown in Fig. 4(b). The contour plot of results obtained from the superbee flux-limiter shows the closest agreement with the exact solutions from Staniforth et al. (the exact solutions are not presented here). The predicted maximum field values are

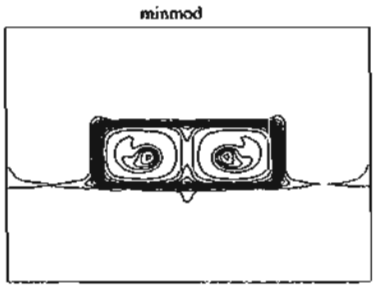
(a) Contours and Velocity Vectors of the Deformational Flow Problem

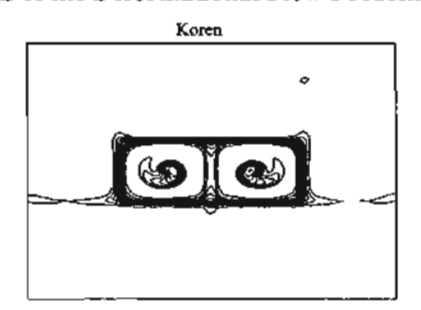




(b) Contour Plots of the Numerical Solutions of the Deformational Flow Problem







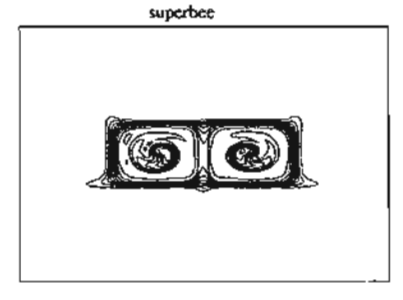


FIGURE 4 Contour plots of the deformational flow problem.

highest using superbee and lowest using minimod, as in test cases 3.1 and 3.2.

IAHR

This steady problem is used widely to test various differencing schemes and represents the convection of a step around a curved flow. The velocity field is specified as

$$U = 2y(1 - x^2) \tag{17}$$

$$V = -2x(1 - y^2) \tag{18}$$

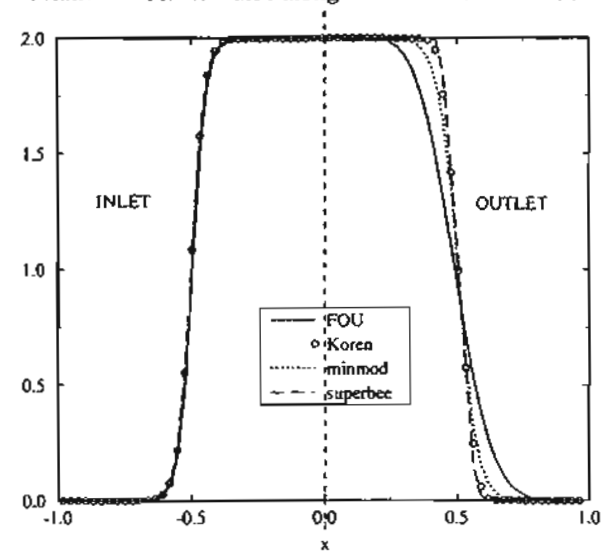
and the boundary conditions at the inlet face (for y = 0 and $-1 \le x \le 0$) as

$$\phi = 1 + \tanh[10(2x+1)]. \tag{19}$$

A zero normal gradient boundary condition is imposed at the outlet, and at the other faces of the domain, the boundary condition is specified as $\phi = 1 - \tanh(10)$. This steady-flow problem is treated as unsteady flow, and the solutions are obtained when the ϕ values reach the steady-state values, i.e. a pseudo-transient approach. A grid-independent of 71×35 mesh is used in this test case. Figure 5(a) shows the variation of ϕ values along the inlet and outlet boundaries of the domain and residuals defined as $\left(\sum (\phi^{n+1} - \phi^n)/\phi_{\max}^{n+1}\right)$ are plotted in log scale against the number of iterations per time step in Fig. 5(b).

It can be seen that *superbee* exhibits the best performance in capturing the steep gradient at the outlet boundary of the domain but shows the worst convergence behaviour, while the flux limiter that shows the best convergence behaviour is *minmod* but the solutions from *minmod* are the least accurate. Therefore,

(a) The Variation of Scalar Value along the Inlet and Outlet Boundaries



(b) Residual of Scalar Variable against the Number of Iterations

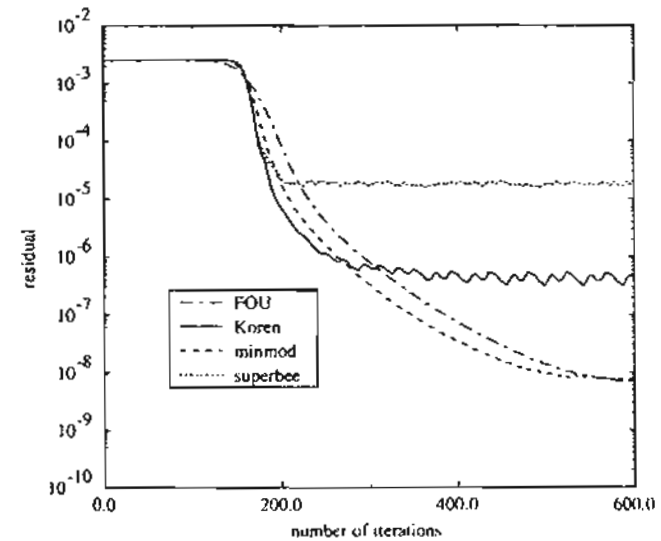


FIGURE 5 Plots of the steady-flow problem.

the compromise has to be made between accuracy and convergence. *Koren* is the most suitable in this case since its results are close to those using *superbee* and its convergence behaviour is good.

CONCLUSIONS

A comparative study of five different flux-limiters—van Leer, minmod, superbee, MUSCL, Koren—based on the MUST methodology is made using five pure convection test cases. The most accurate results are obtained using the superbee flux-limiter whereas the minmod flux-limiter causes the highest errors in the solutions for all five test cases. Therefore, the MUST methodology incorporated with superbee is the most preferable scheme for the problems with unsteady flow. However, for the steady-flow problem as test case 3.5, Koren is more appropriate than superbee because of its accurate results and good convergence behaviour. Minmod always gives the positive results unlike the other flux-limiters (Table II), indicating that minmod can be used in a wider range of applications.

Acknowledgements

This research is partially supported by the Thailand Research Fund (TRF) for the Senior Scholar Professor Pramote Dechaumphai. Special thanks are due to Professor Pramote Dechaumphai and Assistant Professor Ekachai Juntasaro.

References

- Doswell, C. (1984) "Kinematic analysis of frontogenesis associated with a nondivergent vortex", Journal of Atmospheric Sciences 41, 1242-1248.
- Frink, N. (1992) "Upwind scheme for solving the Euler equations on unstructured tetrahedral meshes", AIAA Journal 30, 70-77.
- Jameson, A., Schmidt, W. and Turkel, E. (1981) "Numerical solution of the Euler equations by finite volume methods using Runge-Kutta time stepping schemes". AIAA Technical Report, 81-1259.
- Koren, B. (1993) "A robust upwind discretisation method for advection, diffusion and source terms", In: Vreugdenhil, C. and Koren, B., eds, Numerical Methods for Advection-Diffusion Problems (Vieweg, Braunschweig), pp 117-137.
- Roe. P. (1981) "Approximate Riemann solvers, parameters vectors, and difference schemes", Journal of Computational Physics 43, 357-372.
- Roe, P.L. (1985) "Some contributions to the modelling of discontinuous flows", Lectures in Applied Mathematics 22, 163-193.
- Roe, P.L. and Baines, M.J. (1982) Algorithms for advection and shock problems, 4th GAMM Conference on Numerical Methods in Fluid Mechanics (Braunschweig, Vieweg).
- Smolarkiewicz, P. (1982) "The multi-dimensional crowley advection scheme", Monthly Weather Review 110, 1968-1983.
- Staniforth, A., Cote, J. and Pudykiewicz, J. (1987) "Comments on Smolarkiewicz's Deformational Flow", Monthly Weather Review 115, 894-900.
- Tamamidis, P. (1995) "A new upwind scheme on triangular meshes using the finite volume method". Computational Methods in Applied Mechanics and Engineering 124, 15-31.van Leer, B. (1973) "Towards the ultimate conservative difference
- van Leer, B. (1973) "Towards the ultimate conservative difference scheme I. The Quest of Monotonicity", Lecture Notes in Physics 18, 163-168.
- van Leer, B. (1974) "Towards the ultimate conservative difference scheme II. Monotonicity and conservation combined in a second-order scheme", *Journal of Computational Physics* 14, 361-370.
- van Leer, B. (1979) "Towards the ultimate conservative difference scheme V. A second-order sequel to Godunov' method", *Journal of Computational Physics* 32, 101-136.